3D CFD-DEM-IBM SIMULATIONS OF SAND PRODUCTION IN OIL WELLS

Aigerim Rakhimzhanova

A thesis submitted in partial fulfillment of the requirement of Nazarbayev University for the degree of Doctor of Philosophy in Science, Engineering and Technology

Supervisory committee:
Prof. Michael Yong Zhao, Nazarbayev University
Prof. Sergey Spotar, Nazarbayev University
Dr Colin Thornton, University of Birmingham

April 2021

Declaration

I declare that the research contained in this thesis, unless otherwise formally indicated within the text, is the original work of the author. The thesis has not been previously submitted to this or any other university for a degree, and does not incorporate any material already submitted for a degree.

Aigerim Rakhimzhanova
March 9, 2021

Abstract

Sand production is particularily prominent in sandstone reservoirs, which are common to observe in the majority of oil and gas fields. When sand particles start to erode from weak sandstone formations for different reasons, their impact could lead to the decline of the production flow rate and equipment degradation, which will results in a huge economical loss. In some cases, it results in the end of production life of a well and reservoir. The key to overcome this problem and achieve accurate prediction of sand production may lie in the understanding of the cause of sanding mechanism.

The current numerical approaches to predict the sanding mechanism are based on continuum and non-continuum models. The majority of developed models are based on the continuum approach, while a few discontinuum-based (DEM – Discrete Element Method) have been developed in the last two decades. Sand production is a dynamic and continuous process, which starts from microscopic scales where the rock is discontinuous in nature. It is impossible to capture local discontinuous phenomena using continuum-based models. The DEM models can capture the interaction and motion of each sand grain, the failure micro mechanism in a dynamic process at micro and macro scales, which makes it possible to simulate the sanding phenomena.

In this research the DEM is firstly used for the rock characterization, where a simple 3D bond contact model for cemented sandstone material is developed by modifying the previous existing JKR (Johnson-Kendall-Roberts) model for auto-adhesive silt size sand particles, and the model parameter is the bond strength in terms of the interface energy. The material properties of the synthetic sandstone specimens equivalent to the Ustyurt-Buzachi Sedimentary Basin core samples were reproduced for the numerical specimens and the triaxial compression test results show that the numerically simulated macroscopic response is in good agreement with the experimental results of the cemented sandstone.

The main aim of this research is to develop the sample preparation procedure/method with physical perforation penetration and sand production modelling in a periodic cell and by developing and using the combined 3D CFD-DEM-IBM modelling techniques (CFD – Computational Fluid Dynamics; IBM – Immersed Boundary Method). The application of the IBM is proposed to simulate the complex interaction between the geometry of the cased horizontal well completion opening and the weakly cemented sandstone under the

overburden pressure and drawdown. The capability of developed methods to capture sand arching, damage zone (due to the perforation penetration) and sanding mechanism (erosion near the perforation hole) due to the pressure drawdown are presented. This study shows the mechanism of sand production in a bottom-up approach in the first 0.1 sec of sanding initiation immediately after the perforation penetration in oil wells, which will help engineers to better understand the sanding mechanism at the micro levels and how the problem of sanding can eventually be overcome though better insight into the phenomenon.

Acknowledgements

This thesis is dedicated to my late grandfather, Nazhmedin Temirovich Kabiyev.

Foremost, I thank the Almighty for giving me the strength and patience to work through all these years.

My greatest appreciations go to my external supervisor – Dr Colin Thornton, who introduced me into the research in particle technology. I would like to thank him for the continuous support of my Ph.D. study, for his patience, immense knowledge that he shared with me and his encouragement. He taught me how to carry out the research in granular media using 3D DEM modelling from scratch. I could not have imagined having a better supervisor for my Ph.D. studies, it was a great honor and privilege to study and work under his supervision.

I want to express my deepest gratitude to my lead supervisor – Professor Michael Yong Zhao. I am thankful for his encouragements, invaluable support and professional recommendations he has provided during my Ph.D. research. My special thanks for his prompt responses to my queries and questions. My sincere gratitude also goes to my co-supervisor – Professor Sergey Spotar, for his time and valuable comments towards improving my research. I feel extremely lucky to have them as my supervisors and it was a great honour and pleasure for me to conduct research under their supervision.

I gratefully acknowledge Professor Stefano Utili for giving me an opportunity to visit and carry out my research at the University of Warwick and Newcastle University, where I spent significant period of my Ph.D. research. I also thank Dr Helen Cheng for her advices, suggestions and help during my research visit to University College London.

My heartfelt thanks go to Director of Ph.D. Studies and Associate Professor - Luis R. Rojas-Solórzano, for his kind support and brilliant work with all Ph.D. students at School of Engineering and Digital Science, Nazarbayev University.

I am enormously thankful to my grandmother, parents and sister for their love, supporting me during the Ph.D. studies and during my entire life. I am extremely grateful to my friend for financial support during the last 2 years of my Ph.D. studies. Last but not the

least, I would like to thank all my Ph.D. colleagues for the spent wonderful years, and I also appreciate all my friends for their invaluable support.

Financial support from the HERCULES “towards geoHazards rEsilient infRastruCtUre under changing cLimatES” (H2020-MSCA-RISE-2017 Grant No 778360); the EU Project GEO-RAMP (H2020- MSCA-RISE-2014 Grant No 645665); the Ministry of Education and Science of the Republic of Kazakhstan (Grant No AP08052762) and the SOE 2015004 grant are gratefully acknowledged.

Contents

List of Figures

List of Tables

List of Abbreviations

CFD	Computational Fluid Dynamics
CPT	Cone Penetration Test
CSL	Critical State Line
DEM	Discrete Element Method
IBM	Immersed Boundary Method
LSO	Large Solid Object
FDM	Finite Difference Method
JKR	Johnson-Kendall-Roberts model
FEM	Finite Element Method
PISO	Pressure-Implicit with Splitting of Operators
PSD	Particle Size Distribution
SBT	Soil Behaviour Type
SEM	Scanning Electron Microscope
SIMPLE	Semi-Implicit Method for Pressure Linked Equations
USGS	Unified Soil Classification System
TWC	Thick Wall Cylinder
XRD	X-Ray Diffraction

Chapter 1 – Introduction

1.1 Research background

Sand production is one of the major problems in the petroleum industry. This is specifically conspicuous in sandstone and terrigenous reservoirs where most gas and oil reservoir fields are often observed. The sandstone reservoir comprises the following typical substances: mica, quartz and rock fragments as well as various kinds of mineral grains with clay, cements or silica (Bjorlykke, 2010). Furthermore, these reservoirs have a high permeability (from 25 to 100 Darcies) as well as a high porosity of about 15%. For various reasons, when sand particles begin to erode from weak sandstone formations, deterioration of the production flow rate and degradation of the equipment could follow. The flow can be choked when the well is filled with sand, thereby causing the casing to collapse, and production costs can increase when the surface is damaged by plugging or erosion. Moreover, the produced sand management is essential to avoid an adverse effect on the environment (Carlson et al., 1992).

Several oilfields in Kazakhstan located in the Ustyurt-Buzachi Sedimentary Basin are faced with this costly problem. In 2025 horizon R&D roadmap of the oil and gas industries in Kazakhstan, the sand control and optimizing recovery are listed as the 1st and the 11th major technical challenges and the resolution of this problem is critical. Nowadays, Zhalgiztobe, North Buzachi, Kenkiyak and Karazhanbas oil fields are all faced with the sand production problem and its management issues. Operators control the sand production simply by dumping the unwanted sand materials in special disposal sites. Reduction of sand production and its disposal are both equally important. Successful overcome of these challenges will contribute to the flow assurance technologies and the development of well completion that can lead to the optimization of oil production. The financial reward of overcoming this challenge is estimated to be in the region of US$ 3.5 billion (Collective industry effort, 2013).

The key to overcome the issue in the accurate prediction of sand production may lie in the understanding of the sanding mechanism. Currently, there are several methods to

predict this sanding phenomenon: analytical, theoretical, experimental, empirical and numerical methods (Rahmati et al., 2013). Over the past several decades, many researchers carried out comprehensive research on the sand production problem using the aforementioned methods and made their invaluable contributions to the common treasury of science.

The aim of this research is dedicated to numerically study the behavior of sandstone materials and their sanding mechanism using a coupled modelling technique of CFD-DEM-IBM.

1.2 Scope and objectives

The research scope is to build geometry and develop procedures for perforation penetration and sand production simulations and generate numerical samples which are maximally similar to the synthetic sandstone specimens equivalent to the Ustyurt-Buzachi Sedimentary Basin core samples.

The first step is to develop a 3D bond contact model for cemented sandstone materials utilising the DEM method. This model will be further utilised to examine the mechanical behavior of cemented reservoir sandstone. Evaluation of the model will be conducted by comparing its predictions with findings from triaxial compression tests with different values of cement bond strength, confining pressure and friction coefficient. The goal is to replicate the Particle Size Distribution (PSD) and material properties of the synthetic sandstone specimens equivalent to the Ustyurt-Buzachi Sedimentary Basin core samples with the numerical model. A mathematical model based on the Mohr-Coulomb theory, which describes the relationship of the tangential stresses of the material with the applied normal stresses, will be constructed. This will help to obtain the Mohr-Coulomb strength criterion parameters c’ (the inherent shear strength) and φ’ (the friction angle) for the numerical model and establish correlations between the shear strength parameters and the bond strength. The correlations can then be utilised to find the bond strength value to be used for comparing with the findings of experimental triaxial tests.

The work will be followed by the development of a new numerical model for the physical and realistic simulation of the perforation penetration. The material properties including the cement bond strength determined in the triaxial compression test will be used to simulate and study the damaged zone due to the perforation penetration.

The final stage of the work is to investigate the 3D CFD-DEM-IBM model and use it to simulate the sand production problem using the previously perforated numerical samples and complex boundaries, where the IBM technique will be optimized in order to simulate the complicated interaction of the geometry associated with the well completion opening and the weakly cemented sandstone under the overburden pressure and drawdown. Oil with low viscosity and density will be used as an injection fluid (reservoir fluid). The erosion of weakly cemented sandstone materials near the perforation tunnel due to the pressure drawdown will be examined under different bond strength values and relative gravity directions (to imitate vertically upward and downward perforation cavities). Hence, the sanding mass and the associated production mechanism could be determined and investigated in a multi-scale/multi-physics bottom-up framework.

The objectives of this research are follows:

1. To develop a 3D bond contact model for reservoir cemented sandstone suitable for performing triaxial compression tests, cone penetration tests and sand production simulations.
2. To perform 3D DEM simulations of triaxial compression tests of sand and cemented sandstone.
3. To develop a 3D DEM model and procedure for realistic/physical perforation penetration simulations.
4. To develop a 3D CFD-DEM-IBM model for sand production simulation.
5. To examine the mechanism of sand production.

The originality of this research includes the followings:

- Development of a new 3D bond contact model for cemented reservoir sandstone by modifying the previous existing JKR theory for auto-adhesive silt size sand particles;
- Identification of the bond strength value defined in term of interface energy for experimental cemented sandstone;

- Development of a new realistic model/procedure of perforation penetration with the damaged zone. Analysis of the 3D DEM Cone Penetration Test (CPT) in cemented sandstone results within the Soil Behaviour Type (SBT) framework;
- Development of a new complex sand production simulation geometry and procedures with a realistic/physical perforation penetration and immersed complex boundaries;
- Capturing of a sand arch around the perforation cavity; and
- Elucidation of sand production mechanism at micro and macro scales.

1.3 Assumptions and limitations

In this study, numerical simulations of sand production in a sandstone formation were performed at 1 MPa of overburden pressure equals to a well depth of 39.1 m. The verification is based on the experimental triaxial data conducted on shallow depth conditions. The main limitation of current triaxial simulation works were the low confining stress levels. The numerical confining stress levels 100-1000 kPa were selected because of the availability of experimental data and results for comparison and validation. In the experimental study, the maximum limit of allowable confining stress level in a triaxial apparatus was 700 kPa. Therefore, Shabdirova et al. (2016) conducted the triaxial test at 300 kPa, 500 kPa and 700 kPa and the authors didn't consider a real oilfield reservoir depth of 200-500m located in Ustyurt-Buzachi Sedimentary Basin. This work does not support that the obtained results are applicable too high depth and high confining stress faced in actual conditions. The assumption was made that the developed contact bond model for cemented sandstone needs to be carefully examined and validated by experimental data before performing the simulations of triaxial compression test, perforation penetration and sand production with large confining stress levels and overburden pressures.

Fully 3D simulations of cone penetration and sand production tests in cemented sandstone with real-world PSD are excessively time consuming. Therefore, due to time constraints, plane strain and quasi-3D simulations of cone penetration and sand production were performed which defines as another limitation of the current study.

Numerical simulations of perforation penetration tests (cone penetration) do not consider damage criterion and model. In this study, perforation damage is a zone of increased porosity, broken contacts and bonds created around perforation tunnels by physical cone penetration.

1.4 Publications

1. Rakhimzhanova, A. K., Khamitov, F. A., Minh, N. H., & Thornton, C. (2018). 3D DEM simulations of triaxial compression tests of cemented sandstone. In Proceedings of IS Atlanta 2018 symposium on geomechanics from micro to macro in research and practice, Atlanta, USA.
2. Rakhimzhanova, A. K., Thornton, C., Minh, N. H., Fok, S. C., & Zhao, Y. (2019). Numerical simulations of triaxial compression tests of cemented sandstone. Computers and Geotechnics, 113, 103068. https://doi.org/10.1016/j.compgeo.2019.04.013
3. Rakhimzhanova, A., Thornton, C., Amanbek, Y., & Zhao, Y. (2021). Numerical simulations of cone penetration tests in cemented sandstone. In EPJ Web of Conferences, 249, 14010. EDP Sciences. https://doi.org/10.1051/epjconf/202124914010
4. Rakhimzhanova A, Thornton C, Amanbek Y, Zhao Y. Numerical simulations of sand production in oil wells using the CFD-DEM-IBM approach. Journal of Petroleum Science and Engineering. [Accepted]

Peer-reviewed research proposal:

1. Effect of Flow through Porous Media on Sanding Phenomena in Poorly Consolidated Reservoirs – Research Assistant and co-author. Funding Agency: Ministry of Education and Science of the Republic of Kazakhstan. Grant No AP08052762, 2019. PI – Dr. Yerlan Amanbek.

1.5 Thesis layout

This thesis contains 7 chapters.

The current Chapter 1 presents the research background and its aims and objectives.

Chapter 2 widely defines the sand production problem in terms of definition, perils, factors, mechanism, management, control and prediction (Section 2.1); presents basic principles of Petroleum Engineering related to sand production problem (Section 2.2).

Chapter 3 provides a numerical methodology that will be used during the modelling of sand production problem. Section 3.1 introduces the main numerical methods and tool used in this study. The DEM and its governing equations, the theoretical background of granular dynamics are described in Section 3.2. The developed 3D contact bond model is provided in Section 3.3. Section 3.4 presents a coupled modelling technique of CFD-DEM-IBM in terms of interaction forces between fluid-particle, particle-fluid and particle-fluid with the complex geometries (boundaries); numerical algorithm and pressure-correction equations. Section 3.5 describes numerical solutions of DEM and hydrodynamics models and Section 3.6 provides information on boundary conditions for DEM, CFD and IBM models.

Triaxial compressions test simulations and validation are presented in Chapter 4. The data of the Ustyurt-Buzachi Sedimentary Basin reservoir analogue synthetic samples are written in Section 4.2. Section 4.3 presents the numerical simulation stages and procedure; and Section 4.4 reports the results obtained from the triaxial compression tests simulations on medium dense, medium loose and loose cemented sandstone samples using 3D DEM approach and provides the comparison with experimental data.

In Chapter 5, the numerical simulations of physical perforation penetration (cone penetration test) are presented. Section 5.2 describes the numerical simulation stages, procedure and sample geometry and Section 5.3 reports the obtained results from 3D DEM simulations of CPT tests.

Chapter 6 presents sand production simulations in oil wells. Section 6.2 provides the sand production simulation details with model setup. The results and discussion of sand production simulations are reported in Section 6.3.

Chapter 7 concludes the main findings and outcomes of the numerical simulations of triaxial compression, cone penetration and sand production tests and provides recommendations for future works.

Chapter 2 – Literature review of the sand production problem

2.1 Introduction to the sand production problem

Sand production is a global problem. This always has serious consequences in the development of oil and gas fields. When sand particles start to erode from weak sandstone formations for different reasons, the impact could lead to degradation of the equipment and deterioration of the production flow rate. The filling of the well with sand can cease the flow and result in collapse of the casing. The damage to the surface equipment by erosion or plugging can increase the cost of production. Each year the petroleum industry is losing millions of dollars for the cleaning of sand. In the worst-case scenario, the production life of the reservoir and well may catastrophically end. In addition, the management of the eroded sand is vital to prevent a negative impact to the environment (Carlson et al., 1992). Besides the main actions (sand management and control) to be taken in the oil and gas fields, the key to overcome the issue in the accurate prediction of sand production may lie in the understanding of the cause of the sanding mechanism.

Predicting sand production involves numerous multidisciplinary areas, which include: drilling; fluid mechanics; geology; geomechanics; geophysics; petroleum, reservoir and production engineering. Furthermore, a hydrocarbon's field life with its three stages (exploration, development and production) needs to be considered and comprehensively studied. Each stage has particular targets and involves the collection of massive amounts of data for sand production issues. Consequently, it is a difficult and complicated task.

2.1.1 Factors and types of sand production

Sand production in oil fields is a complex and wide-ranging phenomenon, which depends on various factors. Veeken et al. (1991) classified parameters influencing sanding process into the 3 categories: formation, completion and production (Table 2.1). Based on these parameters, the types of sand production and sanding mechanisms (shear and tensile failures, erosion and transportation of fine particles) will differ.

Table 2. 1. Parameters affecting sanding problem (Veeken et al, 1991)

Categories	Parameters
Formation	Rock
	- Strength
	- Vertical and horizontal in-situ stresses (change during depletion)
	- Depth (influences strength, stresses and pressures)
	Reservoir
	- Far field pore pressure (changes during depletion)
	- Permeability
	- Fluid composition (gas, oil, water influenced by completion and production philosophy)
	- Drainage radius
	- Reservoir thickness
	- Heterogeneity
Completion	- Wellbore orientation, wellbore diameter
	- Completion type (open hole/perforated)
	- Perforation policy (height, size, density, phasing, under/overbalance)
	- Sand control (screen, gravel pack, chemical consolidation)
	- Completion fluids, simulation (acids volume, acid type)
	- Size of tubulars
Production	- Flow rate
	- Drawdown pressure
	- Flow velocity
	- Damage (skin)
	- Bean-up/shut-in policy
	- Artificial lift technique
	- Depletion
	- Water/gas coning
	- Cumulative sand control

Sand production was categorised by Veeken et al. (1991) into the following three types: transient, continuous and catastrophic.

Transient sand production: Following an initial burst, a continuous sand production occurs whose rate declines under constant conditions. It often becomes apparent immediately subsequent to a perforation penetration work, water breakthrough, changes in production conditions (generally a well-pressure reduction).

***Continuous sand production*:** This is where sand is produced continuously, and at a comparative constant rate. Following many years of production, it is possible for this type of sand production to add up to hundreds of kilos per metre of the well, even for just a few

grams per cubic metre. It is clear that removing such a vast volume of sand changes both the shape and size of the producing cavities. For example, when perforations are effectively formed separately, the eventual result could be that they form larger cavities behind the casing.

***Catastrophic sand production*:** In this type the well becomes choked because of the high rate of sand production, which occasionally results in well conservation.

2.1.2 Mechanisms

Two stages are involved in the sanding mechanism in the petroleum industry. This commences when the stress on the formation becomes greater than its strength, thereby causing rock failure. In such conditions, stresses in the vicinity of wellbore and/or perforations become more concentrated, and weak rocks are liable to deformation. Furthermore, the following factors can be cause of damage to the adjacent wellbore area of the formation: overburdened pressure, tectonic activity, reservoir depletion, pore pressure, drilling and perforating. Moreover, the reservoir fluid flow and its corresponding viscous stress gradients, pressure gradient, and drag force applied to the weakened formation cause erosion at the sandface, whereby sand grains are conveyed up the wellbore.

Over the years, different sand production prediction approaches have been used to understand the origin of sanding mechanisms: experimental, empirical, analytical and numerical (Section 2.1.5) and various failure criteria have been developed to describe the strength of rock under different stress conditions: the Hoek–Brown, Mohr–Coulomb, Mogi, modified Wiebols–Cook, modified Lade, Drucker–Prager, von Mises, Griffith and etc. Additionally, several types of rock mechanics tests (Figure 2.1) have been developed to determine the approximate strain around the axial hole at which failure occurs: hydrostatic compression tests, uniaxial compressive tests, uniaxial tension tests, triaxial compression tests, triaxial extension tests, and polyaxial tests (or true triaxial). Following Zoback (2017), two important facts should be always noted: the stresses acting in the earth at depth are strongly concentrated around wellbores; and core samples of overburden formations are never available for laboratory testing. However, in actual field case studies it is better to use the rock strength data obtained from experimental works.

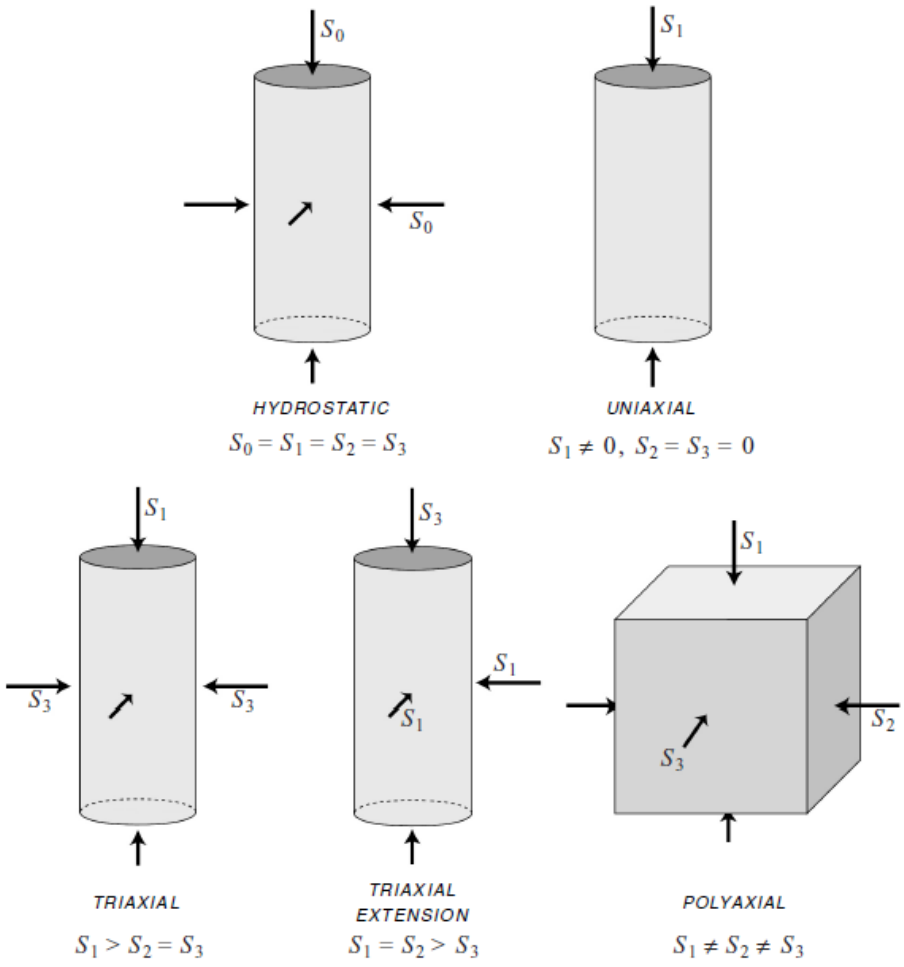

Figure 2. 1. Rock mechanics tests (adopted from Zoback, 2017)

Lastly, in the region adjacent to the cavity wall and borehole, 3 kinds of rock failure are evident, such as tensile failure, compressive (or shear) failure and erosion (Veeken et al., 1991).

Compressive (or shear) failure of rock happens when the stresses acting on a rock mass are greater than its compressive strength. This occurs with every stress that acts on the rock (including the pore pressure), and it can be instigated by pressure drawdown and reservoir depletion. Another type of compressional rock failure occurs in porous rocks (uncemented sands, sandstones), known as end-cap failure or shear-enhanced compaction. This leads to losses of permeability and porosity as a result of pore collapse and greater shear stress and/or confining pressure that exceeds a limiting value that causes reservoir depletion.

Tensile failure, which is usually caused by high pressure drawdown, is an uncommon occurrence in oil fields. Overburdened stress at depth is never tensile; therefore, in all rocks, the tensile strength is considerably less in that it is assumed to be close to zero where there are pre-existing cracks in rock. Consequently, it should be borne in mind that the tensile strength of rock in the earth's crust is relatively unimportant compared with compressional strength. Tensile failures can occur near wellbores in some stress states (when tensile radial stress exceed the tensile failure envelope) since the stresses acting in the earth at depth are strongly concentrated around wellbores. Furthermore, although the near wellbore tensile failure produces lower amounts of sand, it stabilises after a period of time. One of the type of tensile failure – hydraulic fracturing, happens when fluid pressure becomes greater than the local least principal stress.

Erosion happens when the resultant force from fluid drag, pressure gradient and shear stress gradients acting on a particle at the sandface become greater than its apparent cohesion, which according to Vekeen (1991), is a specific type of tensile failure.

2.1.3 Sand management

The aim of sand management is to guarantee that hydrocarbon production is maintained when particulate solids exist in well fluids, simultaneously minimising the effect of the produced solids on surface equipment. A control technique is needed when the particle size or solids rate cause lost production in order to recover the hydrocarbon flow to its economically sustainable level. It is essential to know txhe chemical and physical attributes of the produced solids in order to compare the inclusionary and exclusionary methods. The physical attributes of each kind of solid, which may be exploited for separation or completion, are of principal concern. Such attributes include concentration, density, particle size dissemination and shape. Inorganic particulates produced at an adequate concentration and size that need separation or exclusion treatment are usually referred to as produced solids. Such material may be generally divided into two classifications, namely natural (indigenous) and artificial (foreign). Natural solids emerge from formation minerals which are generally silt and sand, being a terminology according to size rather than chemical nature. Foreign

materials produced by external intervention are artificial solids; for example: cement fines, gravel pack material, corrosion products, drill mud, injection fines, fracture sand or proppant.

Sand control equipment conventionally concentrates on particulate matter from entering the well in one of two ways: completion design or production limits, also known as exclusionary techniques, which include the followings: chemical consolidation, mechanical retention (slotted liner or screen), gravel packs, or a combination of any of these methods (Penberthy, 1992). The optimal technique is chosen according to production life, intervention costs, well and reservoir conditions, and whatever treatment that gives maximum sustained productivity.

Another method of sand management is the production of solids from well fluids, subsequently separating them at the surface facility. Since the solids flow freely with the gas and oil at the production facilities or the choke, this method is known as inclusionary technique. The solids and the well fluids are separated prior to the separator vessels or at the choke by a multiphase desander.

The separated solids could need the following steps: central collection, cleaning, measurement, storage, transportation to a landfill site, injection disposal or overboard discharge (Rawlins et al., 2000; Rawlins, 2013). The separated sands are managed by worldwide oilfield operators, basically by dumping in special disposal sites (Figure 2.3), thereby having an adverse effect on the environment. Sand production reduction and its application both present major problems.

Sustainable oil and gas production is the main goal for choosing an inclusion or exclusion method. The application of sand management technology oil and gas fields with sand production problems has resulted in well life extension on marginal fields, increase in oil and gas production from sand producing wells, and shut-in wells restart in specific oil and gas fields around the world.

Figure 2. 2. Oilfield waste landfill (adopted from Druzin, 2018)

2.1.4 Sand control

Available tools for the control of produced solids include: downhole completions in order to avoid sand ingress from the reservoir face; production limits in order to sustain sand inflow below the damaging threshold; traditional facilities for processing sand which comes to the surface with particular devices of separation whose function is to enhance the strength of facilities' operations.

Production Limits: The most basic solids' control technique is the adoption of a method of *zero sand production* (Palmer et al., 2003; Selfridge et al., 2003; Tiffin et al., 2003; Wong et al., 2003). This technique seeks to establish a maximum sand-free production rate according to drawdown criteria. Well tests enable a map of drawdown to establish sand-free production areas. Although this method needs minimal capital expenditure, it reduces hydrocarbon production and inflow. Furthermore, since the well flow profile is in a constant state of change, the sand-production map is a moving target. Changes in sand production can be detected by sand monitoring instruments which are used to optimise drawdown (Balgobin et al., 2005; Musa et al., 2005; Stein et al., 2005; Vaziri et al., 2006).

Figure 2.4 depicts a window of safe drawdown indicating the predicted safe drawdown for specific combinations of stress conditions, completion, initial reservoir

pressure and rock strength. The plot of reservoir pressure versus bottom hole flowing pressure comprises three zones: 1) no production zone locates above the diagonal line where the bottom hole flowing pressure exceeds the reservoir pressure; 2) well production zone, where the bottom hole flowing pressure is less that the reservoir pressure. The well production zone is divided by the predicted safe drawdown line into the sand-free production zone (green) and sand production (and reservoir fluid) zone (red).

As depletion increases, there is a change in the amount of drawdown that can be applied to the completion without failing the rock. Furthermore, prediction of the line of safe drawdown in the safe window is a principle objective of sand production problem.

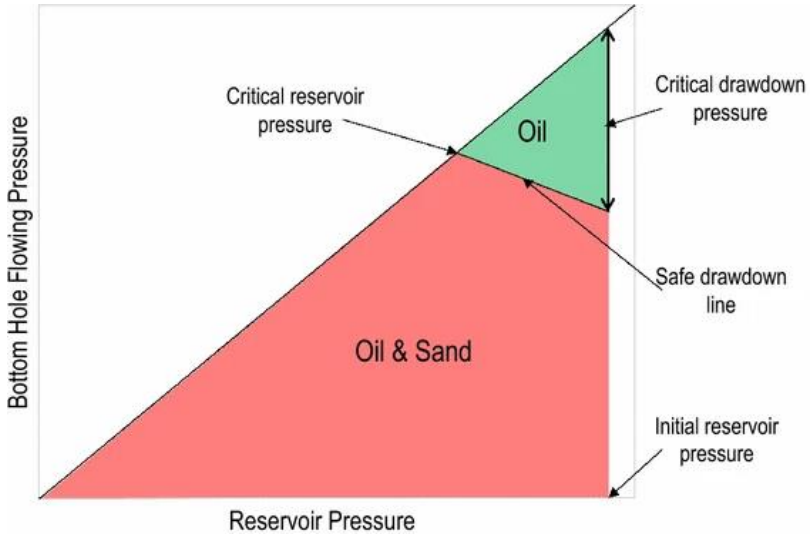

Figure 2. 3. Safe window for sand production (adopted from Mohamad-Hussein and Ni, 2018)

Completions: The most frequently applied sand control technique is the exclusion of sand from the wellbore by utilising open and cased-hole gravel packs, wire-wrapped screens, expandable screens, frack packs, selected and oriented perforation and others (Figure 2.5). Most sand is prevented from entering the flow path together with well fluids by mechanical retention that uses slotted liners or screens. The design is planned so that spherical particles will not flow continuously through rectangular slots that are double the width of the particle. This is provided that they flow in adequate concentration and bridge over the opening, due to grain-to-grain contact (Penberthy, 1992). Gravel packs are used in combination with screens, and accurately sized and clean gravel is placed around the periphery, thereby enabling a greater screening area. Furthermore, the gravel has greater resistance to erosion

than does the screen material. Gravel pack methods, which are the preferred option for sand control, are comprehensively studied (Price-Smith et al., 2003; King et al., 2003; Williams et al., 2006).

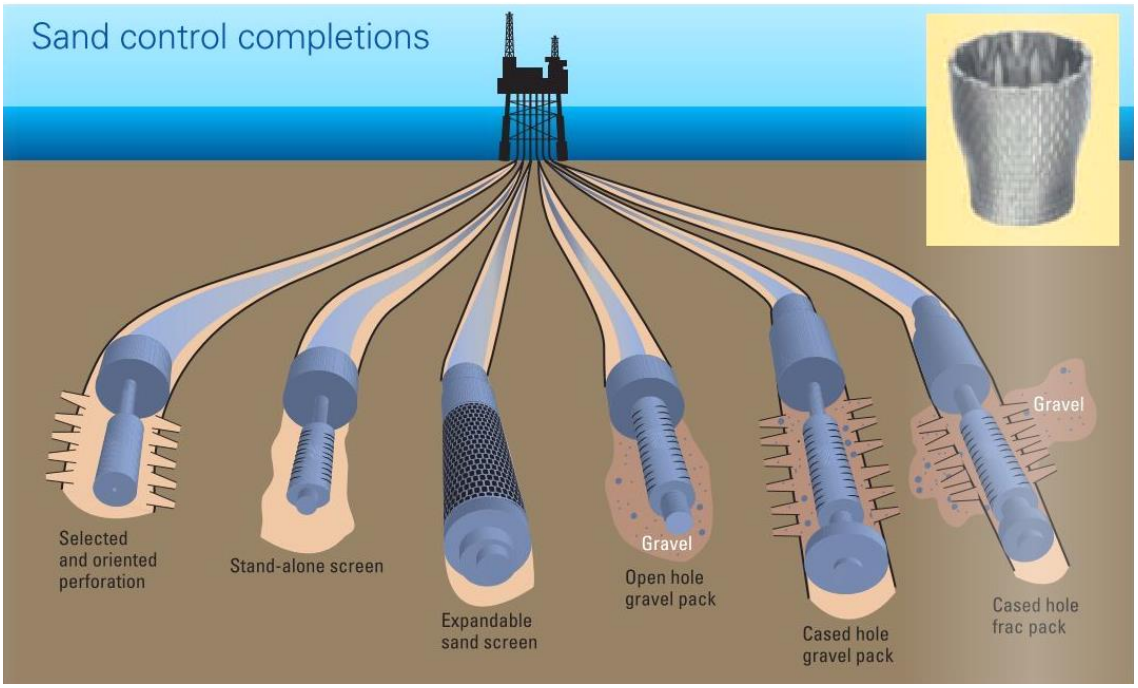

Figure 2. 4. Sand control completions (adopted from Morgan, 2006)

Chemical sand control methods can bind the formation sand particles for a radius that is many centimetres from the wellbore. Penberthy (1992) reported that plastic consolidation creates a bond between the existing formation sand grains, thereby building a filter barrier to flowing sand. In this technique, multiple stages are needed for installation; for example, pre-flush, injection of the catalyst and resin, and acid clean.

Several combinations of the aforementioned methods may be applied for efficient sand control. Moreover, in comparison with traditional screen liners, multipath and expandable screen present greater throughput and flexibility (Williams, 2006; Iversen, 2006). In order to verify good placement of the consolidating resin, precoated gravel may be injected. Frac pack combines the advantages of gravel packing with the simulations of hydraulic fracture. Since they attempt to prevent the reservoir material from entering the wellbore, all of these methods are exclusion techniques.

Surface Facilities: These are traditional facilities for extracting sand particles which lift to the downstream, which requires particular separation equipment in order to enhance the strength of the topside operation.

2.1.5 Prediction

Empirical, experimental, analytical and numerical methods have been applied to forecast the difficulty of sand production and to gain an improved understanding of the onset and sanding mechanisms. Combined techniques are useful for thorough sand management and control.

2.1.5.1 Empirical methods

Field observation or empirical techniques utilise many field parameters and data to forecast the onset of sand production, as shown in Table 2.1. (Veeken et al., 1991). Such parameters are dependent on production and recovery mechanisms, completion type and reservoir attributes. Furthermore, the empirical corelations of parameters will vary according to each field and well. The fact that few parameters can be utilised is a major drawback of this technique, which is because of the problems regarding monitoring and recording data in every well in a field (Veeken et al., 1991).

Numerous empirical corelation techniques are based on the following parameters: porosity, pressure drawdown, and critical depth. Furthermore, in order to assess the formation hardness and porosity, density, neutron and sonic logs are extensively utilised in gas and oil fields in which the sonic log evaluates the time taken to transmit sound waves through the formation. If the time transmits less than 50 μm seconds, then the sandstone formation is hard and has high density and low porosity. However, if the time transmits over 95 μm seconds, the formation sandstone may be considered to be soft and to have a low density and high porosity. Consequently, if the formation porosity is over 30 per cent (weakly consolidated), the sand control method is required.

The next correlation technique is establishing a critical depth, which is based on the assumption that rock strength usually increases with depth. Veeken et al., 1991 reported that a critical depth criterion for the installation of sand control measures is used in several deltaic environments and a sand control technique is not required below the critical depth. The critical depth is established from field experience and it is regionally dependent. Tixier at al. (1975) and Lantz and Ali (1991) mentioned that the critical depth is ~3600 m and ~2100 m, respectively.

Another correlation technique applies the critical pressure drawdown, being a maximum drawdown value for which no sand is triggered (Subsection 2.1.4). No sand control method is needed below the critical drawdown.

It is impossible for the empirical techniques to forecast the amount of sand production, which it occasionally overestimates. Consequently, this could lead to an incorrect decision regarding sand control, thereby resulting in greatly increased economic expenditure.

2.1.5.2 Experimental methods

Over several decades, experiments were performed in a laboratory to examine controlling parameters regarding solid stress, material attributes, fluid flow rate and pressure drawdown for the purpose of gaining an understanding of the sand production pattern in various conditions. The first scientific experiments associated with sanding problem was conducted by Terzaghi in 1936, and the author was the first who observed a sand arch near a bottom hatch in a box filled with sand. Hall and Harrisberger (1970) improved Terzaghi's experiment and found a link between the introduced fluid flow and the formation of sand arches. Experiments were investigated later using various hydrocarbon production parameters in which it became apparent that sand production depends on stress anisotropy, stress level, saturation and injection fluid and formation rock material (Tronvoll et al., 1993, 1997; Papamichos et al., 2000; Nicholson et al., 1998; Wu et al., 2016; Fattahpour et al., 2012). Many researchers have utilised various kinds of fluid; for instance, water (Wang and Wu, 2001; Wu et al., 2016); diesel fluid (Fattahpour et al., 2012); kerosene (Nicholson et al.,

1998); brine (Al-Awad, 2001; Van Den Hoek et al., 2000; Zivar et al., 2019) and paraffin oil (Papamichos et al., 2000).

Several researchers have conducted experimental studies with modified thick wall cylinder (TWC) tests in order to study the stress behaviour adjacent to the borehole which has an impact on the sand production process (Veeken et al., 1991; Wu and Tan, 2002; Papamichos et al., 2001, 2010; Nouri et al., 2004, 2006; Papamichos and Vardoulakis, 2005; Papamichos, 2006; Ispas et al., 2006; Dresen et al., 2010; Fattahpour et al., 2012). This testing method provides awareness of sand production mechanisms, and also of the effect of different operational and field parameters on sand production. Nevertheless, since it is easier to sample stronger rock rather than uncemented and weak rock, these tests are, to a certain extent, limited.

The experimental technique's principal drawback is that all of the cemented analogue samples that have been studied experimentally are not core samples of overburdened formations, such samples being rarely available for comprehensive testing in the laboratory (Zoback, 2017). However, tests of sand production were normally investigated on artificial samples because of the problems with retrieving rock cores. Holt et al. (2000) and Alvarado (2007) stated that, in the course of sampling, core samples from deep wells experience stress release. This results in the laboratory results collected by examining such samples to be an inappropriate representation of the materials' in-situ behaviour, which could also give an incorrect representation of the possibility of sanding problem. Furthermore, experimental works are costly, and occupy a considerable amount of time; moreover, small sizes of the laboratory setup normally lead to boundary effects on the results.

Additionally, experimental samples ought to be used to replicate (or at least mimic) the real field conditions. In this case, the deposition, cementation, compaction, lithification, drilling and completion with casing and cementation (if necessary), perforation of sandstone and sand production ought to be applied to the sandstone sample. This is in order to represent the in-situ behaviour of the material from deep penetration holes of oil wells. The standard of the experimental work depends, in a controlled way, on the real conditions. Nevertheless, it is usual for several previous experimental sand production designs to separate the principal steps of preparation of sample, perforation, sand production, thereby causing the sandstone sample to crack (Alvarado et al., 2012; Holt and Kenter, 1992).

The fact that the in-situ perforation was not normally considered was a further limitation of past experiments. A prepared hollow cylinder specimen was generally utilised to conduct the production experiments. Moreover, in order to create this core, a metal rod was placed at the centre of the cast moulds, and subsequently to the completion of the procedure, was removed (Nouri et al., 2006). Baxter et al. (2009) reported that this specimen preparation technique restricts the perforation damaged zone, thereby making a notable contribution to the seriousness of sand production.

2.1.5.3 Analytical methods

Although analytical or theoretical techniques are rapid and user-friendly, they are appropriate only to forecast the commencement of sand production. Rahmati et al., (2013) reported that the majority of analytical techniques are valid only for capturing one sanding mechanism under simplified boundary and geometrical conditions, but not normally in complex field-scale problems.

Much research has been conducted on the prediction of the commencement of sanding according to the conditions of stress and fluid flow where rock failures and erosion happen respectively (each of these mechanisms is described in Subsection 2.1.2). In order to study the sanding onset Bratli and Risnes, 1981; Risnes et al., 1982; Bradford and Cook, 1994; Yi et al., 2005; Nouri et al., 2006; Jin et al., 2011; Al-Shaaibi et al., 2013; Papamichos and Furui, 2013; Hayavi and Abdideh, 2017 used the Mohr-Coulomb, Drucker-Prager, Mogi-Coulomb, Hoek-Brown and modified Lade failure criteria as the failure models.

In order to forecast the critical condition for sand arch stability, Bratli and Risnes (1981) offered an elastoplastic paradigm. The steady-state fluid flow was applied in this model, and in order to examine sand initiation, the effective radial stress in the plastic area of a sand arch was used. The sand arch would be considered to have failed if the effective radial stress became tensile, and also, sand grains would flow into the well.

An equation was presented by Weingarten and Perkins (1995) defining tensile failure and induced sanding condition regarding wellbore pressure, pressure drawdown, frictional angle and formation rock cohesion (based on the Mohr-Coulomb criteria) and presupposing

spherical geometry for perforation cavity. In their work, dimensionless curves were supplied in order to establish the pressure drawdown at a particular wellbore pressure.

Ong et al. (2000) created an analytical paradigm to forecast the commencement of sand production or critical drawdown pressure in high-rate gas wells. This defines the open-hole cavity stability and perforation that combines both fluid and rock mechanics' fundamentals. The pore pressure gradient was computed in this paradigm by applying the non-Darcy gas flow equation, coupled with the stress state for a perfect Mohr-Coulomb material. Moreover, it was presupposed that sand production would commence when drawdown pressure condition induced tensile stresses over the cavity face.

The analytical poroelastoplastic paradigms were presented by Yi et al. (2004) and based on sphere geometries and the thick-walled hollow cylinder. On the basis of these, the sand production forecasting paradigms, by assuming shear failure, induced tensile stress and sanding. The paradigms may be applied in order to study sand production from an open-hole well or a perforation tunnel and tip for a cased well.

Hayavi and Abdideh (2017) obtained an analytical sanding onset forecasting paradigm according to the theory of poroelastoplasticity, and presupposing that tensile failure caused sanding from the plastic area adjacent to the perforations of a gas well.

Morita et al. (1989a, 1989b) presented a sand production stability diagram according to pore pressure gradient and drawdown where it is possible to predict the compressive (shear) and/or tensile failures and sand-free production.

Finally, a type of sand production paradigm is based on mechanisms of erosion (Vardoulakis et al., 1996; Geilikman and Dusseault, 1997). Fluid velocity in these paradigms becomes a significant aspect, and the mechanism of erosion enables granular solids to permeate interconnected void spaces. Moreover, matrix defects are considered to be the cause of erosion (Nouri et al., 2006).

2.1.5.4 Numerical methods

Certainly, the most efficient tools in sand production forecasting are numerical models. They may be merged with analytical correlations in order to receive more effective

results. Furthermore, laboratory results are used to authenticate or calibrate a numerical model.

In order to model sand production, it is necessary to couple two mechanisms. The first of these is the degradation and the mechanical instability, with the second being the hydromechanical instability caused by the flow-induced pressure gradient on degraded material surrounding the cavity; for example, open-hole and perforation. The numerical approaches in the mechanical modelling are usually categorised under both discontinuum and continuum methods. In order to simulate the above-mentioned two mechanisms, it is necessary to couple the continuum or non-continuum methods with the CFD.

The Finite Difference Method (FDM) and the Finite Element Method (FEM) are usually utilized in the continuum approach and they are more popular for field-scale problems. Matters in the continuum method are regarded as being continuous in obtaining the governing differential equations. By assuming continuity, it is implied that it is impossible to separate the material or break it in to smaller parts. Where discontinuity exists, the deformation magnitudes across or along the discontinuity are similar to the remaining continuum (Jing & Stephenson, 2007). The DEM is effective in simulating sand production, particularly in comprehending the sanding mechanism.

In order to capture the physical behaviour of the material, continuum paradigms are based on different presuppositions, sanding criteria, constitutive laws and numerical processes having various complexity levels. Several researchers initially computed the onset of mechanical failure or the commencement of sand production. However, at a later date in 1996, Vardoulakis et al. suggested a fundamental theory for hydrodynamic erosion of sandstone on the basis of filtration theory, but with no necessity to solve the equilibrium equation. Further in 1998, Papamichos and Stavropoulou merged the evolution of localised deformation with hydrodynamic erosion. For many researchers, this marked the start of the acceptance of the full-strength softening/hardening behaviour of sandstone in their models (Papamichos et al., 2001; Vaziri et al., 2002, 2008; Detournay et al., 2006; Nouri et al., 2006, 2007, 2009; Detournay, 2008; Kim et al., 2011). Since the results are particularly mesh-dependent for strain softening material, it is essential to apply a regularisation technique. This would include an internal length, associated with grain size in the formulation. For cavity failure adjacent to boreholes, Papanastasiou and Vardoulakis (1992) used the Cosserat microstructure technique (Papanastasiou and Vardoulakis,1992; Muehlhaus and

Vardoulakis, 1987), whereas for thick-walled cylinders, Zervos et al., (2001) considered gradient elastoplasticity. Furthermore, the fracture energy regularisation method (Crook et al., 2003) was used by Nouri et al. (2009), Rahmati et al. (2011) and Wang et al. 2011 in their sand production modelling.

As aforementioned, it is impossible for traditional conventional continuum method to capture local discontinuous phenomena since sand production is a dynamic and continuous procedure, happens at a microscopic scale in which the rock becomes a discontinuum in nature. Consequently, a discontinuum (DEM) method shows encouragement to model phenomena like the detachment of separate particles from the rock matrix.

The principal pros of the DEM models is their ability to capture the interaction and motion of each sand grain as well as their failure at micro scales in a dynamic procedure. Therefore, the model is able to predict much authentic physical behaviour, This includes: behaviour which changes its character with stress state, continuous non-linear strain-stress response, militancy dependent on history, memory of previous strain or stress excursion in both direction and magnitude, hysteresis at loading/unloading, initial states, and mean stress. As far as we are aware, no continuum constitutive models which reproduce all of these behavioural types exist. Nevertheless, as the DEM concerns numerous separate particles and interactions between them, it is computationally costly; consequently, it cannot be applied to major problems. Since it is impossible to produce a model which has a precisely identical particle arrangement as the real material, it is a difficult task to calibrate the model, which also involves numerous uncertainties.

The full details of DEM method are described in Chapter 3 and the numerical studies done on sanding problem in the literature using the discontinuum approach (DEM) are provided in Chapter 6, Section 6.1.

2.2 Oil wells

In real field conditions, reservoir rock (sandstone) forms through deposition of sediments derived from pre-existing rocks and mineral particles. Further, sediments move down from the Earth's surface to the underground and diagenetic processes starts. During the diagenesis of organic matter, the kerogen chemical bonds – cementation appears between

sediment grains, and it depends on burial depth and time, temperature and pressure. After, compaction (consolidation) process due to increase in depth and overburden pressure takes a place. At the final stage, a lithification process happens, where the cemented sediment converts into sandstone. The depositional, diagenesis and lithification processes of the reservoir sandstone take several hundred million years. Then an oil well is drilled, completed and perforated, and from this moment hydrocarbon production begins. However, when producing for younger and shallow sedimentary formations, sand production is usually problematic. Slightly cementitious matrix material that binds sand particles is contained in the young reservoir sandstone formations which are frequently regarded as being “poorly consolidated” or “unconsolidated”.

The configuration of the system considered in the sand production simulations based on the well geometry and design, its trajectory in the formation, and the way it is completed. In general, there are 4 types of well geometry with its trajectory (Figure 2.5):

1. Vertical well – the most basic and widely used model is a vertical well that fully penetrates the reservoir producing interval.
2. Horizontal well - is well is where the reservoir section is drilled at a high angle, generally with a trajectory in order to keep the well inside a hydrocarbon zone or a particular reservoir interval. Although these wells are rarely perfectly horizontal, they do tend to be almost horizontal, usually at an angle of over than 80° from the vertical. Their objective is to maximise reservoir contact in order to increase productivity.
3. Slanted wells - are designed similarly to horizontal wells for the purpose of maximising reservoir contact in order to increase productivity. However, the slanted well, while crossing the communication length totally, maximises it with the formation; however, even zero vertical permeability formations are connected to the well over the total thickness.
4. Multilateral well – involves at least two laterals (horizontal, vertical or deviated) drilled from a principal mother well, thereby enabling one well to produce from many reservoirs. Such wells are appropriate for complex geology in which case it is uneconomical to drill new wells to penetrate to those reservoirs. It is possible to utilise lateral sections to produce from a separated section in layered, faulted, depleted and heavy oil reservoirs.

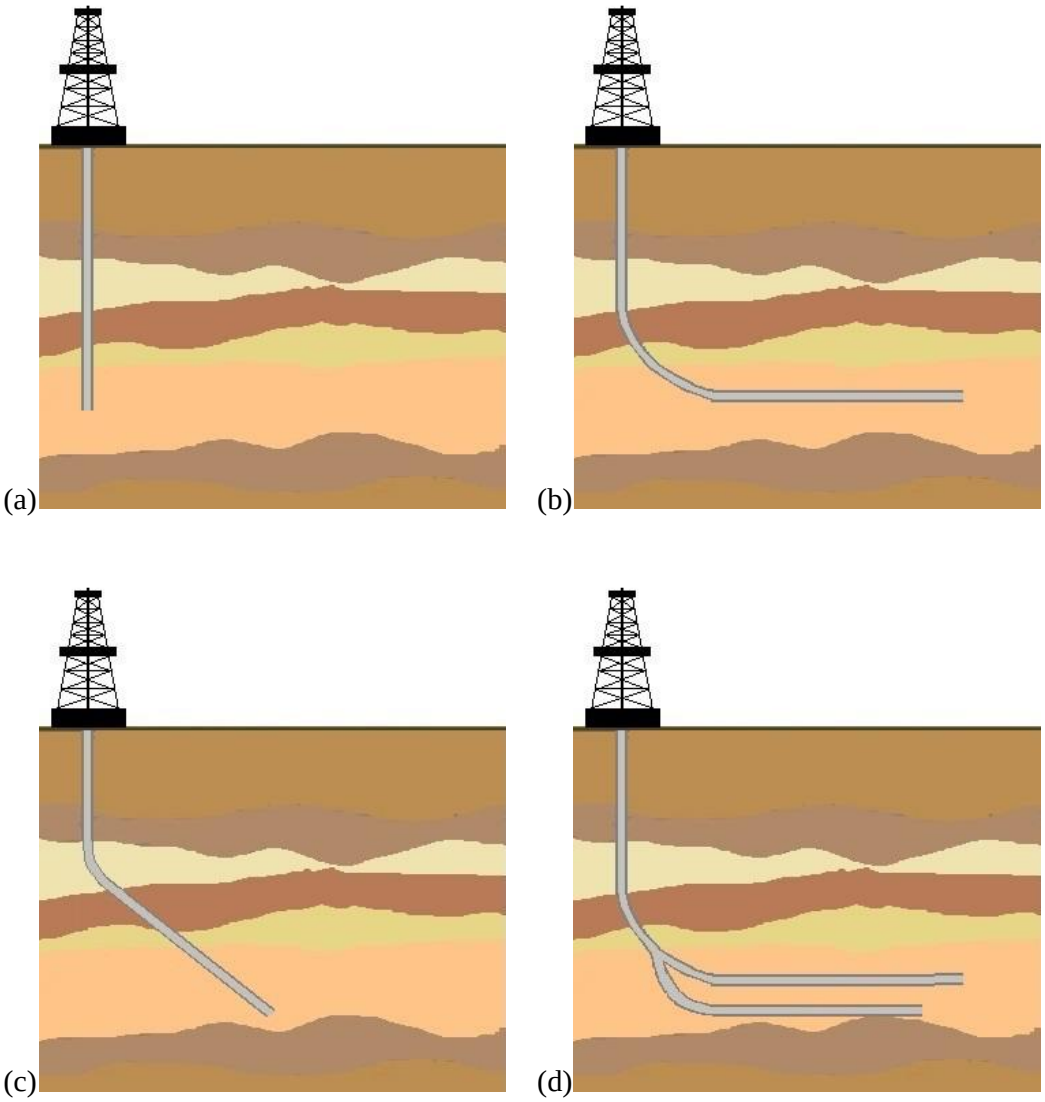

Figure 2. 5. Types of wellbore orientation: (a) vertical; (b) horizontal; (c) slanted; (d) multilateral

Based on the orientation of the wellbore and the stress concentration surrounding it, the in-situ stress magnitudes and directions, rock strength and its failure types (compressive and tensile) will change.

As soon as the location of the rig, where the well needs to enter the reservoir, and its design and trajectory are selected the well-drilling procedure will commence. Furthermore, the most frequently used technique of drilling wells utilises rotary drilling. In this method, a drilling bit is attached to the end of a long string of jointed, hollow drill pipe, and then a motorised turntable rotates the entire assembly at the surface, namely the rotary table. The

rotating bit then crushes or cuts the rock. The mud, which is drilled comprises solids, water or an oil-water mixture and different additives, is circulated down through the drill pipe and subsequently out through nozzles within the drilling bit. The mud then moves up the annulus, the space outside of the drill pipe, and returns to the surface. In this process, the mud lubricates the bit, thereby preventing it from becoming excessively hot as a result of friction and lifts the drilled rock cuttings up the hole. It ought to be sufficiently dense to overbalance any high-pressure formations encountered in the drilling process.

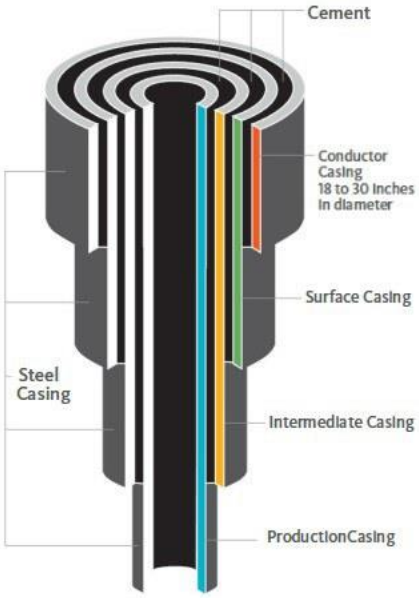

Figure 2. 6. Vertical well design (adopted from devonenergy.com)

Figure 2.6 depicts the most frequently used well design where the initial tubular – *conductor casing* is installed by a civil engineer prior to the arrival of the rig on site, the subsequent phases being drilled by using the rotary drilling method. The unconsolidated surface formations are sustained by the *surface casing* which also protects the groundwater. The purpose of the *intermediate casing* is to protect the well from the fluid or formations which could prevent the continuation of the drilling procedure. Finally, the *production casing* enables the reservoir to be isolated. The well completion begins at the last phase when the well enters the reservoir.

In the well completion procedure, a well is prepared for production (or injection) following drilling operations by installing the equipment and any additional items in order to control the fluid flow. When the drilling procedure is complete, the drilling mud fluid is

replaced by a completion fluid, usually salt water, whose purpose is to control a well if downhole hardware fails without damaging the completion components or producing formation.

The well completion comprises *lower* and *upper completion*. *Lower completion* (or reservoir) connects the wellbore with hydrocarbon formation, whereas *upper completion* supplies a connection between the surface and the lower completion. The well-completion stages include the following: cementing, casing, gravel packing (lower completion), perforating, as well as installing a production tree, sleeves, packers, landing nipples, safety valves and landing nipples (upper completion). The upper completion is outside the range of this PhD thesis, therefore, in this research I concentrated exclusively on the lower completion type.

Two types of completion techniques used on wells at the reservoir level are *open-hole* and *cased-hole completions*.

An *open-hole completion* means a well that is drilled to the top of the hydrocarbon reservoir which is subsequently cased at this level and left open at the bottom. Open-hole completions reduce the cost of casing where the reservoir is well-known and solid, thereby minimising expenses, and if the well is deepened later, enabling flexible treatment options; although such completions limit well fluid control. Furthermore, this is well adapted with well consolidated reservoirs, when the well produces exclusively from one reservoir layer, which is especially well adapted for gas wells.

Cased-hole completion involves casing and liner completions. A *cased-hole completion*, casing (casing string), is set through the producing reservoir and cemented into place, whereas a casing string within a well extends from the surface to a setting depth. *Cementing* involves pumping cement slurry into the well in order to displace the existing drilling fluids. This also fills in the space between sides of the drilled well and the casing, which positions the casing into place permanently.

Casing is needed for the cased-hole completions to run into the reservoir. Furthermore, if hydrocarbons are to be produced, it is necessary to perforate the casing, and to cement by using various techniques such as abrasion, bullet gun, shaped charges and water jets. The size, height and density (measurement of the perforations made per unit length of the gun) and phasing (the angle between the charges) vary according to the different techniques utilised for perforation. The following factors influence the choice of method:

compressive strength, fracture pressure, mineral content of the rock metric, rock properties, reservoir pressure, tectonic stress and overburdened reservoir pressure, completion fluid, reservoir fluid and temperature and wellbore configurations; for instance, grade and size of casing, wellbore deviation and orientation.

The most frequently applied technique utilised jet perforating guns equipped with shaped explosive charges (Chapter 6, Section 6.2). During the *perforation* procedure, a reservoir locating gun and a perforation gun are run into the wellbore several times through a slickline, wireline or coiled tubing. On reaching the reservoir level, the gun shoots holes into the sides of the well, enabling the hydrocarbons to enter the well stream.

Behrmann et al. (2000) stated that in authentic field conditions, oil wells are perforated by a shaped charge perforation gun using military technology in less than one second. This comprises a main explosive, a detonating cord, a conical metal liner, a primer and an outer case. The conical metal liner, whose purpose is to maximise the penetration, is connected to a detonating cord which initiates the primer, and then detonates the principal explosive. The conical metal liner collapses, thereby forming a high-velocity jet of fluidised metal particles that is propelled along the charge axis. This jet comprises a slower tail that moves at below 1 km/sec, and a faster one which moves at approximately 7 km/sec by particularly high impact pressures of around 20 GPa on the casing and 2 GPa on formations causing rock, cement, steel, cement, and pore fluids to flow plastically outward in a particularly short time.

The perforation may be undertaken in four conditions according to the pressure difference (prior to the perforation procedure) between wellbore and reservoir: underbalanced, balanced, overbalanced and extremely overbalanced (Behrmann et al., 2000). The underbalanced perforation condition currently minimises and removes the perforation damages; therefore, this technique is broadly applied.

1. *Underbalanced perforation* – wellbore pressure is less than reservoir pressure.
2. *Balanced perforation* – reservoir and wellbore pressure are the same.
3. *Overbalanced perforation* – wellbore pressure is higher than reservoir pressure.
4. *Extremely overbalanced perforation* – wellbore pressure is considerably higher than rock strength and reservoir pressure.

2.3 Summary

This chapter provides a general overview to sand production problem in oil and gas fields. It defines the main perils caused by sand production problem happening worldwide and how operators overcome it by existing sand management and control techniques. Furthermore, factors, parameters, and types of mechanisms which lead to sanding phenomenon are listed. Finally, developed empirical, analytical, numerical, and experimental methods reviewed from the literature and the main pros and cons of each method are given.

Chapter 3 – Numerical methodology

3.1 Introduction

A DEM fluidised bed simulation code was developed by Kafui et al. (2002) at Birmingham University. They achieved this by coupling the DEM code which was written by Cundall and Strack (1979) and the CFD code which was provided by Kuipers et al. (1993). The CFD code was based on 2D and 3D Navier-Stokes equations for compressible flows. Moreover, the IBM technique was integrated into this CFD-DEM code by Guo et al. (2012) in order to model particle and gas two-phase flows with moving and complex boundaries.

This research uses the 3D CFD-DEM-IBM code, in which the IBM code was optimized for the sand production modelling geometry. Since the CFD-DEM sand production modelling exclusively concerns incompressible fluids as in real field conditions, the 2D and 3D Navier-Stokes equations for compressible flow have been changed to incompressible flow. In this study, every DEM sand particle is regarded as being frictional and elastic. In all simulations (triaxial compression, cone penetration tests and sand production) the theories of Hertz (1881) and Mindlin (1941) are used to calculate the normal and tangential interparticle and particle-LSO (Large-Sized Objects, and it is considered only in sand production simulations) contact forces without adhesion, respectively. For the case with adhesion, a simple 3D contact bond model for cemented sandstone material has been developed which simply modified the previous existing JKR model (Johnson et al.,1971; Johnson, 1976) for auto-adhesive silt sized particles. This contact bond model was utilised to compute the interparticle normal contact force with adhesion and no-slip model (Mindlin, 1949) to calculate the tangential interaction force.

This chapter is organized as follows. The theoretical background of granular dynamics and assembly mechanics are given in Section 3.2. The full set of required equations (particle kinematics, damping, time step, contact forces) to investigate 3D DEM simulations are provided. Furthermore, the derivations of the stress and fabric tensors, coordination number, and assembly modulus are given. All the information presented in Section 3.2 is obtained from Thornton (2015). Contact mechanics and a developed simple 3D bond contact

model for cemented sandstone material are provided in Section 3.3. The governing equations used for the coupled CFD-DEM-IBM modelling (incompressible flow solver) are presented in Section 3.4. Section 3.5 describes numerical solutions of DEM and hydrodynamics models, and Section 3.6 provides information on boundary conditions for DEM, CFD and IBM models.

3.2 Discrete Element Method

3.2.1 Particle kinematics

The components (i = 1, 3) of the rotational and translational accelerations of each particle in a large particles' system are shown by the following equations:

$$\frac{dv_i}{dt} = \frac{\sum F_{ci}}{m_i} + g_i \tag{3.1}$$

$$\frac{d\omega_i}{dt} = \frac{\sum F_{ti} R}{I} \tag{3.2}$$

where F_c represents the contact forces that act on the particle, with $F_t R$ being the moments due to the tangential components of the contact forces, ω and v are the angular and linear velocity of the particle respectively. The acceleration due to any gravity field is g, and I represents the moment of inertia. For a solid sphere, $I = \frac{2}{5} m R^2$.

By applying a specific central finite difference scheme and by combining Equations 3.1 and 3.2, new particle positions and velocities are calculated by the following equations:

$$v_i^{new} = v_i^{old} + \frac{dv_i}{dt}\Delta t \qquad \text{and} \qquad \omega_i^{new} = \omega_i^{old} + \frac{d\omega_i}{dt}\Delta t \tag{3.3}$$

$$x_i^{new} = x_i^{old} + v_i^{new}\Delta t \qquad \text{and} \qquad \theta_i^{new} = \theta_i^{old} + \omega_i^{new}\Delta t \tag{3.4}$$

where θ_i and x_i represent the components and coordinates of the particle's angular rotation, and Δt is the small time step applied in order for the advancement of the simulation. New contact forces may be computed from new particle velocities and locations; moreover, both

broken and new contacts ought to be examined. There is a contact for spheres A and B where the distance between their centres is below the sum of both radii; that is:

$$\alpha = R_A + R_B - D \tag{3.5}$$

where *D* being the distance between centres of the spheres, and α represents the relative approach in the normal direction.

In the case of the rotational and translational velocities of both spheres being v_i^A, ω_i^A and v_i^B, ω_i^B, the relative normal displacement increment at the contact is:

$$\Delta\alpha = (v_i^B - v_i^A)n_i\Delta t \tag{3.6}$$

with *n* being the unit vector normal to the contact plane whose direction is from sphere *A* to sphere *B*. The time step Δt will be discussed later.

The following equation gives the relative tangential surface displacement increment:

$$\Delta\delta_i = \left(v_i^B - v_i^A\right)\Delta t - \Delta\alpha n_i - (\omega_{i+1}^A n_{i+2} - \omega_{i+2}^A n_{i+1})R_A\Delta t$$

$$-(\omega_{i+1}^B n_{i+2} - \omega_{i+2}^B n_{i+1})R_B\Delta t \tag{3.7}$$

where the subscripts *i, i*+ and, *i* + 2 are rotated between the limits 1 to 3, that is if *i* = 2, *i* + 2 = 4 – 3 = 1.

3.2.2 Contact forces

The new contact may be computed when the relative incremental displacements at a contact have been acquired, and the following equation can be used to update the normal force:

$$F_n^{new} = F_n^{old} + k_n\Delta\alpha \tag{3.8}$$

Nevertheless, the application of functional form; for example, $F_n = k_n\Delta\alpha$, using double-precision arithmetic is a more appropriate option provided that the contact force

model allows this. As described below, it is necessary to update the tangential force incrementally because it is considerably more complex.

The contact plane rotates continuously during particle-particle interactions. Consequently, it is essential to reposition the tangential displacement and existing tangential force directions towards a new orthogonal contact normal direction, prior to the displacements and tangential forces being updated. The following equation gives the contact rotation:

$$\Omega_i = \left(\left(v_{i+2}^B - v_{i+2}^A\right)\Delta t - \Delta\alpha n_{i+2}\right)\frac{n_{i+1}}{D} - \left(\left(v_{i+1}^B - v_{i+1}^A\right)\Delta t - \Delta\alpha n_{i+1}\right)\frac{n_{i+2}}{D} \quad (3.9)$$

in which D indicates the distance between the centres of both spheres. The displacement and tangential force may be modified by applying these equations:

$$\delta_i = \Omega_{i+1}\delta_{t(i+2)}^{old} - \Omega_{i+2}\delta_{t(i+1)}^{old} \text{ and } F_{ti} = \Omega_{i+1}F_{t(i+2)}^{old} - \Omega_{i+2}F_{t(i+1)}^{old} \quad (3.10)$$

where δ_{ti}^{old} and F_{ti}^{old} indicate the components of the tangential displacement and tangential force prior to the contact plane rotation. Furthermore, the modified tangential displacement and force are acquired from the equations below:

$$\delta = (\delta_i\delta_i)^{1/2} \quad \text{and} \quad F_t = (F_{ti}F_{ti})^{1/2} \quad (3.11)$$

An additional difficulty emerges in 3D simulations following the understanding of the contact normal vector rotation. As indicated in Figure 3.1a, the tangential displacement increment direction, as defined by Eq. (3.7), is not usually coaxial with the old tangential displacement direction, as defined by Eq. (3.10). Vector summation gives the new tangential displacement as shown in:

$$\delta_i^{new} = \delta_i^{old} + \Delta\delta_i \quad (3.12)$$

Nevertheless, although the equation $F_t^{new} = F_t^{old} + k_t\Delta\delta$ is not strictly correct, it is used to calculate the new tangential force in most codes. In that the contact area does not change, this may be shown by taking into account a constant normal force. The non-coaxiality in this situation causes the tangential force to attain the limiting value of $F_t = \mu F_n$ at the incorrect value of δ.

The size of the tangential displacement increment, as shown in Figure 3.1, has been excessively overemphasised relative to that of the old tangential displacement for the sake of clarity. Figure 3.1 can give an initial impression that $\Delta\delta$ has two parts, one being orthogonal in the direction of δ old, and the other being coaxial with δ old. However, the reaction to this orthogonal part of $\Delta\delta$ would be questioned if this were true, whereas consideration of the cylindrical coordinates (Figure 3.1b) would provide the correct solution. Therefore, a radial tangential displacement generates a tangential reaction force, whereas a normal displacement generates a normal reaction force; moreover, a contact moment reacts to a rotational displacement, also known as a twist. Therefore, this equation is applied to update the tangential force:

$$F_t^{new} = F_t^{old} + k_t \Delta\delta_r \tag{3.13}$$

and for the scalar product

$$\Delta\delta_r = \delta^{new} - \delta^{old} \tag{3.14}$$

This equation gives the tangential force components:

$$F_{ti}^{new} = F_t^{new} \frac{\delta_i^{new}}{|\delta^{new}|} \tag{3.15}$$

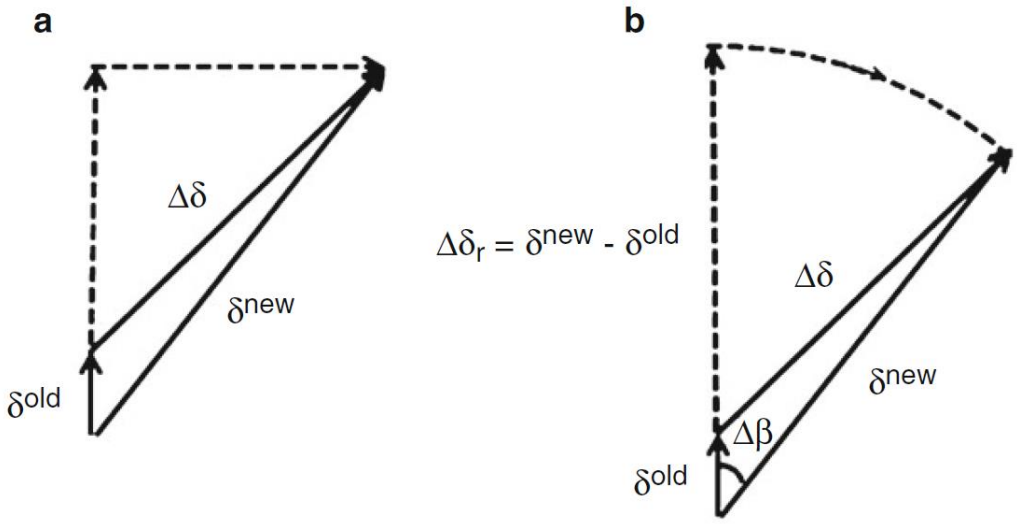

Figure 3. 1. Non-coaxiality on the contact plane for the (a) Cartesian and (b) cylindrical local (adopted from Thornton, 2015)

In the comparison between the sliding criterion and the tangential force, where the sliding force is the greater, the tangential force is reset to the limiting value $\boldsymbol{F_t = \mu F_n}$. Furthermore, Figure 3.1b depicts a rotational displacement increment shown by the angle $\Delta\beta$; nevertheless; it usual to disregard the resultant contact moment because of the small contact area. The contact stiffnesses k_n and k_t as shown above, and which depend on the contact force model that is used, are the current stiffnesses.

3.2.3 Time step

Although a particle has the potential to collide with walls or with adjacent particles during its movement, such movement is influenced by other particles remote to its local neighbourhood by the propagation of disturbance waves. The selection of a small value that is appropriate to the time step resolves this difficulty, in that in the course of a single time step, a disturbance can propagate only from one particle to others in its vicinity. However, when the contact stiffness is modelled by linear springs, the ratio of the particle density to the contact spring stiffness is associated with the critical time step. Furthermore, in the case of non-linear springs it is theoretically impossible to calculate the critical time step (a Hertzian spring). Nevertheless, Miller and Pursey (1955) demonstrated that the Rayleigh waves represent 67% of the radiated energy when compared with the distortional (26%) and the dilational waves (7%). The Birmingham DEM code assumes that the Rayleigh waves transfer all the energy. The difference between the Rayleigh wave speed and the distortional wave speed and is exceptionally small, with the energy that the dilational wave transfers being negligible; therefore, this is an appropriate estimation. Furthermore, the average time at which the Rayleigh wave arrives at any contact remains constant, whatever the contact point location. For an assembly of many particles, it can be derived that the highest frequency of Rayleigh wave propagation is determined by the smallest spheres which gives the critical time step:

$$\Delta t_c = \frac{\pi R_{min}}{v_R} = \frac{\pi R_{min}}{\lambda}\sqrt{\frac{\rho}{G}} \tag{3.16}$$

where $v_R = \lambda\sqrt{\frac{G}{\rho}}$ is the Rayleigh wave speed, G is the particle shear modulus, ρ is the particle density, R_{min} is the minimum particle radius, and λ can be obtained from:

$$(2-\lambda^2)^4 = 16(1-\lambda^2)\left[1-\lambda^2\left(\frac{1-2\nu}{2(1-\nu)}\right)\right] \tag{3.17}$$

which may be estimated by

$$\lambda = 0.8766 + 0.1631\,\nu \tag{3.18}$$

in which ν is Poisson's particle ratio.

In Eqn. 3.16 it is assumed that the property type of all constituent particles is the same. However, if there are different material types for the constituent particles, the critical time step for the highest Rayleigh wave frequency should be the lowest among those determined by different material types.

The actual time step used in Birmingham code is a multiple of the Rayleigh critical time step by a value of *FRAC* which is normally given less than 1. It has been shown that for most cases, the time-step based on the Rayleigh wave speed can ensure the numerical stability of simulations. However, for the simulation of some dynamic problems such as the agglomerate impact, the Rayleigh time step may not be small enough to guarantee numerical stability. This is because for the above Rayleigh wave propagation-based time step, the relative movements between spheres are not considered. Since the relative velocity between the spheres of an impacting agglomerate may be very high, the Rayleigh wave transmission through the assembly along each sphere surface will be greatly affected. As a result, the critical time step of real Rayleigh wave transmission is much smaller, and the Rayleigh wave time step based on the static assembly does not apply to the dynamic assembly anymore. When numerical instability occurs during the simulation of dynamic particle systems, the time step needs to be further reduced by using the FRAC command. An exception when the time step can be used to exceed the Rayleigh wave speed based critical time step is for the simulation of very loose particle systems. For a very loose particle systems, usually there are very few contacts between particles. Because of this, force transmission in loose particle systems is not yet established. As a result, a relatively larger time step can be used to speed up the process of bringing the particles together. It is advisable, however, to continuously monitor the system when using *FRAC > 1*.

3.2.4 Damping

Particulate systems are not energy conserving. From the external applied field such as wall-controlled boundaries and/or strain controlled periodic cells, the particle system gains energy which causes problems for the simulations of quasi-static systems (shear testing, preparation of agglomerate). In such cases, damping is needed to dissipate energy stored into the system and in consequence to reduce the computational time required by the particles system to reach its quasi-equilibrium state.

The Birmingham code uses a form of viscous damping – contact damping. The contact damping is important for a simulated assemlbly to reach quasi-equilibrium. Without it, the contact forces between particles will continue to oscillate infinitely.

The Birmingham code, unlike most of the other DEM codes, does not contain a dashpot force as a portion of the contact force. Nevertheless, as a result of elastic wave propagation through a solid particle, some dashpots are utilised in order to disperse a small amount of energy (the contact damping considers the energy losses during the force transmission through the solid particles). Although the dashpot forces are not regarded as being part of the real contact forces, they are added to the tangential contact forces and to the normal forces in order to supply the out-of-balance moment and force which, from that contact, act on the particle, as used in Equations 3.1 and 3.2.

The normal and tangential damping forces are as follows:

$$F_{nd} = 2\beta\sqrt{m^* k_n}\Delta\alpha/\Delta t \tag{3.19}$$

and

$$F_{td} = 2\beta\sqrt{m^* k_t}\Delta\delta/\Delta t \tag{3.20}$$

with

$$\frac{1}{m^*} = \frac{1}{m_A} + \frac{1}{m_B} \qquad \text{and} \qquad \beta = \frac{frac}{2\pi \cdot freq} \tag{3.21}$$

in which m_A and m_B are the masses of the two particles, whereas the value of β with the parameters of Rayleigh damping: *frac* is the fraction of critical damping at the modal frequency *freq*). The damping parameters were specified for ball-to-ball contact (*frac* = 0.05

and *freq* = 0.5) and for ball-to-wall contact (*frac* = 0.1 and *freq* = 0.5). Nevertheless, the contact damping forces contribu#te only to the particle's out-of-balance force from which the particle acceleration is acquired, and not to the stored contact forces (Cundall and Strack, 1979). In addition to the damping mechanism, energy of the simulated particle system may also be dissipated by interparticle friction and contact breaking.

3.2.5 Stability consideration

There is a connection between the average number of contacts per particle and the structural stability of a system of particles, showing that the coordination number $Z = 2C/N$ where the number 2 indicates that each contact is shared by two particles, and where N is the number of particles and C is the number of contacts (Thornton, 2000). Therefore, in a 3D system of particles where $\mu = \infty$, there is no sliding at any contact. There are six degrees of freedom in a single particle, comprising three translations and three rotations, with the total number in the system being 6N. At a single contact, the number of constraints, otherwise referred to as unknown reactions, is 3, being a normal force, a contact moment and a radial tangential force, making the total number in the system to be 3C. In some cases, the total number of constraints and the total number of degrees of freedom is equal ($3C = 6N$). Therefore, when this applies, the system is statically determinate (isostatic); furthermore, the critical coordination number $Z_c = 4$ can be defined if $Z > Z_c$. This means that the system is indeterminate (hypostatic) and the number of contacts required to guarantee stability is more than necessary, and the system is redundant. However, it is impossible to satisfy the equilibrium if $Z < Z_c$, which is because the number of contacts needed to maintain the stability of the system is fewer, resulting in the system becoming mechanism (hyperstatic).

However, it is not necessarily suitable to define the coordination number as $Z = 2C/N$ because it is apparently the coordination number which includes particles without contacts. The geometrical coordination number can be defined as:

$$Z_g = \frac{2C}{(N - N_0)} \tag{3.22}$$

in which N_0 is the number of particles without contacts. Although this coordination number may be effective in characterising agglomerates or clusters, the definition includes particles having only one contact which do not contribute to the system's stability. Therefore, a mechanical coordination number is defined in order to examine the stability:

$$Z_m = \frac{(2C - N_1)}{(N - N_1 - N_0)} \tag{3.23}$$

in which N_1 is the number of particles having only one contact. Therefore, a system is defined as being isostatic when $Z_m = 4$.

The aforementioned case is limiting, whereas the other limiting case is when $\mu = 0$ where there are no particle rotations, in which case the only constraint at a contact is the normal force. Therefore, in a case where $\mu = 0$, the isostatic state corresponds to $Z_m = 6$. The interparticle friction is finite in simulations as well as in reality; therefore, the critical value of Z_m is dependent on the percentage of sliding contacts. However, it is an arduous task to determine precisely what the value ought to be; nevertheless, $Z_m = 4$ *can be assumed* to be the lower bound.

Another method is to define a redundancy index IR which is a function of the fraction of the sliding contacts. The redundancy index might be defined as the ratio of the number of constraints to the number of degrees of freedom in the system. However, when sliding occurs, this allows for the reduced number of constraints. Consequently, if, in 3D, the contact moment mentioned in Section 3.2.2 is disregarded, then:

$$I_R = \frac{C}{N}\left(\frac{3-2f}{6}\right) \tag{3.24}$$

in which f is the fraction of sliding contacts; for example, 0.10. However, if $I_R = 1$ the system is isostatic, if $I_R > 1$ it is hypostatic and if $I_R < 1$ it is hyperstatic. If the particles without contacts will be disregard, and the number of particles having only one contact is negligible, then the Equation 3.24 can be rewritten as:

$$I_R = Z_m\left(\frac{3-2f}{6}\right) \tag{3.25}$$

3.2.6 Microstructure

It is generally accepted that the closeness of the packing of the individual particles has a powerful impact on the mechanical behaviour of granular material. Therefore, granular material is usually characterised by a scalar parameter; for example, solid fraction, porosity or void ratio. Nevertheless, it is now common knowledge that the microstructure of granular materials needs a tensorial description because it is anisotropic. Satake (1982) claims that, for sphere or disc systems, the structural anisotropy can be defined by the orientational distribution of contact normals (n_i) which we can identify by a second-order fabric tensor ϕ_{ij}.

$$\phi_{ij} = \frac{1}{2C}\sum_1^{2C} n_i n_j = \langle n_i n_j \rangle \tag{3.26}$$

where *C* represents the total number of contacts, which are counted twice because each of them belongs to two particles. The direction cosines of a unit contact normal vector for sphere and disc assemblies are given by:

$$n_i = (x_i^A - x_i^B)/(R^A + R^B) \tag{3.27}$$

where x_i^A and x_i^B indicate the positions of the centres of both contacting particles of radii, R^A and R^B. Although consideration may be given to higher-order fabric tensors like $\phi_{ijkl} = \langle n_i n_j n_k n_l \rangle$, DEM simulations have demonstrated that a second-order representation, as shown in Equation 3.25, is acceptable. However, provided that we consider a continuous distribution of contact normal vectors we may also write:

$$\phi_{ij} = \int_\Omega \mathrm{E(n)n_i n_j d\Omega} \tag{3.28}$$

which satisfies the conditions

$$\int_\Omega \mathrm{E(n)d\Omega} = 1 \qquad \text{and} \qquad \mathrm{E(n)} = \mathrm{E(-n)} \tag{3.29}$$

where *E(n)* represents the probability density function of contact normal, whereas *E(n)dΩ* indicates the estimated rate of *n*, the directions of which are within a small solid angle *dΩ*. We can express the probability density function as a Fourier series which, in tensorial format:

$$E(n) = E_0 + E_{ij} f_{ij} \tag{3.30}$$

where

$$f_{ij} = n_i n_j - \frac{\delta_{ij}}{3} \tag{3.31}$$

The Fourier coefficients are given by:

$$E_0 = \frac{1}{4\pi} \int_\Omega E(n) d\Omega = \frac{1}{4\pi} \tag{3.32}$$

$$E_{ij} = \frac{15}{8\pi} \int_\Omega E(n) f_{ij} d\Omega = \frac{15}{8\pi} \langle f_{ij} \rangle = \frac{15}{8\pi} (\phi_{ij} - \frac{\delta_{ij}}{3}) \tag{3.33}$$

These coefficients are totally symmetric and traceless, as well as transforming as tensors under rigid body rotations. In 2D systems we may write:

$$\phi_{ij} = \int_0^{2\pi} \int_\Omega E(\theta) n_i n_j d\theta \tag{3.34}$$

in which θ is the inclination angle of n with respect to the reference axis and

$$E(\theta) = E_0 + E_{ij} f_{ij} \tag{3.35}$$

$$\text{with } E_0 = \frac{1}{2\pi} \int_0^{2\pi} E(\theta) d\theta = \frac{1}{2\pi} \quad \text{and} \quad E_{ij} = \frac{2}{\pi} \int_0^{2\pi} E(\theta) f_{ij} d\theta = \frac{2}{\pi} \langle f_{ij} \rangle \tag{3.36}$$

E(θ) can also be expressed as:

$$E(\theta) = \alpha_0 + \alpha_2 \cos(2\theta) + b_2 \sin(2\theta) \tag{3.37}$$

with

$$\alpha_0 = \frac{1}{2\pi}; \; \alpha_2 = \frac{2}{\pi} \langle f_{11} \rangle = \frac{2}{\pi} (\phi_{11} - \frac{1}{2}); \; b_2 = \frac{2}{\pi} \langle f_{12} \rangle = \frac{2}{\pi} \phi_{12} \tag{3.38}$$

If a second-order Fourier series representation is assumed, it is of interest to observe that this suggests there are restrictions on the level of anisotropy which may be defined in 2D by the deviator fabric $(\phi_1 - \phi_2)$. If the main anisotropy axes coincide with the reference axes then:

$$E(\theta) = \frac{1}{2\pi} + \alpha_2 \cos(2\theta) \tag{3.39}$$

Since it is impossible for *E(θ)* to be negative, we regard *E(θ) = 0* at $\theta = \pi/2$ as being the limit condition, and also by applying Equation 3.38, ϕ_1 = 0.75 and ϕ_2 = 0.25 will be obtained. Therefore, 0.5 is the maximum deviator fabric that is possible. In 3D, a similar exercise produces a corresponding maximum deviator fabric of 0.25 where there is axisymmetric compression.

3.2.7 Stress

In certain circumstances, particle systems act as a solid, while at other times, they act as like a liquid. The state of stress is generally defined by this equation:

$$\sigma_{ij} = p\sigma_{ij} + \frac{1}{2V}\sum^{N_p} m\hat{\dot{x}}_i\hat{\dot{x}}_j + \frac{1}{V}\int \sigma_{ij}^{p} dV \tag{3.40}$$

where *V* represents the volume of the system containing N_p particles, *m* indicates the mass of a particle having a fluctuating velocity $\hat{\dot{x}} = \dot{x} - \langle\dot{x}\rangle$, and σ_{ij}^{p} represents the average state of stress within a particle.

The first expression, shown on the right, is the result of the fluid pressure *p* which contributes to the stress tensor isotropic component. The second expression represents the fluctuating kinetic energy density, also referred to as the Reynolds stress, and associated with what is known as 'granular temperature' which is generally anisotropic. The third expression indicates the Cauchy stress which is caused by interparticle interactions, either enduring or collisional. The drag forces, particle collision forces and lift forces, or, in fact, any other factor that causes the particles to deviate from the fluid streamlines, lead to fluctuating velocities. The second expression is negligibly small in the case of quasi-static deformation of compact systems, where particle systems are continuous, and the effective stress, σ'_{ij} , as it is known in soil mechanics, can be defined as follows:

$$\sigma'_{ij} = \sigma_{ij} - p\sigma_{ij} = \frac{1}{V}\int \sigma_{ij}^{p} dV \tag{3.41}$$

For a single particle, the average stress tensor may be expressed as follows:

$$\sigma_{ij}^{p} = \frac{1}{V^P} \int \sigma_{ij}\, dV^P \tag{3.42}$$

in which V^P is the volume occupied by a single particle (it should be borne in mind that the volume which the particle V^P occupies is not the particle's solid volume, but that it also includes the portion of the void volume which is nearer to the particle than it is to any other particle). The Divergence Theorem may be applied to replace the volume integral by the surface integral, thereby giving:

$$\sigma_{ij}^{p} = \frac{1}{V^P} \int x_i\, t_j dS \tag{3.43}$$

If the tractions t_j are regarded as comprising the discrete forces F_j which act at point contacts that are defined by the coordinates x_i, we may replace the integral in Equation 3.43 by a summation over the n contacts of particle *p*. Therefore

$$\sigma_{ij}^{p} = \frac{1}{V^P} \sum_1^n x_i\, F_j \tag{3.44}$$

The effective stress is not continuously distributed over the system ($\sigma'_{ij} = 0$ in the voids); therefore, we may rewrite Equation 3.41 as:

$$\sigma'_{ij} = \frac{1}{V} \sum^{N_p} \sigma_{ij}^{p} V^P = \frac{1}{V} \sum^{N_p} \sum^{n} x_i F_j \tag{3.45}$$

being aware that the coordinates x_i are referenced to the particle centre for each particle, and also that, for systems of discs or spheres, $x_i = R n_i$. Furthermore, it is possible to partition the contact force into the normal and tangential components, F_n and F_t, thereby, $F_{ni} = F_n n_i$ and $F_{ti} = F_t t_i$, in which n_i defines the contact normal vector, and t_i is orthogonal to n_i.

The summation is basically undertaken over the *C* contacts in the system, for polydisperse systems of spheres or discs, giving:

$$\sigma'_{ij} = \frac{1}{V} \sum^{C} (R^A + R^B) F_n n_i n_j + \frac{1}{V} \sum^{C} (R^A + R^B) F_t n_i t_j \tag{3.46}$$

or, with regard to statistical averages, we may say:

$$\sigma'_{ij} = \frac{C}{V} \langle D F_n n_i n_j \rangle + \frac{C}{V} \langle D F_t n_i t_j \rangle \tag{3.47}$$

where $D = R^A + R^B$ represents the distance between the centres of both particles in contact.

3.2.8 Assembly modulus

As Walton (1987) suggests, it is possible to formulate an equation associated with a small change in the ensemble average stress to small changes with the interparticle contact forces. Subsequently, a simplifcation of presupposition regarding the applied strain increment field can be made in order to acquire the present effective compliance/modulus, meaning that we desire to determine the following relationships:

$$d\sigma_{ij} = S_{ijkl} d\varepsilon_{kl} \qquad \text{or} \qquad d\varepsilon_{ij} = C_{ijkl} d\sigma_{kl} \qquad \text{with} \quad C_{ijkl} = (S_{ijkl})^{-1} \tag{3.48}$$

If the pore fluid pressure is assumed to be zero, then the Equation 3.47 can be written as:

$$\sigma_{ij} = \frac{C}{V} \langle D n_i F_j \rangle \tag{3.49}$$

or, in an incremental form

$$d\sigma_{ij} = \frac{C}{V} \langle D n_i dF_j \rangle \tag{3.50}$$

However, if k_n and k_t are the present normal and tangential contact stiffnesses then it can be written as:

$$dF_i = k_n n_i d\alpha + k_t d\sigma_{ri} \tag{3.51}$$

in which $d\sigma_r$ represents the relative radial tangential displacement increment at the contact and $d\alpha$ is the increment in the relative approach of both particles; therefore:

$$d\sigma_{ij} = \frac{C}{V} \left[\langle D k_n d\alpha n_i n_j \rangle + \langle D k_t d\sigma_{ri} n_j \rangle \right] \tag{3.52}$$

The incremental displacement of the sphere centres may be presupposed to be compatible with an applied uniform strain increment field, as follows:

$$du_i = d\varepsilon_{ij} X_j \tag{3.53}$$

in which ε_{ij} represents the applied strain increment tensor and X_{ij} defines the coordinates of a sphere.

The individual sphere rotations, in polydisperse spheres' system have an impact on the relative tangential displacement increment at the contact as shown in Equation 3.7. From a random perspective, these are independent of the applied strain increment tensor. Consequently, it is not easy to assimilate these into the macroscopic strain-stress description. Therefore, if we presuppose, for the sake of simplicity, that there are no particle rotations then $d\sigma_{ri} = d\sigma_i$, and that the tangential and normal relative incremental displacements at the contact are:

$$d\alpha = (du_i^B - du_i^A)n_i \tag{3.54}$$

$$d\delta_i = (du_i^B - du_i^A) - d\alpha n_i \tag{3.55}$$

however,

$$\left(du_i^B - du_i^A\right) = d\varepsilon_{ij}\left(X_j^B - X_j^A\right) = d\varepsilon_{ij}Dn_j \tag{3.56}$$

therefore,

$$d\alpha = Dd\varepsilon_{ij}n_in_j \tag{3.57}$$

$$d\delta_i = Dd\varepsilon_{ij}n_i - Dd\varepsilon_{kl}n_kn_ln_i \tag{3.58}$$

We can substitute this into Equation 3.51 to give:

$$d\delta_{ij} = \frac{C}{V}\left[\langle k_nD^2d\varepsilon_{ki}n_in_jn_kn_l\rangle + \langle k_tD^2d\varepsilon_{jk}n_in_k\rangle - \langle k_tD^2d\varepsilon_{ki}n_in_jn_kn_l\rangle\right] \tag{3.59}$$

Additionally, it is noted that the second expression may not necessarily be symmetric; therefore, we write:

$$d\delta_{ij} = \frac{C}{V}\left[\langle k_nD^2d\varepsilon_{ki}n_kn_ln_in_j\rangle + \langle k_tD^2d\varepsilon_{jk}n_kn_ln_in_j\rangle + 0.5(\langle k_tD^2d\varepsilon_{ik}n_kn_j\rangle + \langle k_tD^2d\varepsilon_{jk}n_kn_i\rangle\right] \tag{3.60}$$

By applying $d\varepsilon_{ik} = d\varepsilon_{kl}\delta_{il}$ and $d\varepsilon_{jk} = d\varepsilon_{kl}\delta_{jl}$ we obtain $d\sigma_{ij} = S_{ijkl}d\varepsilon_{kl}$ and also

$$S_{ijkl} = \frac{C}{V}\left[\langle k_n D^2 n_i n_j n_k n_l\rangle + \langle k_t D^2 n_i n_j n_k n_l\rangle \right.$$
$$+0.25(\langle k_t D^2 n_j n_k\rangle\delta_{il} + \langle k_t D^2 n_i n_k\rangle\delta_{jl}$$
$$\left.+\langle k_t D^2 n_j n_i\rangle\delta_{ik} + \langle k_t D^2 n_i n_l\rangle\delta_{jk})\right] . \quad (3.61)$$

3.3 Particle-particle interaction forces and a 3D contact bond model for cemented sandstone material

Forces are created at the particle-particle contacts due to the relative displacements between particles. The behaviour of the contact force-displacement is dependent on the surface conditions, the size of the two spheres in contact and their material properties. Contact behaviour is inclusive of every intricate type of surface physics, such as elasticity, friction and adhesion, all of which normally interact simultaneously in a complicated geometrical plan (Thornton, 2015).

3.3.1 Without adhesion

For frictional elastic spheres with no adhesion, the theories presented by Hertz (1881), and Mindlin (1949) define the normal and tangential stiffnesses respectively. The Hertz' theory applies the normal force F_n to the relative approach α of the centres of both adjacent spheres with radii R_i and elastic attributes E_i, G_i and ν_i $(i = 1, 2)$

$$F_n = \frac{4}{3}E^*\sqrt{R^*\alpha^3} \quad (3.62)$$

in which

$$\frac{1}{R^*} = \frac{1}{R_1} + \frac{1}{R_2} \quad (3.63)$$

and

$$\frac{1}{E^*} = \frac{1-\nu_1^2}{E_1} + \frac{1-\nu_2^2}{E_2} \tag{3.64}$$

From these equations, the normal contact stiffness is

$$k_n = 2E^*\sqrt{R^*\alpha} \tag{3.65}$$

The tangential force, which is computed incrementally, is dependent on whether the normal forces are decreasing or increasing (Thornton, 2015). We obtain the tangential force at the i^{th} timestep from the following equation:

$$F_t^i = F_t^{i-1} + k_t^i \Delta\delta \quad \text{if} \quad \Delta F_n \geq 0 \tag{3.66a}$$

or

$$F_t^i = F_t^{i-1}\left(\frac{k_t^i}{k_t^{i-1}}\right) + k_t^i \Delta\delta \quad if \quad \Delta F_n < 0 \tag{3.66b}$$

However, if $F_t \geq \mu F_n$, then $F_t = \mu F_n$ (3.66c)

We define the contact stiffness by:

$$k_t = 8G^*\sqrt{R^*}\alpha \tag{3.67}$$

as the Mindlin (1949) 'no-slip' solution, where

$$\frac{1}{G^*} = \frac{2-\nu_1}{G_1} + \frac{2-\nu_2}{G_2} \tag{3.68}$$

3.3.2 With adhesion

Johnson et al. (1971) proposed the JKR model of adhesion in order to model auto-adhesive interactions as a result of the van der Waals forces between silt-sized particles. Nevertheless, the oil field formation rock is sandstone, meaning that it is sand with cement bonds. In this study, a simple modification of the JKR model has been made to calculate the normal contact force, and for the tangential contact force, the no slip model of Mindlin's

(1949) is used. Johnson (1976) provided the connection between the relative approach α and the normal contact force F_n as depicted in Figure 3.2.

$$\frac{\alpha}{\alpha_f} = \frac{3\left(\frac{F_n}{F_{nc}}\right)+2+2\left(1+\frac{F_n}{F_{nc}}\right)^{1/2}}{3^{2/3}\left[\frac{F_n}{F_{nc}}+2+2\left(1+\frac{F_n}{F_{nc}}\right)^{1/2}\right]^{1/3}} \tag{3.69}$$

in which

$$\alpha_f = \left(\frac{3F_{nc}^2}{16R^*E^{*2}}\right)^{1/3} \tag{3.70}$$

represents the (negative) relative approach at which the contact breaks which is point D in Figure 3.2.

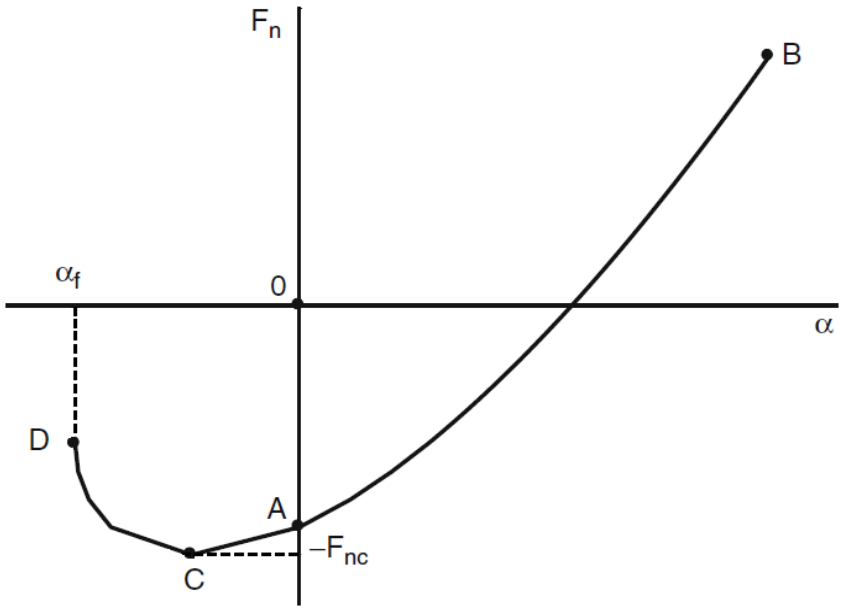

Figure 3. 2. JKR theory (normal force-displacement curve)

Initially, when two spheres come into contact ($\alpha = 0$) as a result of the van der Waals attractive forces the normal contact force F_n instantly drops down to point A, where the normal contact force equals $F_n = -8F_{nc}/9$. However, the normal contact force increases from point A to (say) point B during the compression or loading step. If the decompression (or unloading stage) follows, the response is elastic, and the force returns to point A from point B. In this case, the value of the relative approach is $\alpha = 0$, but a finite area of contact

remains. During the unloading process, when the normal contact force reaches point A, all the previous work undertaken will be recovered. However, the spheres remain together at point A; therefore, to break the contact, additional work is needed, during which the tensile force increases from point A to point C, and subsequently reduces until the contact breaks at point D, when $F_n = -5F_{nc}/9$ and $\alpha = -\alpha_f$.

Since cement bonds are less stretchable, they break brittely. Therefore, the bond breaks at point C, where $F_n = -F_{nc}$ and $\alpha = -\alpha_f/3^{2/3}$ in the adapted JKR model used/proposed in this research. The maximum tensile force needed to break the contact is at point C is:

$$F_{nc} = 1.5\pi\Gamma R^* \tag{3.71}$$

where Γ represents the work of adhesion, and $\Gamma = \gamma_1 + \gamma_2$ where γ_1 and γ_2 represent the surface energies of both solids, that is $\Gamma = 2\gamma$ and $1/R^*$ which is the relative curvature of the contact.

In the proposed 3D contact bond model, any new contacts are made, they are regarded as being elastic, and both the normal and tangential forces are obtained from equations (3.62) and (3.66) (will be calculated by Hertzian theory).

3.4Coupled CFD-DEM-IBM modelling

The existing CFD method embedded in CFD-DEM-IBM code was changed from compressible to incompressible viscous fluid solver since the CFD-DEM modelling of sand production is not a large-scale simulation that can capture the density changes caused by pressure or temperature changes as in real field conditions. The flow can be approximated as incompressible if flow-induced pressure changes do not cause significant density changes.

3.4.1 Fluid-particle interaction force

This study addresses large numbers of fine solid particles as well as the single-phase fluid. The total force F_i which acts on particle *i* assimilated into the CFD-DEM-IBM method has numerous components: f_{fpi} is the fluid-particle interaction force, f_{ci} is the sum of the solid particle-particle contact force and the particle-LSO contact force; also, a gravitational force $m_i g$ exists. The rotational and translational motions of each particle are governed by Newton's second law:

$$m_i \frac{dv_i}{dt} = F_i = f_{ci} + f_{fpi} + m_i g \tag{3.72}$$

$$I_i \frac{d\omega_i}{dt} = T_i \tag{3.73}$$

in which I_i ω_i and v_i are the momentum inertia, angular and linear velocities of the particle *i*, respectively. T_i represents the torque which emanates from the contact force tangential components. As Anderson and Jackson (1967) indicate, the fluid-particle interaction force, f_{fpi}, can be expressed as follows:

$$f_{fpi} = -v_{pi}\nabla p + v_{pi}\nabla \cdot \tau_f + \varepsilon f_{di} \tag{3.74}$$

where v_{pi} represents the volume of particles, p is the local fluid pressure, ε is the local void fraction, f_{di} represents the drag force, and τ_f is the local viscous stress tensor.

Di Felice (1994) presented an experiential correlation to compute the drag force f_{di} on particle *i*

$$f_{di} = \frac{1}{2} C_{Di} \rho_{fj} \frac{\pi d_{pi}^2}{4} \varepsilon_j^2 |u_{fj} - v_i| (u_{fj} - v_i \chi) \varepsilon^{-\chi} \tag{3.75}$$

in which ε_j, u_{fj} and ρ_{fj} indicate the void fraction, fluid velocity and density of the fluid cell j, in which particle i of diameter d_{pi} resides; also $\varepsilon^{-\chi}$ is a correction for the existence of other particles. This considers the variation of the exponent in the intermediate flow regime in addition to the near constant values in the high and low Reynolds number flow regimes:

$$\chi = 3.7 - .065\, exp\left[-\frac{(1.5 - log_{10} Re_{pi})^2}{2}\right] \tag{3.76}$$

For a single unhindered particle, C_{Di} represents the coefficient of fluid drag:

$$C_{Di} = \left[0.63 + \frac{4.8}{\sqrt{Re_{pi}}}\right]^2 \tag{3.77}$$

The particle Reynolds number Re_{pi}, on the basis of the superficial slip velocity between particle and fluid is:

$$Re_{pi} = \frac{\rho_f d_{pi} \varepsilon_j |u-v|}{\mu_s} \tag{3.78}$$

It is anticipated that the viscous stress tensor is exclusively dependent on the fluid motion (Bird et al., 1960).

$$\tau_f = \left[\left(\mu_b - \frac{2}{3}\mu_s\right)\nabla \cdot u_f\right]\delta + \mu_s\left[\left(\nabla u_f\right) + \left(\nabla u_f\right)^T\right] \tag{3.79}$$

in which μ_b and μ_s are the bulk and shear viscosities, and u_f is the velocity of the fluid, respectively. This study addresses incompressible flow; consequently, the fluid density ρ_f remains constant.

3.4.2 Particle-fluid interaction force

The continuity and momentum equations for the hydrodynamics of incompressible fluid in a granular system are as follows:

$$\frac{d(\rho_\mathrm{f}\varepsilon)}{dt} + \nabla \cdot \rho_\mathrm{f}(\varepsilon \mathrm{u_f}) = 0 \tag{3.80}$$

$$\frac{d(\rho_\mathrm{f}\varepsilon \mathrm{u_f})}{dt} + \nabla \cdot \rho_\mathrm{f}(\varepsilon_e \mathrm{u_f u_f}) = -\nabla p + \nabla \cdot \tau_\mathrm{f} - \mathrm{F_{fp}} + \varepsilon \rho_\mathrm{f} \mathrm{g} \tag{3.81}$$

where F_{fp} represents the interaction force between fluid and particle per unit bed volume which is obtained as:

$$\mathrm{F_{fp}} = \frac{1}{V_\mathrm{cell}}\sum_{i=1}^{n_\mathrm{c}} \mathrm{f_{fpi}} = -(1-\varepsilon)\nabla p + (1-\varepsilon)\nabla \cdot \tau_\mathrm{f} + \frac{1}{V_\mathrm{cell}}\sum_{i=1}^{n_\mathrm{c}} \varepsilon \mathrm{f_{fpi}} \tag{3.82}$$

in which n_c is the number of particles in a fluid cell of volume V_{cell}. We can express the momentum equation by substituting Equation 3.82 with Equation 3.81.

$$\frac{d(\rho_f \varepsilon u_f)}{dt} + \nabla \cdot (\rho_f \varepsilon_e u_f u_f) = -\varepsilon \nabla p + \varepsilon \nabla \cdot \tau_f - F_{fp}^* + \varepsilon \rho_f g \tag{3.83}$$

where F_{fp}^* is expressed as

$$F_{fp}^* = \frac{1}{V_{cell}} \sum_{i=1}^{n_c} \varepsilon f_{fpi} \tag{3.84}$$

3.4.3 Particle-fluid Interaction force with the IBM

In order to simulate arbitrarily complicated geometry with mobile and sophisticated boundaries, Peskin (1972) presented the IBM method. Although this is not compatible with the CFD-DEM Eulerian rectangular grids. Further, to model gas-particle two-phase flows with moving and complicated boundaries Guo et al. (2013) assimilated the IBM technique into a current CFD-DEM code. These are based on the previous IBM development for modelling of particulate systems comprising solid and gas particles as suggested by Kajishima et al. (2001). This technique is applied when the multiphase method concerns a fluid, at least one Large Solid Object (LSO) (or complex wall boundaries), numerous fine solid particles, as well as the dynamic interactions among them.

We can express the volume of a single fluid cell V_{cell}, as the sum of the volume of the fine particles, V_p, the volume of the fluid in this cell, V_f and the volume of the LSO, V_{obj}

$$V_{cell} = V_p + V_{obj} + V_f \tag{3.85}$$

Furthermore, we can define the volume fraction of the fluid cell, excluding the fine particles, as the effective void fraction:

$$\varepsilon_e = 1 - \frac{V_p}{V_{cell}} = \frac{V_{obj} + V_f}{V_{cell}} \tag{3.86}$$

and the volume fraction of the LSO in a fluid cell can be defined as:

$$\alpha = \frac{V_{obj}}{V_{cell}} \tag{3.87}$$

In order to evaluate the value of α at the collocation point for each cell, Yuki et al (2007) suggested a basic algorithm:

$$\alpha = 0.5\left[1 - tanh\left(\frac{\Delta}{\sigma\lambda d_{cell}}\right)\right] \tag{3.88}$$

$$\lambda = |n_x| + |n_y| + |n_z| \tag{3.89}$$

$$\sigma = 0.05(1 - \lambda^2) + 0.3 \tag{3.90}$$

where and σ indicates a signed distance from the cell centre to the surface element, $n = (n_x, n_y, n_z)$ is a normal outward unit vector at a surface element, and d_{cell} is represents the cell size.

Furthermore, Kajishima et al. (2001) determined a unified velocity, u, in order to describe the fluid-LSO technique by volume averaging the local fluid velocity, u_f, and the local solid object velocity, U_{obj}, for each fluid cell:

$$u = \frac{V_f}{V_{obj}+V_f}u_f + \frac{V_{obj}}{V_{obj}+V_f}U_{obj} = \frac{\varepsilon_e - \alpha}{\varepsilon_e}u_f + \frac{\alpha}{\varepsilon_e}U_{obj} \tag{3.91}$$

in which the local LSO velocity, U_{obj}, is calculated from the average of the local velocities at solid points over the volume of the LSO falling in a fluid cell, V_{obj}:

$$\mathrm{U_{obj}} = \frac{1}{V_{\mathrm{obj}}}\int_{V_{\mathrm{obj}}}(\mathrm{v_{LSO}} + \omega_{\mathrm{LSO}} + r)dV = \mathrm{v_{LSO}} + \frac{1}{V_{\mathrm{obj}}}\int_{V_{\mathrm{obj}}}\omega_{\mathrm{LSO}} + rdV \tag{3.92}$$

where ω_{LSO} and v_{LSO} are the rotational and translational velocities of the LSO, with r being the relative position from the centre of the object mass to a local point on the object.

The momentum and continuity equations for the hydrodynamics of incompressible fluid in the presence of the LSO and in a granular system are based on the governed equations for compressible flow by Guo et al. (2012):

$$\frac{d(\varepsilon_e)}{dt} + \nabla\cdot(\varepsilon_e u) = 0 \tag{3.93}$$

$$\rho_f\frac{d(\varepsilon_e u)}{dt} + \rho_f\,\nabla\cdot(\varepsilon_e uu) = -\varepsilon_e\nabla p + \varepsilon_e\nabla\cdot\tau - F_{fp}^{*} + \rho_f\varepsilon_e g + f' \tag{3.94}$$

in which the fluid-LSO is regarded as being a single continuum having a unified velocity field, u. This is because the impermeable and no-slip and conditions at fluid-solid interface with $u_f = U_{obj}$ were considered. Furthermore, the expression, f' is the virtual body force used to correct the velocity field, u, at the fluid-solid interface and within the LSO. The viscous stress tensor τ, subsequently provided by Equation 3.75, is used with u replacing u_f. Moreover, the effective void fraction, ε_e, is applied in both governing equations in order to consider the impact of the presence of fine particles. Nevertheless, the real void fraction is applied in equations 3.75 and 3.82 in order to compute the drag force f_{di} and the fluid-particle interaction force F_{fp}^*, respectively, and is obtained from:

$$\varepsilon = 1 - \frac{V_p}{V_{cell} - V_{obj}} = \frac{\varepsilon_e - \alpha}{1 - \alpha} \tag{3.95}$$

Furthermore, the momentum Equation 3.94 is discretised in time by using the first-order finite difference algorithm:

$$\rho_f(\varepsilon_e u)^{n+1} = \rho_f(\varepsilon_e u)^n + \Delta t \cdot H^n - \Delta t \cdot (\varepsilon_e \nabla p)^{n+1} + \Delta t \cdot (f')^{n+1} \tag{3.96}$$

in which

$$H = -\nabla \cdot \rho_f(\varepsilon_e u u) + \varepsilon_e \nabla \cdot \tau_f - F_{fp}^* + \rho_f \varepsilon_e g \tag{3.97}$$

and Δt which represents the time step and superscripts implies the number of the time step.

The three principal variables α, u and f' of the computational cells, based on the LSO location, will differ:

1. If the computational cells are outside the LSO, $\alpha = 0$, $u = u_f$ and no virtual force exists, $(f')^{n+1}$=0; consequently, the momentum Equation 3.94 reduces to Equation 3.83.
2. If the computational cells are inside the LSO, the momentum Equation 3.94 is used with $\alpha = 1$, ${u^{n+1}} = {U_{obj}}^{n+1}$, the virtual body force, $(f')^{n+1}$, may be obtained from Equation.3.96:

$$(f')^{n+1} = \frac{\rho_f \left(\varepsilon_e U_{obj}\right)^{n+1} - \rho_f(\varepsilon_e u)^n}{\Delta t} - H^n + (\varepsilon_e \nabla p)^{n+1} \tag{3.98}$$

3. If the computational cells are at the fluid-solid interface which are partly occupied by the LSO, the momentum Equation.3.94 is used with $0 < \alpha < 1$, $u^{n+1} = {U_{obj}}^{n+1}$, and the virtual body force, $(f')^{n+1}$, may be defined by a first-order linear interpolation using α as defined in equations 3.88 to 3.90:

$$(f')^{n+1} = \alpha \left[\frac{\rho_f \left(\varepsilon_e U_{obj}\right)^{n+1} - \rho_f (\varepsilon_e u)^n}{\Delta t} - H^n + (\varepsilon_e \nabla p)^{n+1} \right] \tag{3.99}$$

3.4.4 Numerical Algorithms

The previous algorithm (Guo et al., 2012) is restated with adaptations for incompressible flow case for the reader's convenience.

1. Calculate the new velocities and new positions from equations 3.72 and 3.73.
2. Calculate the new position of LSO and the new velocity.
3. Calculate ε_e, α and ε for each cell.
4. Calculate the virtual body force.
5. We calculate p' according to the pressure-correction technique. Firstly, we calculate u^{n+1} from the continuity system (Eq. 3.100). Secondly, we calculate u^* from Equation 3.104 with the provided p^*. Subsequently, we obtain p' rom Equation 3.105.
6. We can obtain the piecewise constant in cell pressure at $(n+1)^{th}$ by applying $p^{n+1} = p^* + p'$.
7. Update $(f')^{n+1}$ and u^{n+1} by using p^{n+1}.
8. If there is difficulty in testing the convergence of continuity, we repeat the process from the fourth stage by using $p^* := p^{n+1}$. This iteration persists until the convergence requirement is attained.
9. We estimate u_f^{n+1} from Equation 3.91.

3.4.5 Pressure-correction Equations

We applied a semi-implicit finite difference numerical method by using a staggered grid to resolve the incompressible Navier-Stokes equations on an equidistant 3D Cartesian grid. Furthermore, we used the adapted PISO (Issa, 1986) version (Pressure-Implicit with Splitting of Operators) of the SIMPLE methodology (Semi-Implicit Method for Pressure-Linked Equations), as suggested by Patanker (1980), as an algorithm. At the centre of each fluid cell the porosity and pressure scalar variables are determined, and at the cell faces the velocity components are determined. (Figure 3.3).

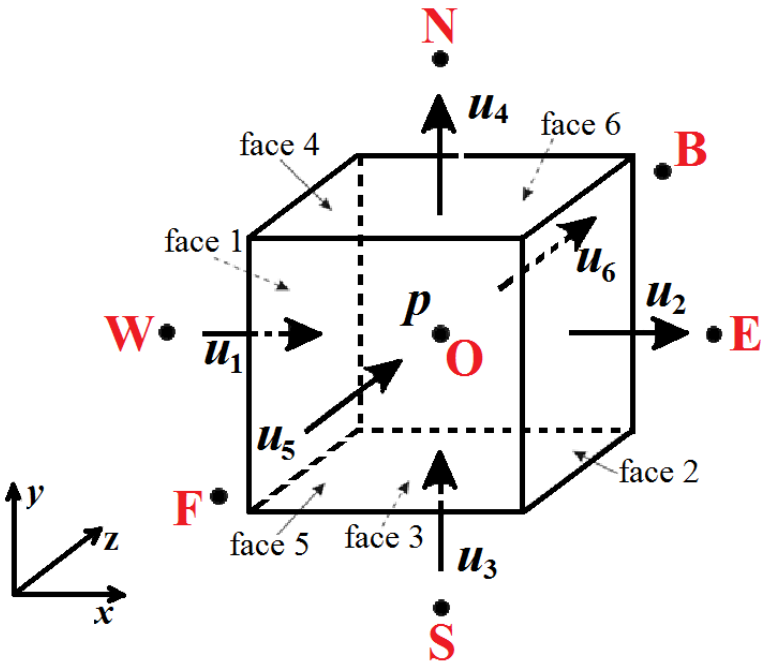

Figure 3. 3. 3D CFD cell

For the cell centre O, the continuity equation (3.93) is discretised as:

$$(\varepsilon_e)_0^{n+1} - (\varepsilon_e)_0^n + \frac{\Delta t}{\Delta x}[(\varepsilon_e u)_2^{n+1} - (\varepsilon_e u)_1^{n+1}] + \frac{\Delta t}{\Delta y}\ [(\varepsilon_e u)_4^{n+1} - (\varepsilon_e u)_3^{n+1}]$$

$$+\frac{\Delta t}{\Delta z}[(\varepsilon_e u)_6^{n+1} - (\varepsilon_e u)_5^{n+1}] = 0 \qquad (3.100)$$

The discretised momentum equation with virtual force is:

$$\rho_f(\varepsilon_e u)^{n+1} = (1-\alpha)\rho_f(\varepsilon_e u)^n + (1-\alpha)\Delta t H^n - (1-\alpha)\Delta t(\varepsilon_e \nabla p)^{n+1} + \alpha\rho_f\left(\varepsilon_e U_{obj}\right)^{n+1} \quad (3.101)$$

The momentum equation at n+1 at 1- 6 faces is:

$$\rho_f(\varepsilon_e u)_1^{n+1} = (1-\alpha_1)\rho_f(\varepsilon_e u)_1^n + (1-\alpha_1)\Delta t(H_x)_1^n - (1-\alpha_1)\frac{\Delta t}{\Delta x}(\varepsilon_e)_1^{n+1}(P_O^{n+1} - P_w^{n+1}) + \alpha\rho_f\left(\varepsilon_e U_{obj}^x\right)_1^{n+1} \quad (3.102.1)$$

$$\rho_f(\varepsilon_e u)_2^{n+1} = (1-\alpha_2)\rho_f(\varepsilon_e u)_2^n + (1-\alpha_2)\Delta t(H_x)_2^n - (1-\alpha_2)\frac{\Delta t}{\Delta x}(\varepsilon_e)_2^{n+1}(P_E^{n+1} - P_O^{n+1}) + \alpha\rho_f\left(\varepsilon_e U_{obj}^x\right)_2^{n+1} \quad (3.102.2)$$

$$\rho_f(\varepsilon_e u)_3^{n+1} = (1-\alpha_3)\rho_f(\varepsilon_e u)_3^n + (1-\alpha_3)\Delta t(H_y)_3^n - (1-\alpha_3)\frac{\Delta t}{\Delta y}(\varepsilon_e)_3^{n+1}(P_O^{n+1} - P_S^{n+1}) + \alpha\rho_f\left(\varepsilon_e U_{obj}^y\right)_3^{n+1} \quad (3.102.3)$$

$$\rho_f(\varepsilon_e u)_4^{n+1} = (1-\alpha_4)\rho_f(\varepsilon_e u)_4^n + (1-\alpha_4)\Delta t(H_y)_4^n - (1-\alpha_4)\frac{\Delta t}{\Delta y}(\varepsilon_e)_4^{n+1}(P_N^{n+1} - P_O^{n+1}) + \alpha\rho_f\left(\varepsilon_e U_{obj}^y\right)_4^{n+1} \quad (3.102.4)$$

$$\rho_f(\varepsilon_e u)_5^{n+1} = (1-\alpha_1)\rho_f(\varepsilon_e u)_1^n + (1-\alpha_1)\Delta t(H_z)_1^n - (1-\alpha_1)\frac{\Delta t}{\Delta z}(\varepsilon_e)_5^{n+1}(P_O^{n+1} - P_B^{n+1}) + \alpha\rho_f\left(\varepsilon_e U_{obj}^z\right)_5^{n+1} \quad (3.102.5)$$

$$\rho_f(\varepsilon_e u)_6^{n+1} = (1-\alpha_6)\rho_f(\varepsilon_e u)_6^n + (1-\alpha_6)\Delta t(H_z)_6^n - (1-\alpha_6)\frac{\Delta t}{\Delta z}(\varepsilon_e)_6^{n+1}(P_F^{n+1} - P_O^{n+1}) + \alpha\rho_f\left(\varepsilon_e U_{obj}^z\right)_6^{n+1} \quad (3.102.6)$$

The pressure at $(n+1)^{th}$ time step, in this technique, may be calculated as a sum of the predicted, p^*, and the corrected p':

$$p^{n+1} = p^* + p' \quad (3.103)$$

Moreover, we calculated the predicted mass flow field, $\rho_f \varepsilon_e u$, by the predicted pressure field p^* (the momentum equation at p^* at 1- 6 faces):

$$\rho_f(\varepsilon_e u)_1^* = (1-\alpha_1)\rho_f(\varepsilon_e u)_1^n + (1-\alpha_1)\Delta t(H_x)_1^n - (1-\alpha_1)\frac{\Delta t}{\Delta x}(\varepsilon_e)_1^{n+1}(P_O^* - P_w^*) + \alpha\rho_f\left(\varepsilon_e U_{obj}^x\right)_1^{n+1} \quad (3.104.1)$$

$$\rho_f(\varepsilon_e u)_2^* = (1-\alpha_2)\rho_f(\varepsilon_e u)_2^n + (1-\alpha_2)\Delta t(H_x)_2^n - (1-\alpha_2)\frac{\Delta t}{\Delta x}(\varepsilon_e)_2^{n+1}(P_E^* - P_O^*) + \alpha\rho_f\left(\varepsilon_e U_{obj}^x\right)_2^{n+1} \quad (3.104.2)$$

$$\rho_f(\varepsilon_e u)_3^* = (1-\alpha_3)\rho_f(\varepsilon_e u)_3^n + (1-\alpha_3)\Delta t(H_y)_3^n - (1-\alpha_3)\frac{\Delta t}{\Delta y}(\varepsilon_e)_3^{n+1}(P_O^* - P_S^*) + \alpha\rho_f\left(\varepsilon_e U_{obj}^y\right)_3^{n+1} \quad (3.104.3)$$

$$\rho_f(\varepsilon_e u)_4^* = (1-\alpha_4)\rho_f(\varepsilon_e u)_4^n + (1-\alpha_4)\Delta t(H_y)_4^n - (1-\alpha_4)\frac{\Delta t}{\Delta y}(\varepsilon_e)_4^{n+1}(P_N^* - P_O^*) + \alpha\rho_f\left(\varepsilon_e U_{obj}^y\right)_4^{n+1} \quad (3.104.4)$$

$$\rho_f(\varepsilon_e u)_5^* = (1-\alpha_5)\rho_f(\varepsilon_e u)_5^n + (1-\alpha_5)\Delta t(H_z)_5^n - (1-\alpha_5)\frac{\Delta t}{\Delta z}(\varepsilon_e)_5^{n+1}(P_O^* - P_B^*) + \alpha\rho_f\left(\varepsilon_e U_{obj}^z\right)_5^{n+1} \quad (3.104.5)$$

$$\rho_f(\varepsilon_e u)_6^* = (1-\alpha_6)\rho_f(\varepsilon_e u)_6^n + (1-\alpha_6)\Delta t(H_z)_6^n - (1-\alpha_6)\frac{\Delta t}{\Delta z}(\varepsilon_e)_6^{n+1}(P_F^* - P_O^*) + \alpha\rho_f\left(\varepsilon_e U_{obj}^z\right)_6^{n+1} \quad (3.104.6)$$

The momentum equation at n+1 as functions of momentum at $*$ and p' (after 3.104 - 3.102 equations for all faces):

$$\rho_f(\varepsilon_e u)_1^{n+1} = \rho_f(\varepsilon_e u)_1^* - (1-\alpha_1)\frac{\Delta t}{\Delta x}(\varepsilon_e)_1^{n+1}(P_O' - P_W') \quad (3.105.1)$$

$$\rho_f(\varepsilon_e u)_2^{n+1} = \rho_f(\varepsilon_e u)_2^* - (1-\alpha_2)\frac{\Delta t}{\Delta x}(\varepsilon_e)_2^{n+1}(P_E' - P_O') \quad (3.105.2)$$

$$\rho_f(\varepsilon_e u)_3^{n+1} = \rho_f(\varepsilon_e u)_3^* - (1-\alpha_3)\frac{\Delta t}{\Delta y}(\varepsilon_e)_3^{n+1}(P_O' - P_S') \quad (3.105.3)$$

$$\rho_f(\varepsilon_e u)_4^{n+1} = \rho_f(\varepsilon_e u)_4^* - (1-\alpha_4)\frac{\Delta t}{\Delta y}(\varepsilon_e)_4^{n+1}(P_N' - P_O') \quad (3.105.4)$$

$$\rho_f(\varepsilon_e u)_5^{n+1} = \rho_f(\varepsilon_e u)_5^* - (1-\alpha_5)\frac{\Delta t}{\Delta z}(\varepsilon_e)_5^{n+1}(P_O' - P_B') \quad (3.105.5)$$

$$\rho_f(\varepsilon_e u)_6^{n+1} = \rho_f(\varepsilon_e u)_6^* - (1-\alpha_6)\frac{\Delta t}{\Delta z}(\varepsilon_e)_6^{n+1}(P'_F - P'_O) \tag{3.105.6}$$

The pressure-correction equation for the cell O may be obtained by substituting Equations 3.105 with Equation 3.100 and rearranging the equation:

$$a_O p'_O + a'_W p'_W + a'_E p'_E + a'_S p'_S + a'_N p'_N + a'_B p'_B + a'_F p'_F = b \tag{3.106}$$

where

$$a'_W = (1-\alpha_1)\left(\frac{\Delta t}{\Delta x}\right)^2 (\varepsilon_e)_1^{n+1} \tag{3.107}$$

$$a'_E = (1-\alpha_2)\left(\frac{\Delta t}{\Delta x}\right)^2 (\varepsilon_e)_2^{n+1} \tag{3.108}$$

$$a'_S = (1-\alpha_3)\left(\frac{\Delta t}{\Delta y}\right)^2 (\varepsilon_e)_3^{n+1} \tag{3.109}$$

$$a'_N = (1-\alpha_4)\left(\frac{\Delta t}{\Delta y}\right)^2 (\varepsilon_e)_4^{n+1} \tag{3.110}$$

$$a'_S = (1-\alpha_5)\left(\frac{\Delta t}{\Delta z}\right)^2 (\varepsilon_e)_5^{n+1} \tag{3.111}$$

$$a'_N = (1-\alpha_6)\left(\frac{\Delta t}{\Delta z}\right)^2 (\varepsilon_e)_6^{n+1} \tag{3.112}$$

$$a_O = -(a'_W + a'_E + a'_S + a'_N + a'_B + a'_F) \tag{3.113}$$

and

$$b = \rho_f(\varepsilon_e)_0^{n+1} - \rho_f(\varepsilon_e)_0^n + \frac{\Delta t}{\Delta x}\left[\rho_f(\varepsilon_e u)_2^* - \rho_f(\varepsilon_e u)_1^*\right] + \frac{\Delta t}{\Delta y}\left[\rho_f(\varepsilon_e u)_4^* - \rho_f(\varepsilon_e u)_3^*\right] + \frac{\Delta t}{\Delta z}\left[\rho_f(\varepsilon_e u)_6^* - \rho_f(\varepsilon_e u)_5^*\right] \tag{3.114}$$

3.5 Numerical solutions

3.5.1 Numerical solution of DEM model

In order to incrementally compute the contact forces and positions of the particles, an explicit finite-difference scheme is utilised. For each time step Δt, the Newton's second law of motion is used to calculate the rotational and translational accelerations of each particle.

These values are assumed to be constant over the small-time step and a numerical integration yield updated positions and velocities of each particle. The relative approach between the contacting particles is calculated using the positions of particles, and the incremental contact forces are calculated using the relative approach. By resolving the contact forces acting on each particle, out-of-balance forces are obtained from which new accelerations can be computed in the next time step. The out-of-balance forces at this stage include the local drag force and local buoyancy force.

A linked-list scheme is used for contact detection. The workspace is divided into several sub-cells or boxes for an efficient contact search scheme (the DEM box size should be less than twice the largest DEM sphere diameter) and each sphere is mapped into any box in which any part of the sphere locates. The addresses of all spheres that map into any box are thus available through a linked list for that box. A second mapping, which uses a circumscribing cube dimension of *2(R+TOL),* ensures that spheres which are near the boundaries of box are also mapped into those boxes, where *R* is a radius of sphere and *TOL* is a tolerance set for sphere mapping (for all simulations, 0 was set for tolerance). For any spheres in the contact scan, only spheres that are held in the linked list of each DEM box in which the sphere is mapped are examined for contact. After the link lists are identified, and the accumulated component of translational displacement increment exceeds a set value, the next sphere remapping and contact scan is triggered.

The main computational scheme which runs the simulation cycle (one time step) has shown in Figure 3.4 (adopted from Kafui et al., 2011). By calling subroutine *evalvpc*, a field of new void fraction is computed, which geometrically divides each sphere volume between the CFD cells that it occupies. Further, in the call to *motion*, the incremental motion of each sphere is calculated using calculated force information from the previous time step. *rebox* is

called to remap the particle, *search* for and *update* contacts involving the particle if the condition of trigger is met. The call to *motion* also computes the fluid-particle interaction forces acting on each sphere. During the generation stage, walls are mapped into DEM boxes as spheres do. Therefore, any contacts between wall and particle are also identified. *walmot* computes the wall's incremental displacement since it has a translational velocity, *reboxw* is called to the wall remapping, *search* for and *update* contacts involving the wall if the condition of trigger is met. Using the information of sphere and wall displacements obtained in *motion* and *walmot*, the incremental calculation of contact forces is computed in *hford* with calls to *nhertz* (with and without adhesion) for the normal interactions and *tmindlin* for the tangential interactions.

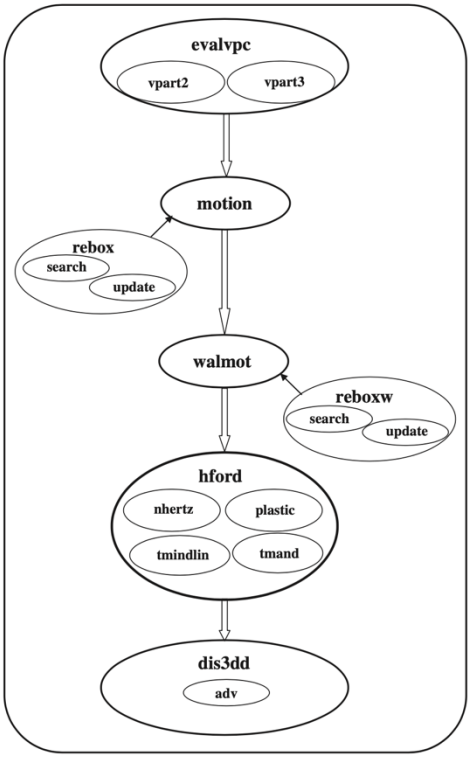

Figure 3. 4. The main computational sequence

The fluid state iterative evolution at the new time calculates by calling *dis3dd* (in the CFD part of code) which in turn calls *adv*. It uses fluid-particle interaction forces, particle velocities and void fraction field obtained from the DEM part of code. In the discretized momentum equation, the explicit terms are computed first, and then enters to implicit loop. In the implicit loop, a whole field pressure correction is iteratively applied. This iteration

continues until the mass residual (computed from the continuity equations) meets a prescribed convergence criterion for all interior computational fluid cells. A new fluid velocity field can then be calculated from the resulting fluid pressure field. Fluid computational cells of between 3 and 5 average particle diameters are generally used and these may or may not coincide with the box grid used in the DEM.

3.5.2 Numerical solution of hydrodynamic model

The numerical scheme used for the hydrodynamic model is well described in Kuipers et al. (1993). In order to the compressible Navier-Stokes equations on an equidistant 2D or 3D cartesian grid, a semi-implicit finite difference numerical technique employing a staggered grid is utilised. At the centre of each fluid cell the porosity and pressure scalar variables are determined, and at the cell faces the velocity components are determined. A difference between the 2D and 3D codes is the discretization of the convective momentum fluxes where a standard upwind scheme (first order accurate) is used in 2D, and the Barton scheme (second order accurate) is used in 3D. The algorithm is an adapted PISO (Issa, 1986) version of the SIMPLE methodology as suggested by Patanker (1980).

The numerical solution of the hydrodynamic model was developed through a series of computational cycles, each of which consisting of: 1) for all interior computational cells, explicit computations of all fluid velocity components; and 2) using an iterative procedure, implicit determination of porosity and pressure distributions. Mass residuals are calculated in accordance with the equation of fluid continuity (3.114) during the implicit computations.

The convergence criteria:

$$\boldsymbol{\rho_f(\varepsilon_e)_0^{n+1} - \rho_f(\varepsilon_e)_0^n + \frac{\Delta t}{\Delta x}\left[\rho_f(\varepsilon_e)_2^* - \rho_f(\varepsilon_e)_1^*\right] + \frac{\Delta t}{\Delta y}\left[\rho_f(\varepsilon_e)_4^* - \rho_f(\varepsilon_e)_3^*\right] + \frac{\Delta t}{\Delta z}\left[\rho_f(\varepsilon_e)_6^* - \rho_f(\varepsilon_e)_5^*\right] < eps \cdot \rho_f(\varepsilon_e)^{n+1}} \quad (3.115)$$

where, *eps* = 10^{-6} is a Relative error Newton iterates. A whole field pressure correction is applied in the case of the residual does not satisfy a prescribed convergence criterion for all interior computational fluid cells. New velocities calculated from the momentum equations, and new porosities are computed. The mass residuals are re-computed,

the convergence criterion checked, and process is repeated until an iteration limit is exceeded, or convergence is obtained.

For the hydrodynamic part of the code, the maximum allowable time step is limited by the viscosity stability criterion and the Courant condition. In general, the time step determined in the DEM part of the code has been found to be much smaller than the maximum determined using the CFL criterion proposed by MacCormarck (1971)

$$\Delta t = \left(\frac{|u|}{\Delta x} + \frac{|v|}{\Delta y} + \frac{|w|}{\Delta z} + c\sqrt{(\Delta x)^{-2} + (\Delta y)^{-2} + (\Delta z)^{-2}}\right)^{-1} \quad (3.116)$$

3.6 Boundary conditions

Each computational method incorporated in the CFD-DEM-IBM approach used in this study has several types of boundary conditions and the selection of its appropriate type for the given simulation geometry and design is very important since it can influence the simulation results.

3.6.1 DEM boundary conditions

Two types of boundary conditions are implemented in the current DEM modelling: rigid wall and periodic boundaries. In the current CFD-DEM-IBM code, the rigid wall boundaries have four types of wall: finite, infinite, cylindrical, and spherical. They are defined as elastic walls and particle-wall interactions forces calculated by Hertz (normal) and Mindlin (tangential) models. Translational movement of each type of walls is obtained by setting the appropriate wall velocities. During the wall movement, forces and displacement of walls are applied to the particle assembly through the wall-particles contacts. The spherical wall is also allowed to have a radial velocity which allows the wall to enlarge of shrink by changing its radius. A servo control mechanism is also introduced for walls, where the velocity of walls is continuously adjusted to minimize the difference between the calculated normal (finite and infinite) or radial (spherical and cylindrical) the force acting on the wall and required force.

Periodic cell/boundary is required to numerically study the material at micro and macro-scale constitutive behaviour and to mimic laboratory experiments (Thornton, 2000). It implies that the 'sample size' is infinite, there are no 'loading boundaries' and there is no finite size effect that may affect the results, material is represented by repeated, identical representative volume element. When using periodic boundaries, the evolution of the system can be achieved by setting a stress control mode and/or strain control mode. The strain control mode only works for assemblies with periodic boundaries and the deformation of the periodic cell can be controlled by specifying a uniform strain-rate tensor ε_{ij} for the assembly, where all the spheres in the cell moves and each of their incremental displacement is

$$\Delta x_i = \dot{\varepsilon_{ij}} x_j \Delta t \tag{3.117}$$

where $x_i (i = 1,2,3)$ is the coordinate component of the consistent particle and Δt is the small timestep used to simulate the evolution of the system. For an assembly with periodic boundaries, any particles which intersect one face of the unit cell have images that intersect the opposite face of the cell. Because of this, the particles intersecting the periodic boundaries of the unit cell are self-balancing. For an assembly without periodic boundaries, particles lying on the periphery of the assembly are not self-balanced and are free to move outwards. When a strain rate tensor is applied, the forces which built up between particles tend to cause the particles on the periphery to move outwards. As a result, one cannot deform the assembly in the desired way by using strain control if periodic boundaries are not applied.

Stress/servo control mode is required to follow the desired stress paths and its general forms are

$$\dot{\varepsilon} = g(\sigma^* - \sigma) \tag{3.118}$$

$$\dot{\varepsilon} = \dot{\varepsilon}^{t-\Delta t} + \dot{g}(\sigma^* - \sigma) \tag{3.119}$$

where σ is the calculated value, σ^* is the desired value of stress and g is a gain parameter and it is computed by trial and error.

Periodic boundaries have been used during the triaxial compression test simulations on cemented sandstone using 3D DEM approach (Figure 3.5), where the Equation (3.116) is used to bring the system to equilibrium at a desired stress state. In this study, this servo

control mode is used to perform an isotropic compression of the sample and the Equation (3.117) is used during the triaxial compression of the samples in order to adjust the strain-rate to minimise the difference between the desired and calculated stress states when following a desired stress path (see Chapter 4, Section 4.3.2).

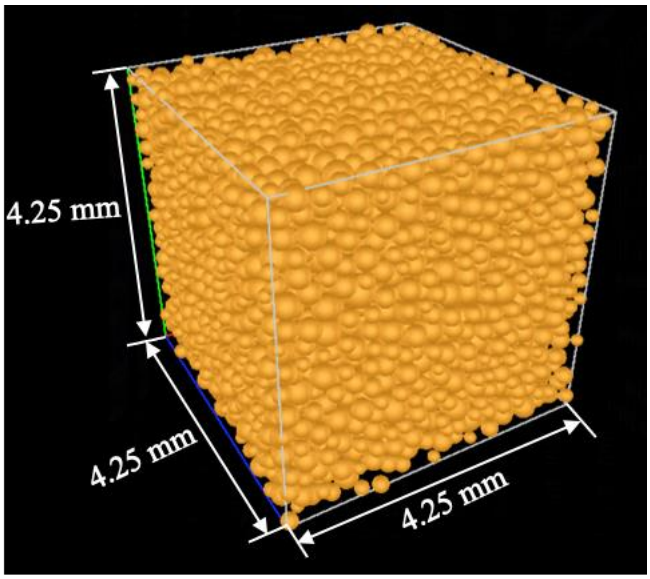

Figure 3. 5. Particle generation with six periodic boundaries

Hybrid boundary conditions are used during the 3D DEM simulations of CPT tests in cemented sandstone and 3D CFD-DEM-IBM simulations of sand production in oil wells. In the cone penetration simulations, initially all sides of sample were defined as periodic boundaries, then the rigid finite wall was set at the base of the specimen (Figure 3.6a) to eliminate the particle appearance from the top of the specimen during the pluvial deposition stage (see Chapter 5, Section 5.2.1). No servo control algorithms were used during the CPT tests, the top three finite wall boundaries (left, middle and right) were used to compress the bed (Figure 3.6b) and at the end of compression stage, the middle compressive wall was removed; two vertical walls and two inclined rigid moving finite wall boundaries (Figure 3.6c) were used as a cone and sides of penetrometer (Chapter 5, Section 5.2.2). At the end of CPT tests simulation, the penetrometer and the top middle compressive wall boundaries were removed, and the other boundary conditions remained during the sand production simulations.

For all walls, the following material attributes of iron were utilised: ρ = 7 900 kg/m^3 – density, ν = 0.29 – Poisson ratio, and E = 210 Gpa – Young's modulus.

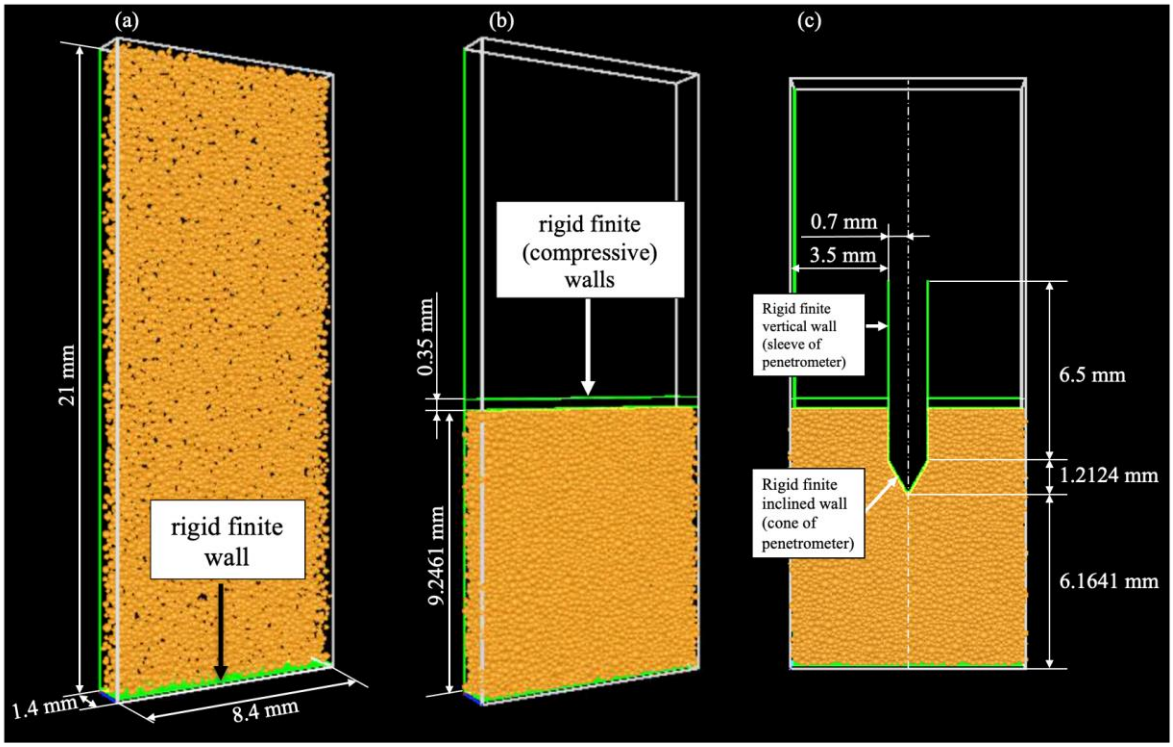

Figure 3. 6. DEM boundary conditions for CPT test (left and right, back and front, top sides are periodic): (a) deposition; (b) compression; (c) perforation

3.6.2 CFD boundary conditions

In the CFD method, boundary conditions are applied with fictitious cells surrounding the computational fluid cells' domain. In order to specify the boundary conditions to each CFD cell (see Figure 3.7), a flag matrix is utilized. There are 9 types of cell flags available in the DEM fluidised bed simulation code developed by Kafui et al. (2002) at Birmingham University.

For the sand production simulations, the following fluid boundary conditions were set for numerical samples: periodic boundary for left and right sides, impermeable free slip for back and front sides, and prescribed pressure for bottom and top sides.

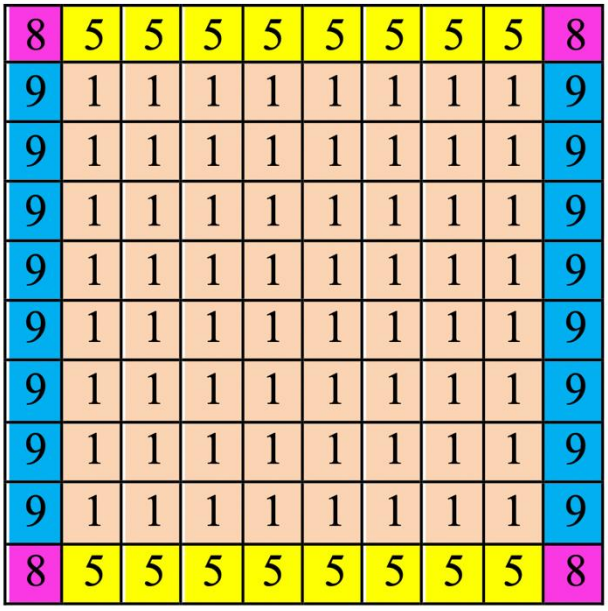

Figure 3. 7. CFD boundary conditions

3.6.3 IBM boundary conditions

In the IBM method integrated into the CFD-DEM approach by Guo et al. (2012) two types of boundaries exist: moving and complex. This method is necessary when dealing with moving and complex boundaries (arbitrarily complex geometries) that do not coincide with any fluid cell boundary. The main aim of this method is to introduce a virtual body force field such that a desired fluid velocity distribution can be imposed over a solid boundary. Consequently, the moving and complex geometries can be treated as immersed boundaries with the free slip and impermeable conditions.

At the beginning of sand production simulation, the IBM method was applied to the top two compressive rigid walls. The two top walls represent the perforated casing of the horizontal well and they are not necessarily located to coincide with any fluid cell boundary. Consequently, in order to treat them as immersed boundaries it was found necessary to attribute the two walls with a vertical thickness at least equal to the fluid cell dimension. As a result of this, the top and bottom boundaries of the ‘thick’ walls mapped into different fluid cells and each could be treated as immersed boundaries (with slip and impermeable conditions) using IBM method (Figure 3.8). The full developed model setup/design is fully described Chapter 6, Section 6.2.

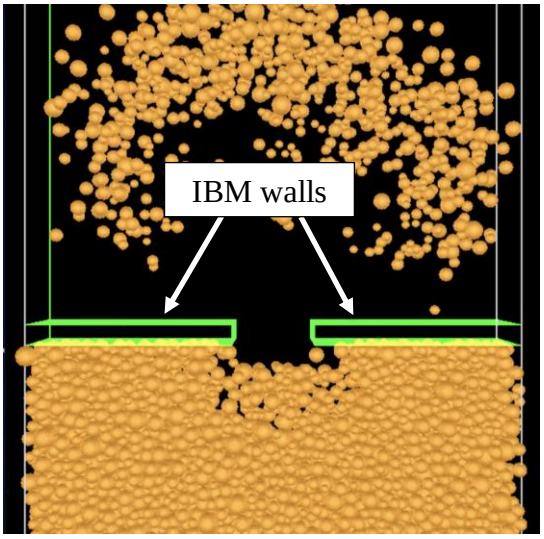

Figure 3. 8. IBM boundary conditions

3.7 Summary

Numerical predictions of sand production problem require the coupled modelling technique, which combinees at least DEM and CFD.

In this chapter, the coupling CFD-DEM-IBM model to simulate 3D sand production simulations is provided, and the equations which govern each computational technique (DEM, CFD and IBM) are given.

The DEM, which was introduced by Cundall and Strack in 1979, is a powerful tool to simulate the disintegration of granular media that is subjected to loading. Every granular media particle is regarded as being a separate entity having a geometric representation of its surface topology as well as a definition of its physical state. The interaction of the particles in the DEM is regarded as being as a dynamic procedure, with a state of equilibrium being attained when the forces and external forces are equal. We may obtain the displacements and the contact forces of a stressed assembly of particles by tracing the movement of each particle (Potyondy & Cundall, 2004).

In order to simulate a cemented sandstone material, a simple 3D contact bond model is provided and further used in all the simulations.

The existing CFD method embedded in the CFD-DEM-IBM code has been changed from compressible to incompressible viscous fluid solver since the CFD-DEM modelling of

sand production is not a large-scale simulation that can capture the density changes caused by pressure or temperature changes as in real field conditions. The flow can be approximated as incompressible if flow-induced pressure changes do not cause significant density changes.

The IBM technique is optimised in order to simulate the complicated interaction of the geometry associated with the well completion opening and the weakly cemented sandstone under the overburden pressure and drawdown.

Chapter 4 – Triaxial compression test simulations and validation

4.1 Introduction

The triaxial compression test is an extensively applied laboratory test to study the material behaviour. This enables the stiffness of soil and rock and the shear strength to be established for application in civil engineering, geotechnical design, and reservoir geomechanics. A triaxial test normally concerns restricting a cylindrical rock or/and soil sample to a pressurised cell to simulate a stress condition. The subsequent action is to shear to failure for the purpose of establishing the sample's shear strength attributes. The following may be inclusive of the primary parameters acquired from this test: the angle of shearing resistance ϕ', the strength of the material, the compression index C_c, the shear stiffness G, and the cohesion c'. Additionally, permeability k may be established.

The main aims of the numerical investigation of triaxial compression tests in this study are:

- To numerically study the material strength and failure, properties and behavior of the synthetic sandstone specimens equivalent to the Ustyurt-Buzachi Sedimentary Basin reservoir core samples.
- To build a DEM model which can capture the mechanical response of reservoir analogue sandstone should be used in the investigation of the mechanism that leads to sand production using DEM.
- To use as an application and validation of a developed simple 3D contact bond model for cemented sandstone.

Numerous researchers have, during the past four decades, conducted experimental triaxial tests of carbonate sands as well as artificial and natural sandstone (Clough et al., 1981; Leroueil & Vaughan, 1990; Lade & Overton, 1990; Airey, 1993; Coop & Atkinson, 1993; Huang & Airey, 1998; Cuccovillo & Coop, 1999; Coop & Willson, 2003; Schnaid et al., 2001; Wang & Leung, 2008a; Wang & Leung, 2008b; Collins & Sitar, 2011; Rios et al., 2014).

The Discrete Element Model (DEM) introduced by Cundall and Strack (1979) has been used to make a numerical study of bonded granular material during the past ten years. Wang and Leung (2008a) applied triaxial compression tests to numerically (2D) and experimentally investigate the material behaviour of cemented sand. Additionally, the stress-strain response of hydrate-bearing sand was numerically (3D) studied by Jung et al. (2012). A 2D contact model for bonded granular media, according to the Mohr-Coulomb failure criteria, was demonstrated by Utili and Nova (2008). Furthermore, a 3D bonded-particle model for cemented sand, where the spherical particles are linked by elastic beams has been suggested by Obermayr et al. (2013). Additionally, a 3D bonded contact model together with its application to grain-coating type methane hydrate-bearing sand and cemented sand was introduced by Shen et al. and Jiang (2016).

For the purpose of investigating the impact of bond strength on the micro and macro responses, this study's objective was to perform triaxial compression tests simulations of cemented sandstone on medium-dense, medium-loose, and loose specimens utilising the 3D DEM approach. The results drawn from the experiments of triaxial compression tests on the synthetic sandstone specimens equivalent to the Ustyurt-Buzachi Sedimentary Basin reservoir core samples, as studied by Shabdirova et al. (2016), were compared with the numerical results.

This Chapter 4 comprises five sections. Basic information concerning the synthetic sandstone specimens equivalent to the Ustyurt-Buzachi Sedimentary Basin reservoir core samples, as studied experimentally by Shabdirova et al. (2016), is given in Section 4.2. A detailed explanation of the triaxial compression tests simulations is provided in Section 4.3. In Section 4.4, a comparison of the experimental data and the numerical findings is given; and finally, Section 4.5 provides a summary of the chapter.

4.2 Reservoir analogue sandstone samples from the Ustyurt-Buzachi Sedimentary Basin

Information concerning the Ustyurt-Buzachi Sedimentary Basin synthetic sandstone specimens, which is obtained from Shabdirova et al. (2016), is included in this section, whereas the complete information may be found in the author's paper. It is important to be

aware that the cemented analogue samples that were studied experimentally are not the core samples of overburden formations. It is extremely rare for the core samples to be available for thorough laboratory testing (Zoback, 2017). Consequently, it is the opinion of Shabdirova et al. (2016) that the sand produced from the oil drawn from the wells is reservoir sand, which is utilised for the preparation of synthetic sandstone samples by firing sand-clay mixture.

The reservoir sandstone obtained from the Ustyurt-Buzachi Sedimentary Basin oilfield is restricted to the Barremian and Lower Cretaceous Hauterivian period formations, the reservoir being between 200 and 500 metres deep. In the Hauterivian age, the paleoclimate was humid and warm; however, during the Barremian era, sedimentation happened at the deltaic depositional environment, and subsequently, sea transgression occurred as well as deposition of shallow-marine sediments (Tashliyev & Tovbina, 1992). Such depositional and climatic conditions consequently caused the reservoir to be composed of fine-grained sandstone containing weak clay cement (Worden & Morad, 2003). Reservoir properties decrease as the clay content of the reservoir rock (which is between 10 and 35 percent) increases.

As a material for the experimental sandstone specimens the reservoir sand was used to replicate the reservoir sandstones in terms of the cement content, mineralogy, particle-size distribution, and porosity. Further, acetone and toluene were used to clean the sand from oil.

A Qicpic dynamic image analyser is used to evaluate the PSD data of the Ustyurt-Buzachi Sedimentary Basin synthetic sandstone specimens, as shown in Figure 4.1.

The X-Ray Diffraction (XRD) reservoir sand analysis indicates that the principal component of the sand is quartz, with a lesser amount of feldspar. Figure 4.2 (below) depicts a Scanning Electron Microscope (SEM) image of the reservoir sand fragment in which the larger particles are more elongated and angular, whereas the smaller ones are more spherical and rounded.

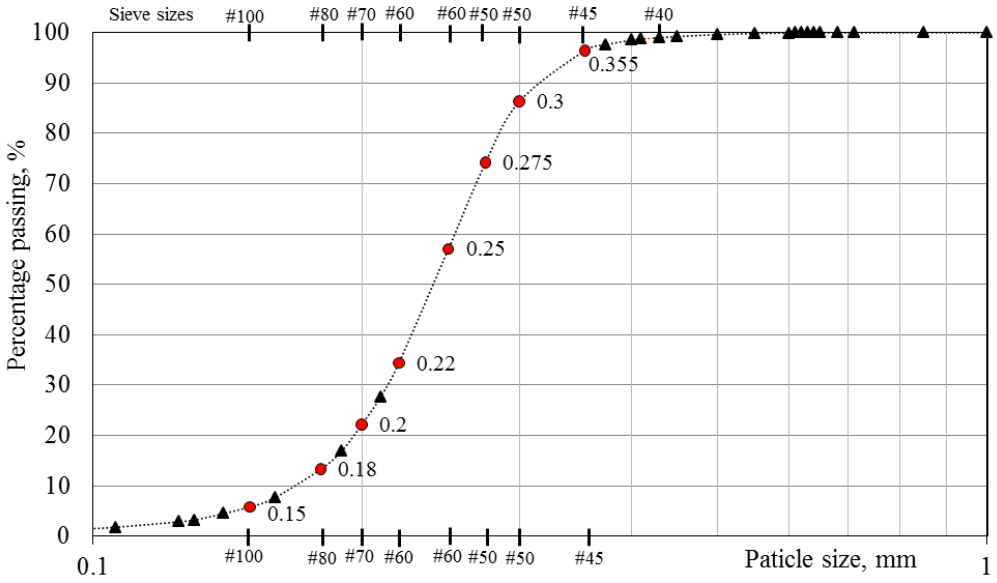

Figure 4. 1. The Ustyurt-Buzachi Sedimentary Basin's reservoir grain size distribution

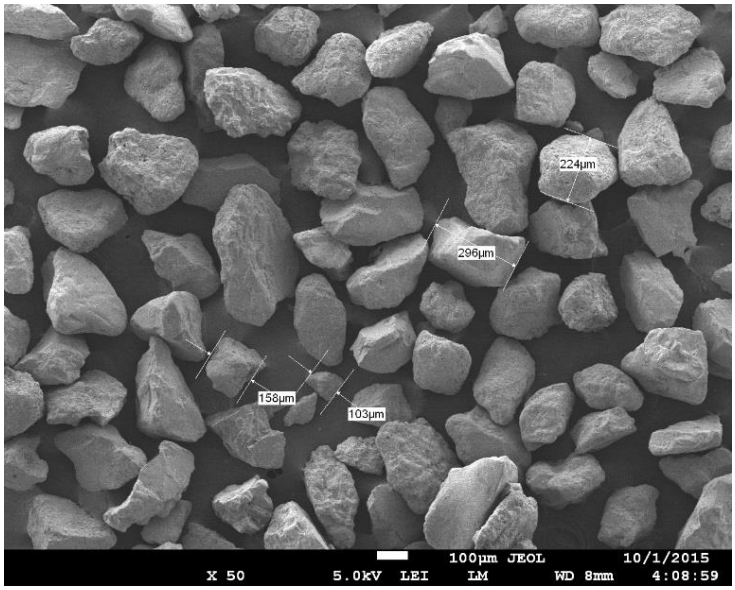

Figure 4. 2. SEM image of the reservoir sand

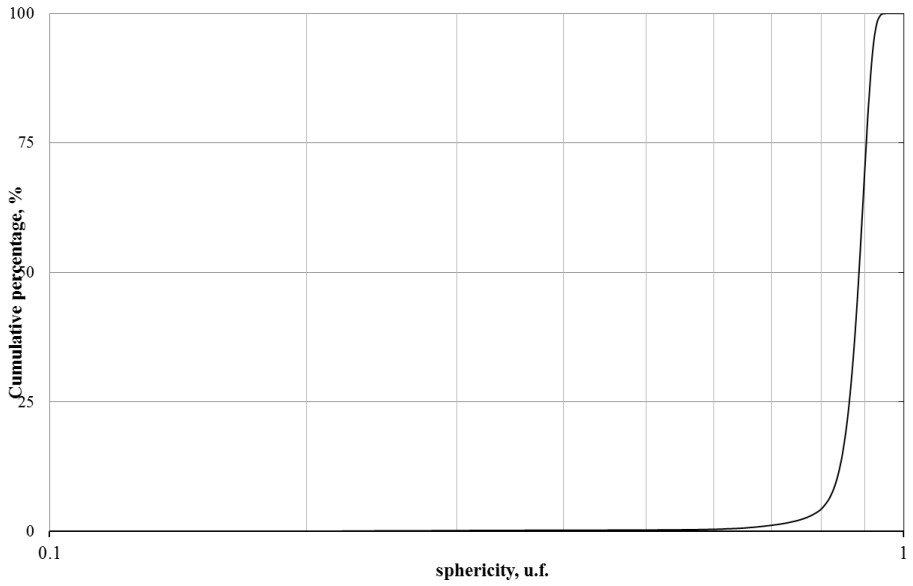

Figure 4. 3. Cumulative percentage of the sphericity values for the reservoir sand particles

Furthermore, the analysis of the particle shape has been studied in Qicpic, and the cumulative percentage of sphericity of particles is depicted in Figure 4.3. Sphericity measures the closeness of the particle shape to a sphere, whereas the software evaluates the particle projection area A and perimeter P from the particle image to calculate sphericity Φ (Cavaretta et al., 2009):

$$\Phi = \frac{2\sqrt{\pi A}}{P} \tag{4.1}$$

Greater values of the sphericity relate to more spherical shapes as it changes from 0 to 1. The analysis of the reservoir sand sample indicates that the sphericity Φ of 50 percent of the particles is greater than 0.88.

Further, the authors prepared the analogue sandstone samples using cementation method by firing sand-clay mixture. This method was first introduced by Maccarini et al. (1987), where specestone kaolin, quartz and crushed and fired kaolin (to represent weaker weathered feldspar in natural soils) were mixed with a ratio of 13:30:57, respectively. The authors reported that the clay cement bond strength depends on firing duration and temperature, and clay content; the cement bonding was form at 500^{o}C. This study was further extended by Hezmi et al. (2009) and Ali Rahman et al. (2010) by studying the effect of

temperature and bond structure of the samples at different temperatures and confining pressures, respectively.

Shabdirova et al. (2016) used the same sandstone preparation method conducted by abovementioned authors, but higher clay contents and different sand material were used. Elemental and microstructural analysis have been investigated on the specimens prepared at different temperatures with different clay content. The porosity of prepared samples was about 0.3 with different clay content of 20% and 30%, where white kaolin with a specific gravity of 2.61 was used as a clay. The reservoir sand had a specific gravity of 2.65.

The split moulds with a heigh of 76 mm and diameter of 38 mm were prepared, where their inner walls covered by thin plastic film. Dry kaolin and sand were mixed first, and then water was added. In order to achieve homogeneous substance, the wet mixture was stirred. The moulds were filled in several layers to form homogeneous specimens and then left for three days under room temperature. After 3 days the specimens were taken from the split mould and placed into the oven under different firing temperature and duration as shown in Table 4.1. The specimens fired for 5 hours at 200°C and 500°C indicated as *200* and *500*; with 20% and 30% of clay content indicated as *ls* and *hs*, respectively. Specimens fired for 8 hours at 200°C and 500°C indicated as 200/8 and 500/8. Loose and dense reservoir sands indicated as *lrs* and *drs*.

Table 4. 1. Information about reservoir sand and sandstone samples

Samples	Temperature, duration	Clay content, %	Void ratio	Porosity, %
lc200	200°C, 5 hours	20	0.492	33
lc200/8	200°C, 8 hours	20	0.472	32
lc500	500°C, 5 hours	20	0.549	35
hc200	200°C, 5 hours	30	0.433	30
hc200/8	200°C, 8 hours	30	0.455	31
hc500	500°C, 5 hours	30	0.521	34
lrs	-	-	0.79	44
drs	-	-	0.63	39

After the firing process, the total loss of weight was about 3% for specimens fired at 200°C, while for the specimens fired at 500°C it was 17%. The authors assumed that some components of the reservoir sand as undissolved oil were burnt off which was resulted in wight loss of 3%; and they didn't observe any kaolin dehydration process. The transformation of kaolin into metakaolin was observed for the specimens fired at 500°C, which was resulted in additional weight loss of 14%.

Further, all specimens were subjected to triaxial compression test compressed at 300 kPa of confining stress. Figures 4.4 and 4.5 shows the stress-strain and volume change data, respectively.

500°C cemented sandstone specimens reached the peak stress (1400 kPa) at lower axial strain of 5%; samples with low clay content show higher peak stress compared with high clay content specimen; specimens showed dilative behavior.

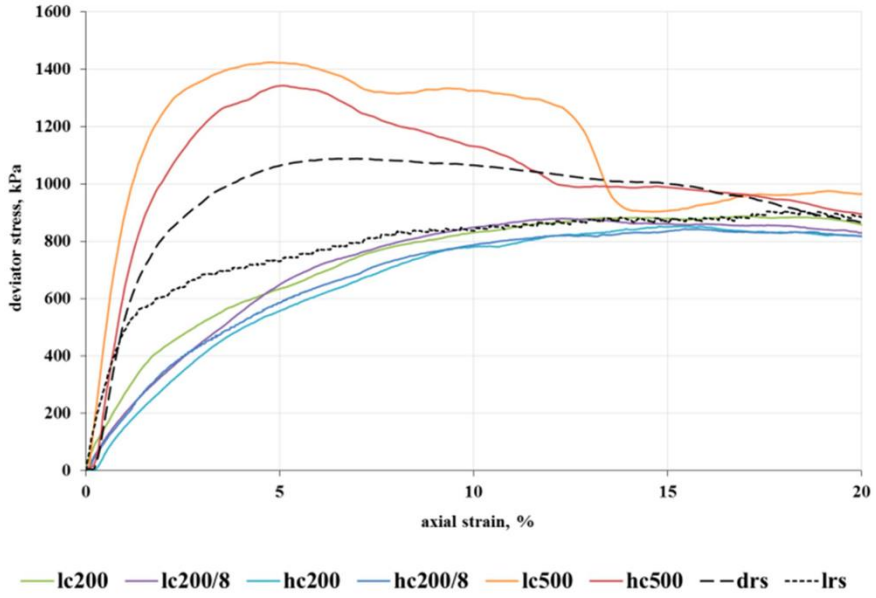

Figure 4. 4. Stress-strain curve

No peak stress was observed for 200°C cemented sandstone specimens. Besides of different duration of firing process and content of clay, the cemented specimens reached the maximum deviator stress (880 kPa) at axial strain of 12% and further sheared at constant stress and volume. During shearing, all 200°C specimens contracted. 500°C cemented sandstone specimens had higher strength compared with 200°C specimens due to formation of

metakaolin during firing. The difference in the maximum deviatoric stress was insignificant for the sandstone specimens with firing durations of 5 and 8 hours. The maximum deviatoric stress for cemented sandstone specimens with high clay content was 6% lower than for the sandstone specimens with low clay content.

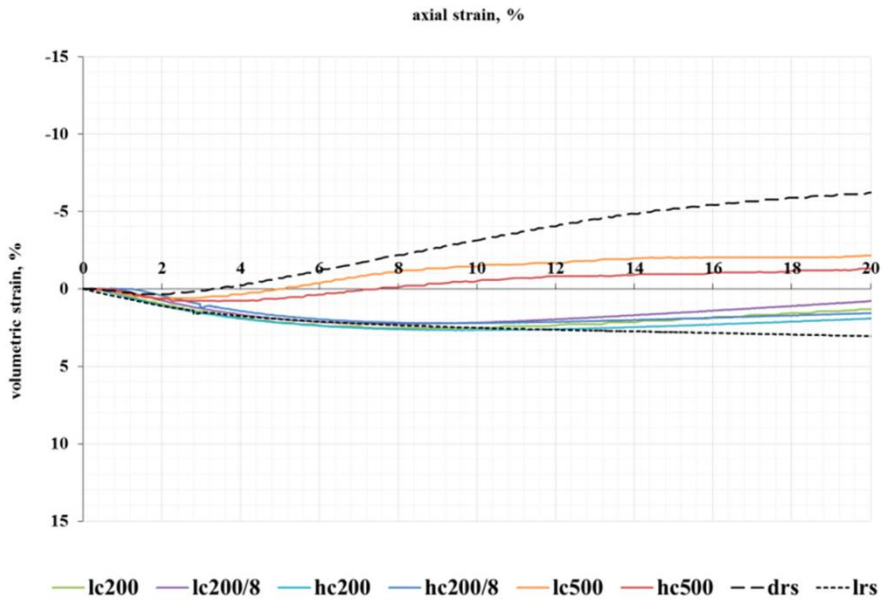

Figure 4. 5. Volume change curve

The authors concluded that no metakaolin was observed for specimens fired at 200°C, while transformation of kaolin into metakaolin was observed at 500°C; and metakaolin forms weak cement bonding; kaolin dehydration was associated with enhanced sandstone samples porosity. Shear strength of the cemented sandstone specimens depends on the clay content, mineralogy and particle size of sand.

4.3 Numerical simulations

Numerical simulations of triaxial compression have been undertaken by utilising 5206 particles at various values of bond strength and confining pressure. In this study, the spherical particles were not permitted to rotate for the purpose of acquiring acceptable values of shear strength (Calvetti and Nova, 2004). Since particularly low friction angles (φ') are

properties of assemblies of spherical particles, being unlike granular materials such as gravel and sand, the authors claim that inhibition compensates the impact of spherically shaped particles.

The objective of the present numerical simulation tests is to study the impact of bond strength, confining pressure and initial density on the cemented sandstone. Sixty simulations of triaxial compression tests on medium-dense, medium-loose and loose specimens were conducted across a scope of the following values of bond strengths (interface adhesion energy) of Γ = 0, 10, 20, 30 and 40 J/m^2, where Γ = 0 J/m^2 is an 'uncemented' sample and confining pressures: 100, 300, 500 and 1000 kPa. The fact that every simulation was conducted within a periodic cell suggests an infinite 'sample size'; however, the number of spheres in the periodic cell is a significant factor. The stress-strain curve's smoothness may be enhanced by increasing the number of particles. Since the acquired stress-strain curves are reasonably smooth, the number of particles used is acceptable. The simulations were categorised into the following three steps: particle generation, isotropic and triaxial compressions.

4.3.1 Particle generation

A selection was made of 8 various PSD of the Ustyurt-Buzachi Sedimentary Basin synthetic samples (see Figure 4.1 in Chapter 4). These were generated randomly as a granular gas in a cuboidal DEM box of the following dimensions of 4.25 mm: 0.355 mm (159), 0.3 mm (318), 0.275 mm (583), 0.25 mm (1027), 0.22 mm (811), 0.2 mm (783), 0.18 mm (911), and 0.15 mm (614). The following mechanical attributes were applied for all particles: ρ = 2605 kg/m^3 – experimental density of particle, E = 70 GPa – Young's modulus, and ν = 0.3 – Poisson's ratio. For the purpose of modelling quasi-static simulations within an acceptable timescale, the density of particle is increased by a factor of 10^{12}. According to Thornton (2000), the particle density scaling has no impact on displacements and forces; therefore, the accelerations and velocities are decreased according to magnitude; however, these are not relevant with regard to quasi-static behaviour. No gravity field is applied in the DEM simulations of triaxial compression test mentioned in this study.

According to Da Cruz et al. (2005), the inertial number *I* may be applied to indicate whether or not the simulations are quasi-static, thereby implying that $I < 1.10^{-3}$ ensures the

simulations to be quasi-static. Furthermore, the axial strain rate was 0.0001 for every simulation presented in the research. The average particle diameter was 0.24 mm, with the particle density being $2.605.10^{15}$ kg/m^3. The equation $I = \dot{\varepsilon} d_p \sqrt{\rho/p}$, calculates the inertial number to be 1.10^{-3} where p = 1000 kPa and 3.10^{-3} for p = 100 kPa. Therefore, it is possible to contend that the simulations are approximately quasi-static.

In the course of the particle generation stage, the interparticle friction coefficient was set to μ = 0.1; 0.2; and 0.3 for the purpose of acquiring the medium-dense, medium-loose and loose specimens, respectively.

4.3.2 Isotropic and triaxial compressions

The generated specimen was initially isotropically compressed to 10 kPa by the application of one million timesteps, thereby guaranteeing the void ratio, the mean stress and the number of contacts to be constant, having a mechanical coordination number $Z_m > 4$. When a stable system had been determined at 10 kPa, an additional isotropic compression was conducted until 80 kPa was reached, when the Hertz and Mindlin contact models were utilised to calculate every contact interaction. The mechanical coordination number at 10 kPa was $Z_m = 4.139$, whereas at 300 kPa, the number was $Z_m = 5.4$ for the medium-dense sample, $Z_m = 4.87$ for the medium-loose sample and Zm = 4.261 for the loose sample. Once the medium-dense and the medium-loose systems reached 80 kPa of isotropic compression, the interparticle friction coefficient was reset to $\mu = 0.3$. Subsequently, various values of bond strengths were initiated for the medium-dense, medium-loose and loose specimens. For all of the medium-dense, medium-loose and loose specimens, the number of bonds was initially 12225, 10345 and 7526 respectively. The modified JKR model was used to calculate the contact interactions in the course of the simulations of isotropic and triaxial compression tests. However, the model of Hertz was utilised for any subsequent new contacts that can be generated (Chapter 3, Section 3.3). The void ratios of the medium-dense, medium-loose and loose were equal to 0.617, 0.659 and 0.698 respectively at the beginning of the triaxial compression stage. In order to control the isotropic compression stage and also to maintain $\sigma_3 = \sigma_1$ to be constant in the shear stage, numerical servo-control algorithms were applied (Thornton, 2000).

At the end of the simulations, the periodic cell dimension towards the axial compression was 2.07 mm for p = 100 kPa; moreover, the corresponding dimension for p = 1000 kPa was 2.06. These two values approach nine times 0.24 mm which is the average particle diameter, indicating that the number of particles, being 5206, equates to a sufficient representative volume of material.

4.4 Numerical results

The deviator stress versus axial strain curves, which were acquired for simulations of triaxial compression test for both medium-dense and loose samples at a 300 kPa confining stress are depicted in Figure 4.6. The cemented sand stress-strain behaviour is shown by the results to depend resolutely on the bond strength; furthermore, it is initially stiff when compared to uncemented sand. As the bond strength increases, the initial stiffness and peak strength also increase, and the peak stress is reached at a lower axial strain in the case of a greater bond strength value. Figure 4.7 depicts the impact of bond strength on the volumetric strain. The material begins to expand at a lower axial strain in the case of a higher bond strength; moreover, as bond strength increases, the specimen shows a higher dilation rate. Furthermore, carbonate soils and both naturally and artificially cemented sands have been reported in experimental studies to display similar behaviour (Clough et al., 1981; Leroueil & Vaughan, 1990; Lade & Overton, 1990; Airey, 1993; Coop & Atkinson, 1993; Huang & Airey, 1998; Cuccovillo & Coop, 1999; Coop & Willson, 2003; Schnaid et al., 2001; Wang & Leung, 2008a; Wang & Leung, 2008b; Collins & Sitar, 2011; Rios et al., 2014). This has also been numerically captured by Wang & Leung (2008a); Obermayr et al. (2013); Jung et al. (2012); and Shen et al. (2016).

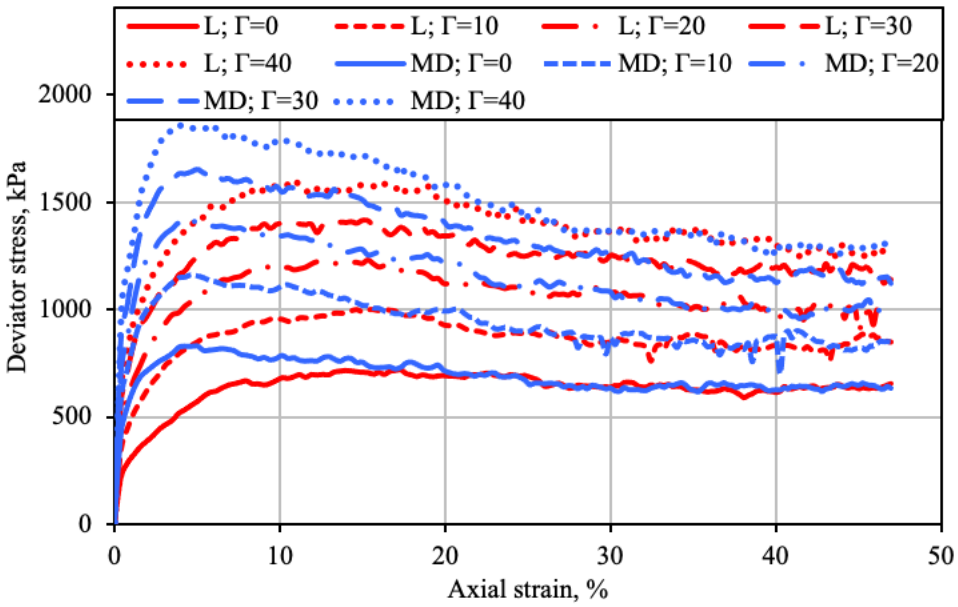

Figure 4. 6. The impact of bond strength on macromechanical response (deviator stress) of medium dense and loose samples compressed at 300 kPa

Figures 4.6 and 4.7 indicate that the mechanical response of cemented sands is dependent on initial density as well as on bond strength. Initial stiffness, peak strength and volumetric dilation increase as density increases (Clough et al., 1981; Huang & Airey, 1998; Rios et al., 2014); furthermore, it became apparent that as the initial density increases, the stress attains a peak at a lower axial strain. Although every numerical loose sample attained peak strength at approximately 15% axial strain, the peak strength was reached at below 5% axial strain in the case of medium-dense specimens. Additionally, the post-peak response of specimens also depends on the initial density and bond strength, for example, the medium-dense specimens demonstrate notable strain softening behaviour. Figure 4.6 illustrates that, subsequent to the peak, the deviator stress for various bond strength values slowly reduces, it does not converge with the curve for 'uncemented' ($\Gamma = 0$) sand. The reason for this is that the critical state strength is dependent on the bond strength magnitude, similarly to how it depends on the interparticle friction value. However, both the medium-dense, and the loose specimens attain the same critical state strength for a given value of Γ.

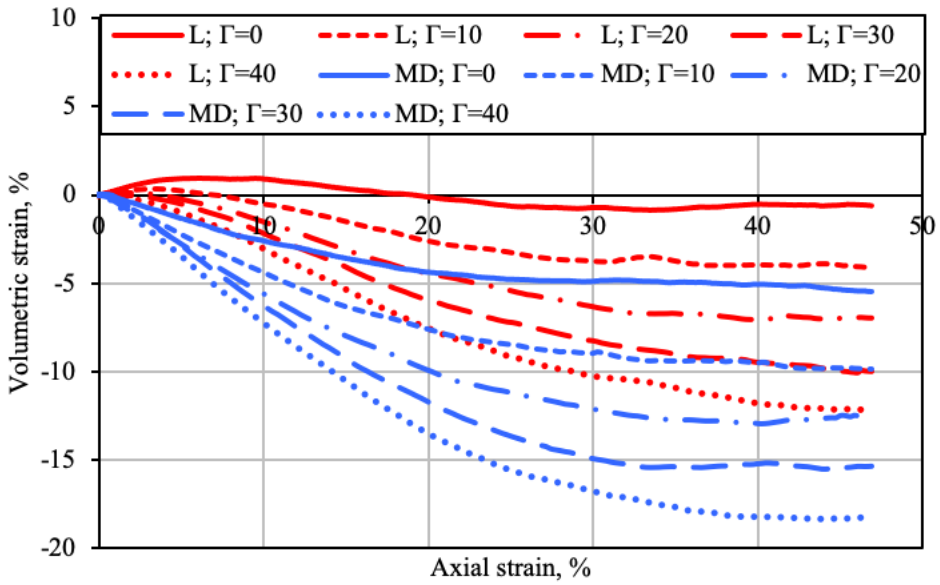

Figure 4. 7. The impact of bond strength on macromechanical response (volumetric strain) of medium dense and loose samples compressed at 300 kPa

The evolution of the number of bonds is shown in Figure 4.8, and that of the number of contacts in Figure 4.9. Furthermore, Figure 4.8 shows a reduction in the number of bonds at a decreasing rate, and also that in the case of lower bond strength, more bonds are broken. For example, at 30% axial strain all the bonded contacts broke, with a bond strength value Γ=10 J/m^2 for both medium-dense and loose samples, whereas some bonded contacts survived at a higher bond strength value of Γ=40 J/m^2. The fact that the total contacts number decreases as bond strength increases is depicted in Figure 4.9. Moreover, Figure 4.8 indicates an initial reduction in the number of contacts, when $\Gamma > 0$, which is caused by breaking bonds; subsequently, the increase of the number of bonded contacts and unbonded new ones is at a decreasing rate. Figures 4.6, 4.7, 4.8 and 4.9 indicate results that are qualitatively consistent with all data acquired from every test simulated at other confining stresses.

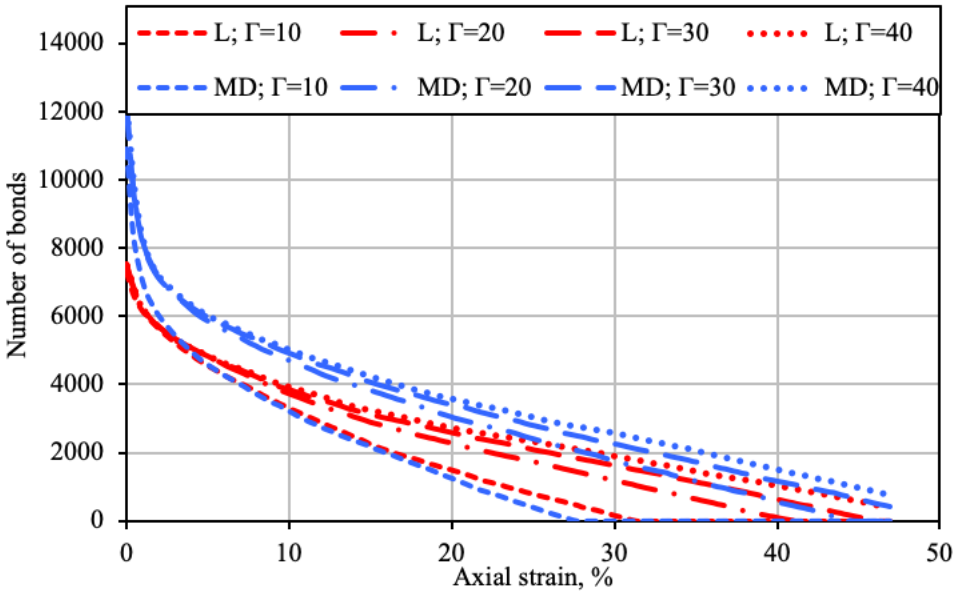

Figure 4. 8. The impact of bond strength on micromechanical response (number of bonds and contacts) of medium dense and loose samples compressed at 300 kPa

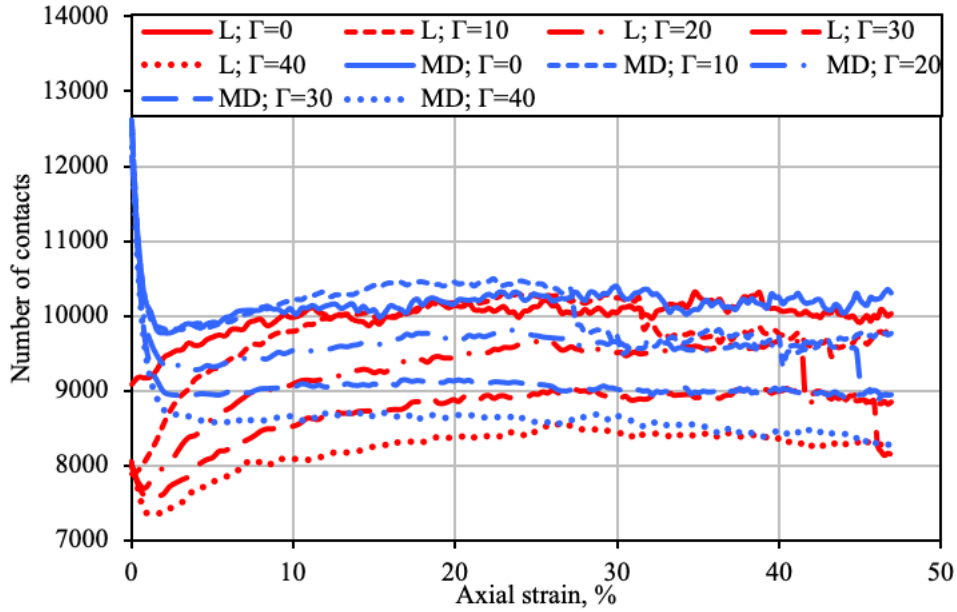

Figure 4. 9. The impact of bond strength on micromechanical response (number of contacts) of medium dense and loose samples compressed at 300 kPa

The impact of confining pressure on the evolution of the deviator stress and volumetric strain for medium-dense and loose specimens at a value of bond strength of Γ=20 J/m^2 is depicted in figures 4.10 and 4.11, respectively. The findings indicate that the stiffness and the peak strength both increase as the confining pressure increases (frictional response); and also that, at lower confining pressure levels, higher volumetric dilation occurs (Clough

et al., 1981; Lade & Overton, 1989; Cuccovillo & Coop, 1999). As the initial density increases, the axial strain at failure decreases, thereby resulting in intense volumetric dilation. At a given initial density for all bond strengths and confining pressures, the stresses attained the peak state at the same axial strains, with medium-dense samples being below 5% axial strain and loose ones at 15%. The post-peak response depends on initial density, confining pressure and bond strength, whereas at all confining pressures, the medium-dense specimens display strain softening behaviour.

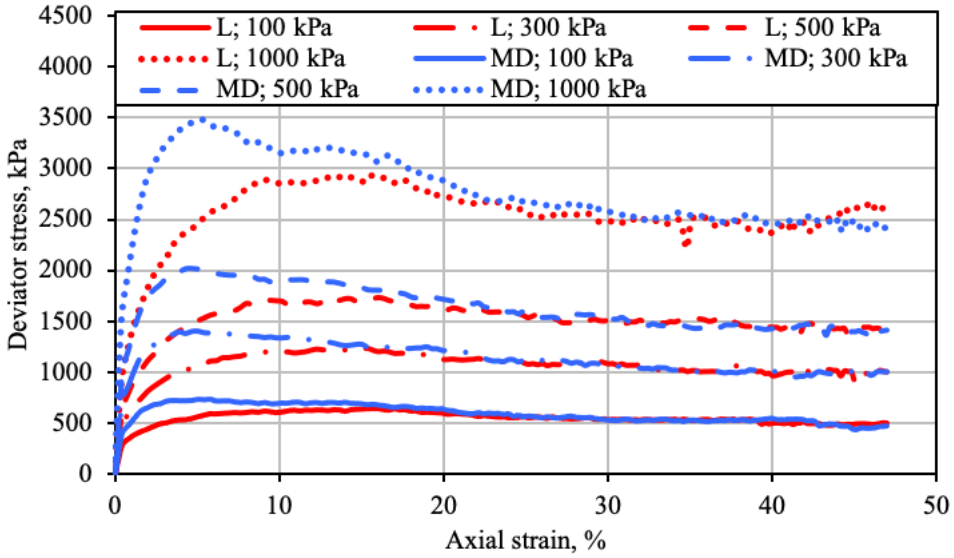

Figure 4. 10. The impact of confining pressure on macromechanical response (deviator stress) of medium dense and loose samples (Γ=20 J/m^2)

The impact of confining pressure on the number of bonds for medium-dense and loose specimens, having a value of bond strength of Γ=20 J/m^2, is indicated in Figure 4.12, whereas the figure also illustrates that rapid and notable bond breakage happens prior to the attainment of the maximum deviator stress.

The same observations in terms of micro and macro responses were found for medium loose specimens.

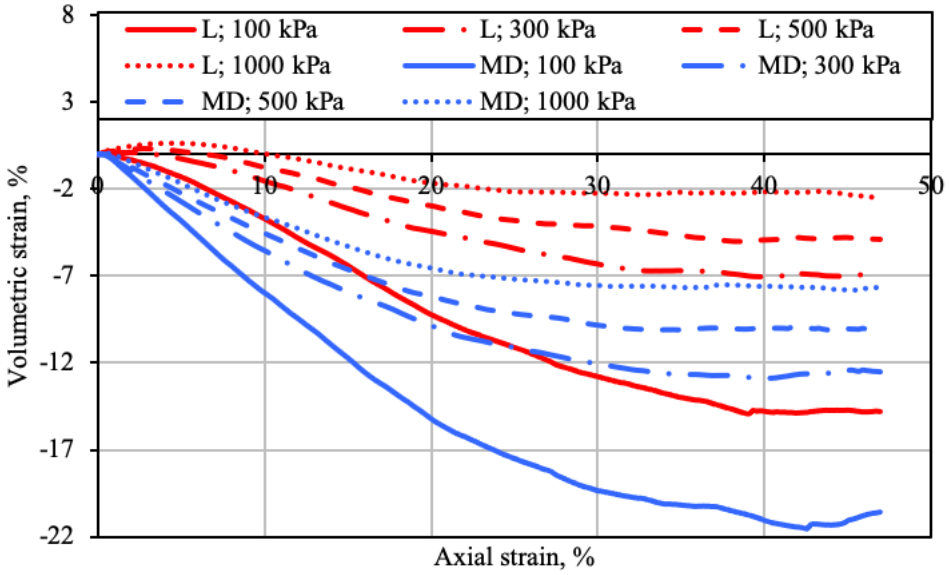

Figure 4. 11. The impact of confining pressure on macromechanical response (volumetric strain) of medium dense and loose specimens (Γ=20 J/m^2)

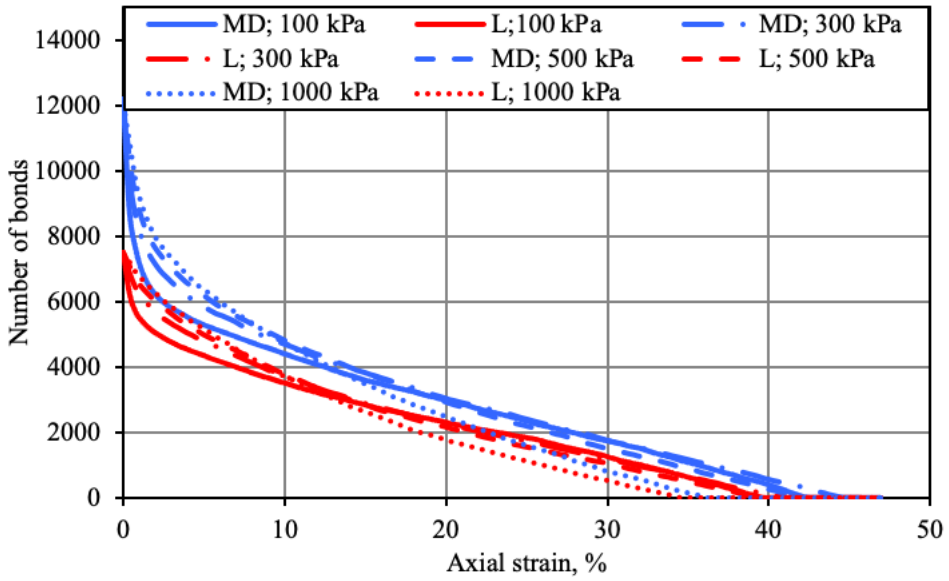

Figure 4. 12. The impact of confining pressure on micromechanical response (number of bonds) of medium dense and loose specimens (Γ=20 J/m^2)

4.4.1 Peak strengths

Figures 4.13, 4.14 and 4.15 depict the Mohr-Coulomb strength envelopes which represent the triaxial compression tests peak strength data for the medium dense, medium

loose and loose specimens, respectively. The envelopes are straight lines with almost the same shape across the scope of 100 to1000 kPa confining pressures, although they have slightly different intercepts. The following equation defines the Mohr-Coulomb strength criterion:

$$\sigma_1' - \sigma_3' - 2c'\cos\varphi' - (\sigma_1' + \sigma_3')\sin\varphi' = 0 \tag{4.2}$$

where and φ' is the angle of internal friction and c' is a unique function of bond strength – the apparent cohesion. For medium-dense systems, the internal friction angles are in the range of 35.1 and 37.8°; for medium-loose systems, the range is between 33.6 and 35.3°, while the loose systems, the figure is $32.5 - 35.5^{\circ}$; with the average values being $36.5^{\circ}, 34.1^{\circ}$ and 33.7° respectively. As reported by Dupas and Pecker (1979), Clough et al. (1981), and Acar and El-Tahir (1986), the laboratory tests indicated similar behaviour. The average value of internal friction angle for medium dense, medium loose and loose specimens was used to calculate the apparent cohesion as follows:

$$c' = \frac{(\sigma_1 - \sigma_3)}{2cos\varphi} - \frac{(\sigma_1 + \sigma_3)tan\varphi}{2} \tag{4.3}$$

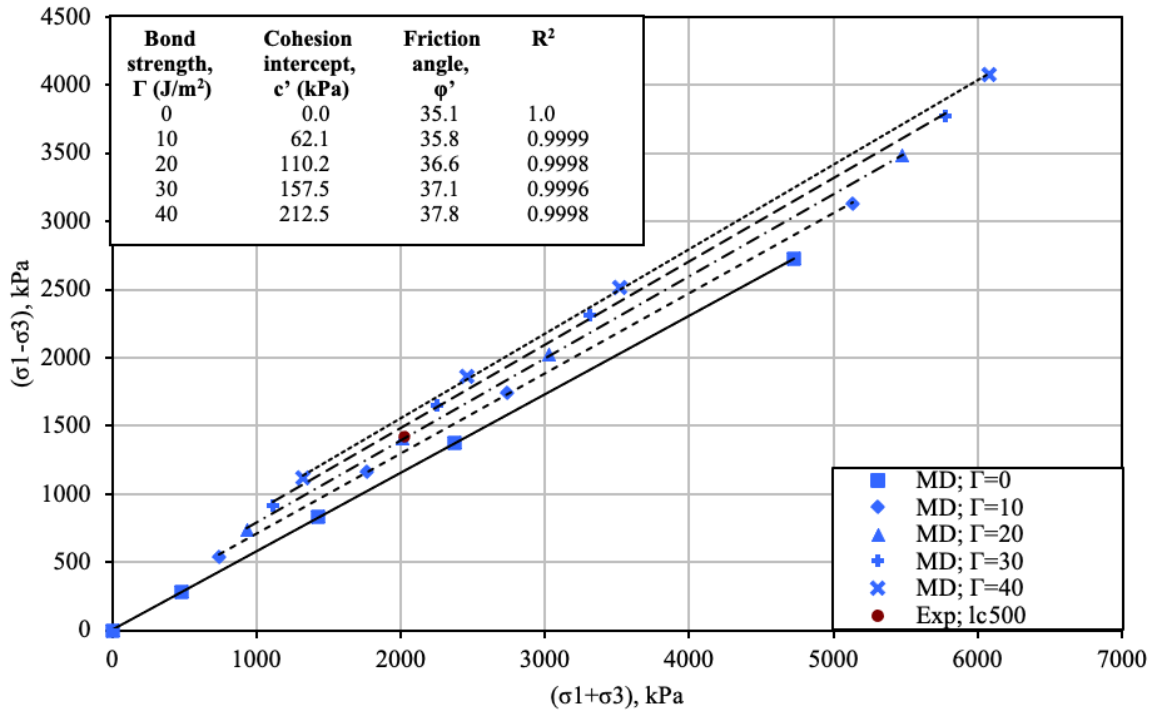

Figure 4. 13. The peak strength data for medium dense systems

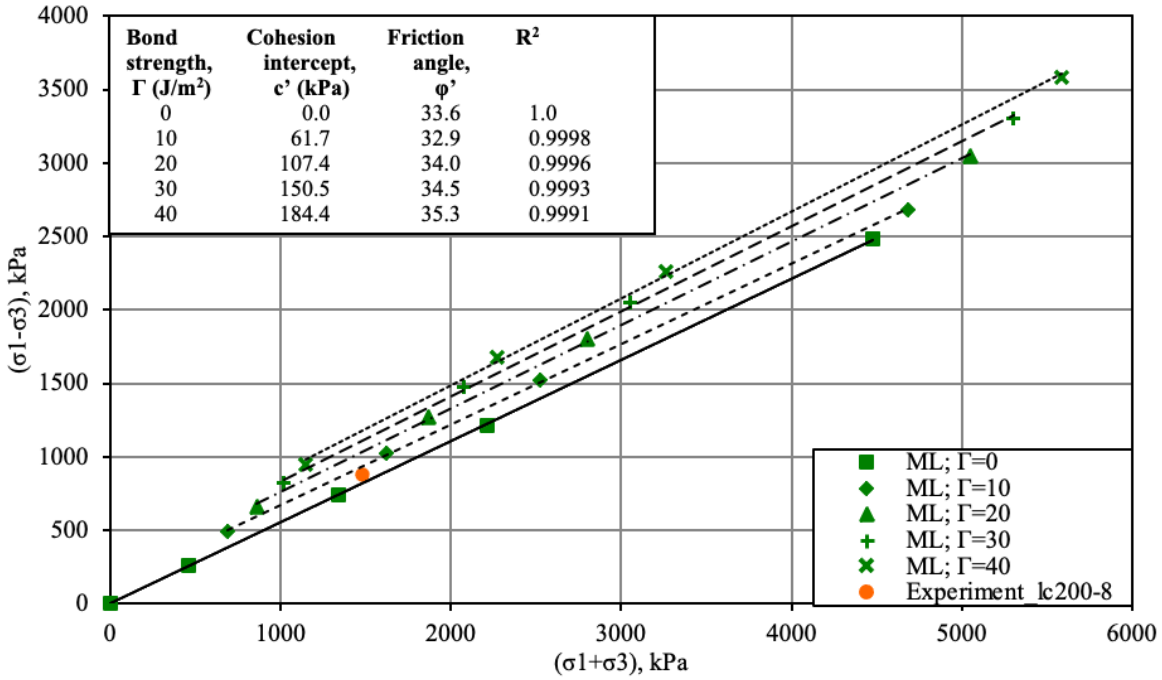

Figure 4. 14. The peak strength data for medium loose systems

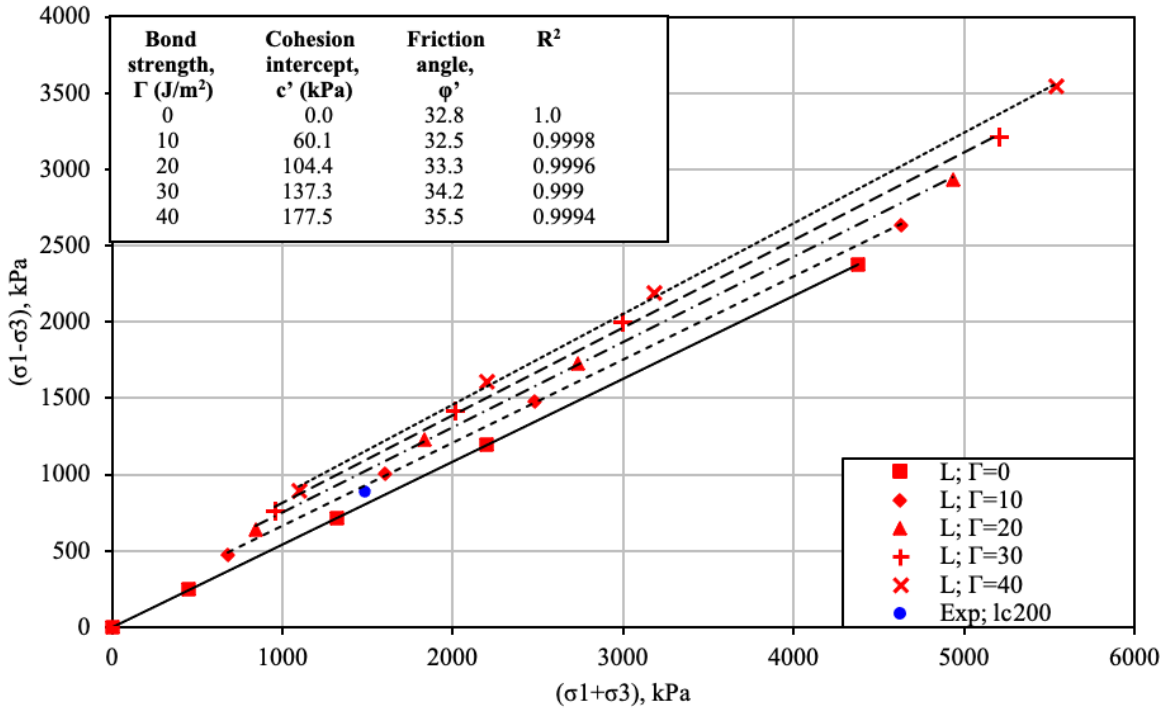

Figure 4. 15. The peak strength data for loose systems

It is indicated in figures 4.13, 4.14 and 4.15 that as bond strength increases, the internal friction angle and the tensile strength also increase. Furthermore, in experiments on cemented sand, the same impacts have been observed (Clough et al., 1981; Lade & Overton, 1989; Schnaid et al., 2001; Airey, 1993; Wang & Leung, 2008a, 2008b and Rios et al., 2014). In comparison with the medium-dense and medium-loose systems, a lower internal friction angle and a smaller apparent cohesion were observed for the loose system. Moreover, the initial density causes a higher friction angle in the case of denser samples. When compared with the looser samples, the denser specimens have more initial cemented bonds; therefore, as the amount of cemented bonds increases, so do the friction angle, tensile strength and cohesion intercept.

According to Clough et al. (1981), density has an appreciable impact on both the nature of the cementing material and cemented soil strength. For all systems, the uncemented sand cohesion intercept equals zero; consequently, dilation leads to the attainment of their peak strengths; whereas in the case of cemented sand, this is caused by cohesive-frictional nature (Coop & Willson, 2003).

Shabdirova et al. (2016) investigated triaxial compression tests on the Ustyurt-Buzachi synthetic sandstone specimens which revealed three peak strength data points: LC500 (medium-dense sample), LC200-8 (medium-loose sample) and LC200 (loose sample). These were added to the Mohr-Coulomb strength envelopes for medium-dense, medium-loose and loose specimens respectively. Figures 4.13 and 4.14 show that the peak strength of LC200 and LC200-8 are located between the slopes of $\Gamma = 0$ J/m^2 and $\Gamma = 10$ J/m^2, while Figure 4.15 shows that LC500 is located on the slope of $\Gamma = 20$ J/m^2. Figure 4.16 depicts how a non-linear correlation was obtained between the Mohr-Coulomb shear strength parameter c' and the bond strength Γ in order to ascertain the precise value of the bond strength as compared with experimental results. Superimposed experimental data points give the values of $\Gamma = 20$ J/m^2, $\Gamma = 6$ J/m^2 and $\Gamma = \sim 6.5$ J/m^2 which ought to be compared with the results of simulations within the laboratory for medium-dense, medium-loose and loose specimens, respectively.

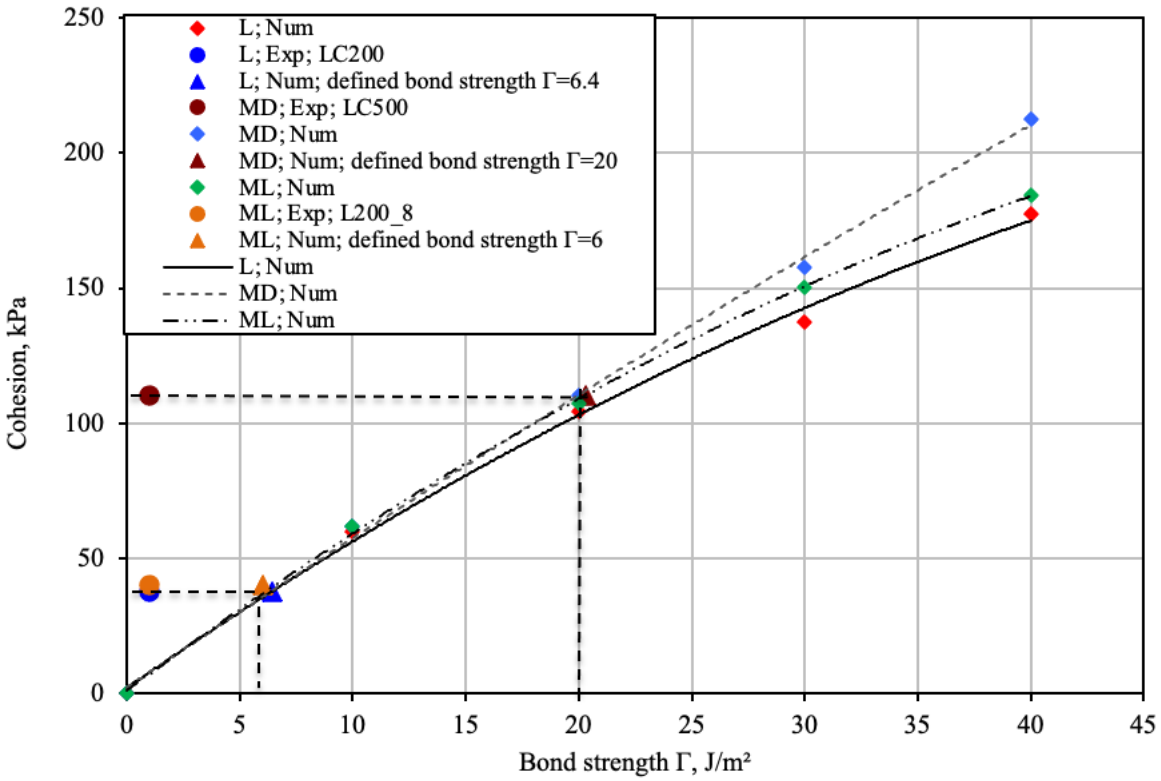

Figure 4. 16. Bond and shear strength parameters correlation for medium dense, medium loose and loose samples

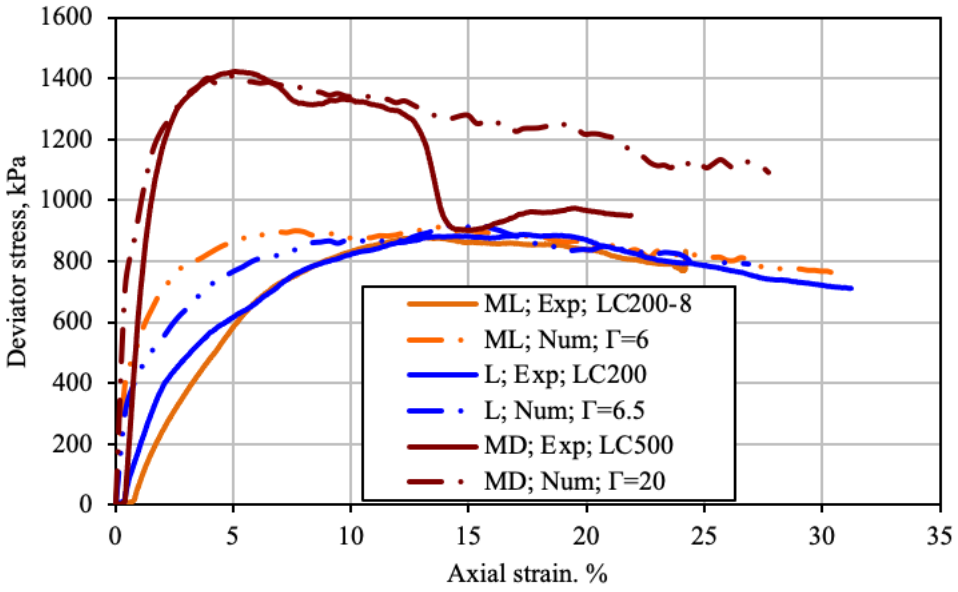

Figure 4. 17. Comparison of laboratory and numerical triaxial compression tests for medium dense, medium loose and loose systems in terms of stress-strain curves

The comparison between the laboratory triaxial compression tests and the numerical data, at 300 kPa of confining pressure, is shown in Figures 4.17 and 4.18. Furthermore, it is evident that the numerical samples' stress-strain responses conformed to the laboratory results, at least with regard to the shear strength. Nevertheless, the numerical specimens contracts by a lesser amount as a result of the difference between cement and interface energy. It should be borne in mind that cement bonds are compressible, and are not considered in the simple modified JKR contact bond model; therefore, the stress-strain curves for the numerical specimens are more stiff.

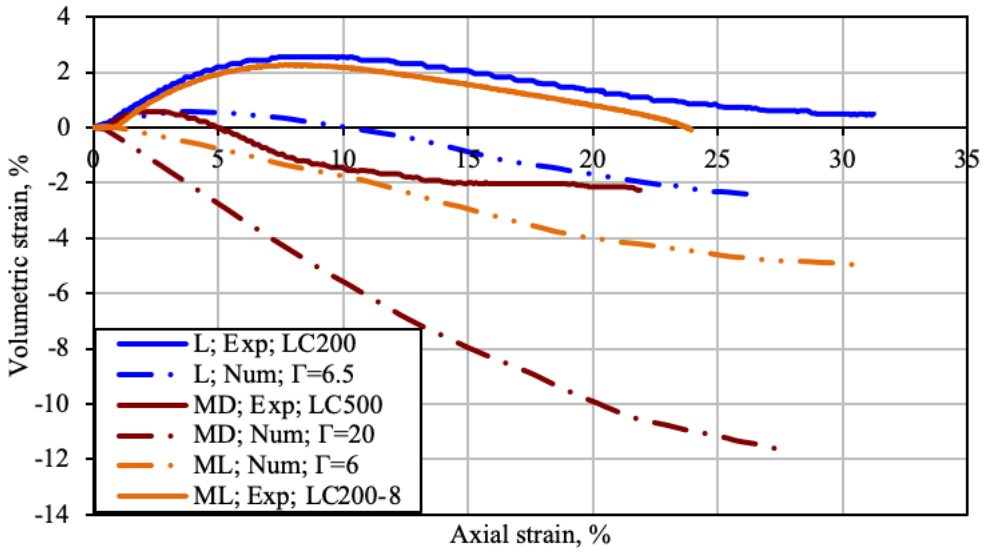

Figure 4. 18. Comparison of laboratory and numerical triaxial compression tests for medium dense, medium loose and loose specimens in terms of volume change curves

Figure 4.19 shows the experimental LC500 and numerical MD (Γ = 20 J/m^2) samples before and after the triaxial compression test.

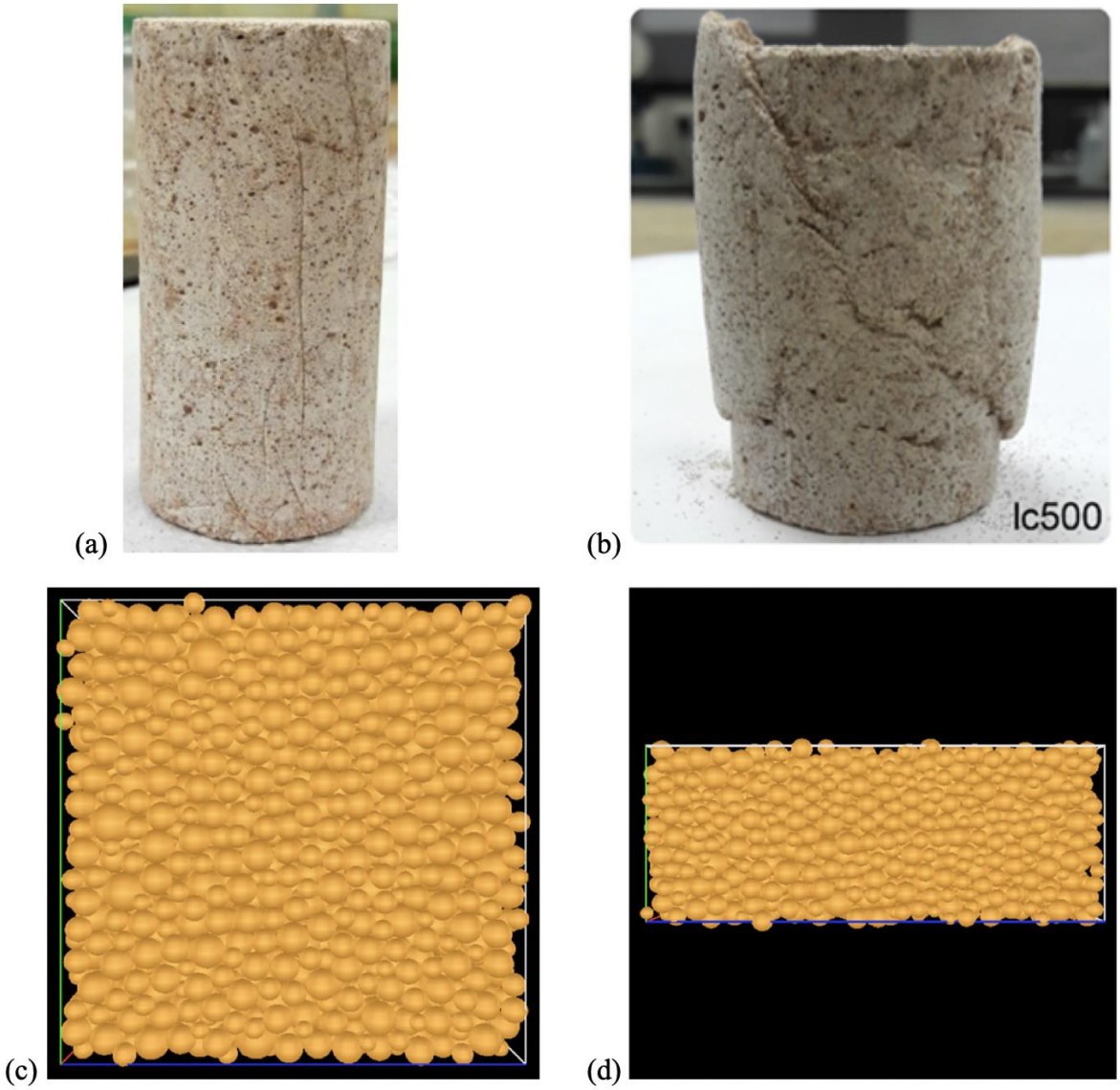

Figure 4. 19. Experimental and numerical samples: (a) experimental LC 500 sample before shearing; (b) experimental LC 500 sample after shearing; (c) Numerical MD sample before shearing; (d) numerical MD sample after shearing

4.4.2 Critical state

The critical state lines (CSL) for the medium-dense, medium-loose and loose specimens in the plane of e - ln p' are shown in Figure 4.20. Initially, the CSL was implemented in order to clarify the behaviour of normally consolidated clay, and it has been utilised for cemented sand materials by only few researchers (Coop & Atkinson, 1993; Airey, 1993; Cuccovillo & Coop, 1999). The full determination of the critical state in a space of *p':*

q: e is somewhat problematic in experiments (Schnaid et al., 2001). This is because of the strain localisation and brittle behaviour was observed for cemented samples. However, the study of the CSL occupies a significant role in determining a general theoretical basis for the cemented sands behaviour.

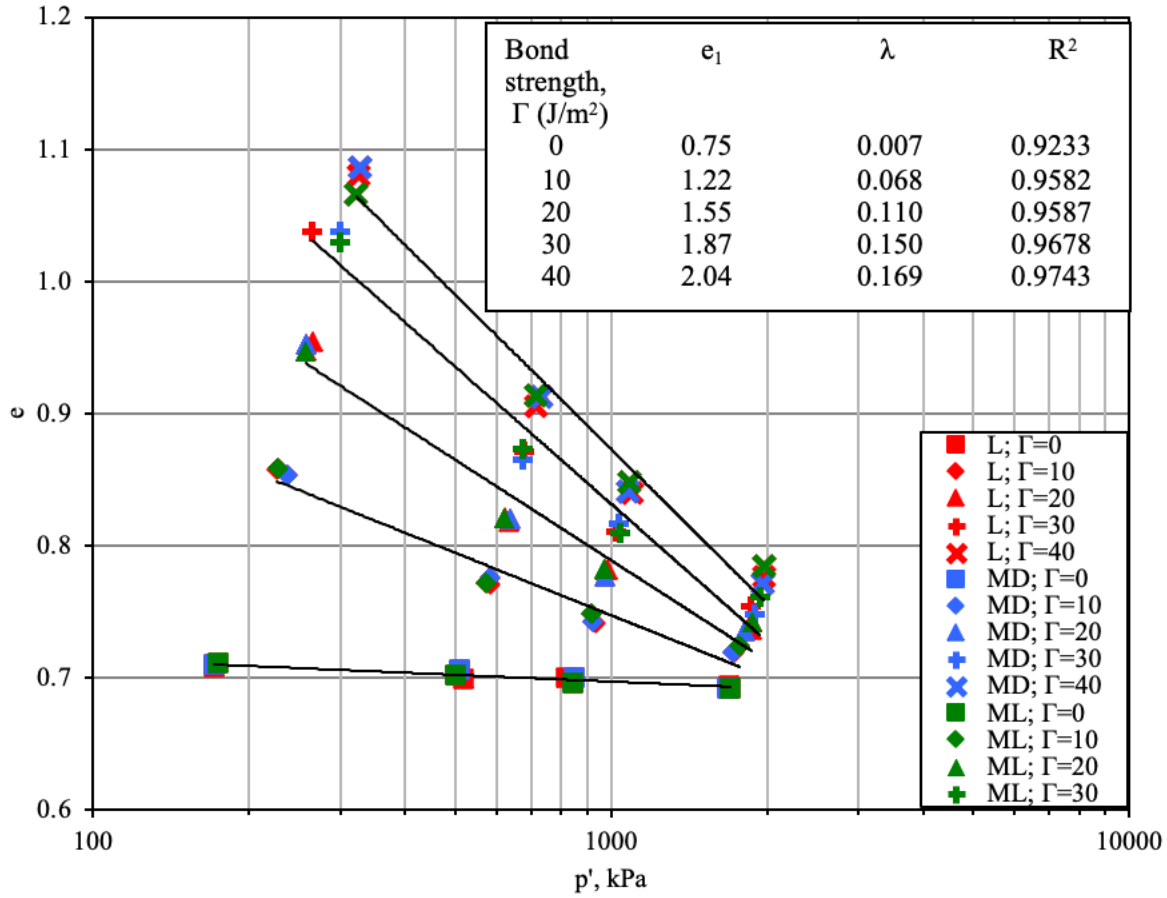

Figure 4. 20. CSL for medium dense, medium loose and loose specimens (e - ln p' plane)

Coop and Willson (2003) imply that it is necessary to shear to strains of at least 30% to attain the CSL for sands, whereas in this research, all of the simulations of triaxial compression tests were performed up to 46% of axial strain. Moreover, Figure 4.20 shows that for a given bond strength value the medium-dense, medium-loose and loose samples all attain the same CSL. The critical void ratio, which is independent of the initial density, increases in line with bond strength; however, it decreases as the confining pressure increases. An increase in the bond strength causes a corresponding increase in the dilation, thereby resulting in a higher critical state void ratio.

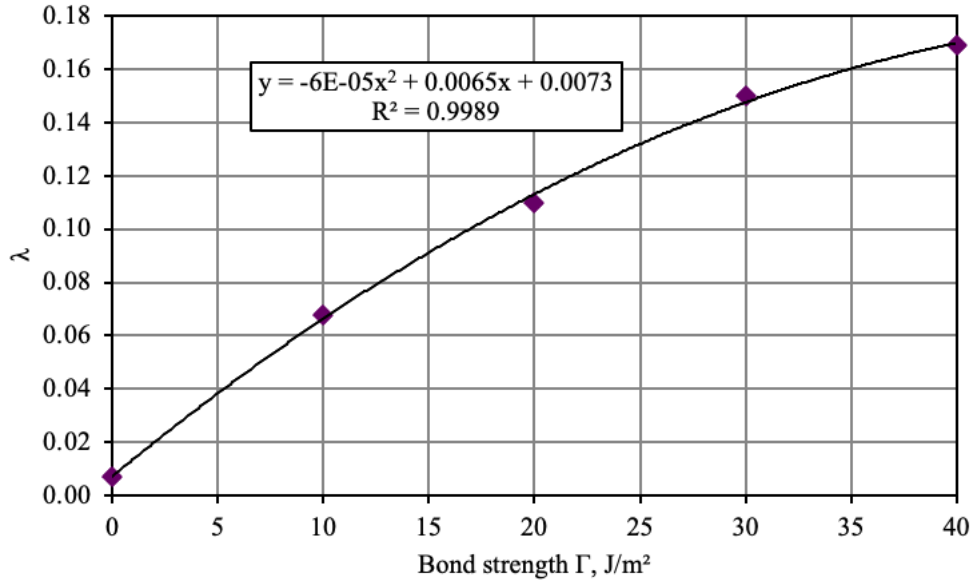

Figure 4. 21. Bond strength and the CSL slope correlation for medium dense, medium loose and loose specimens (e - ln p' plane)

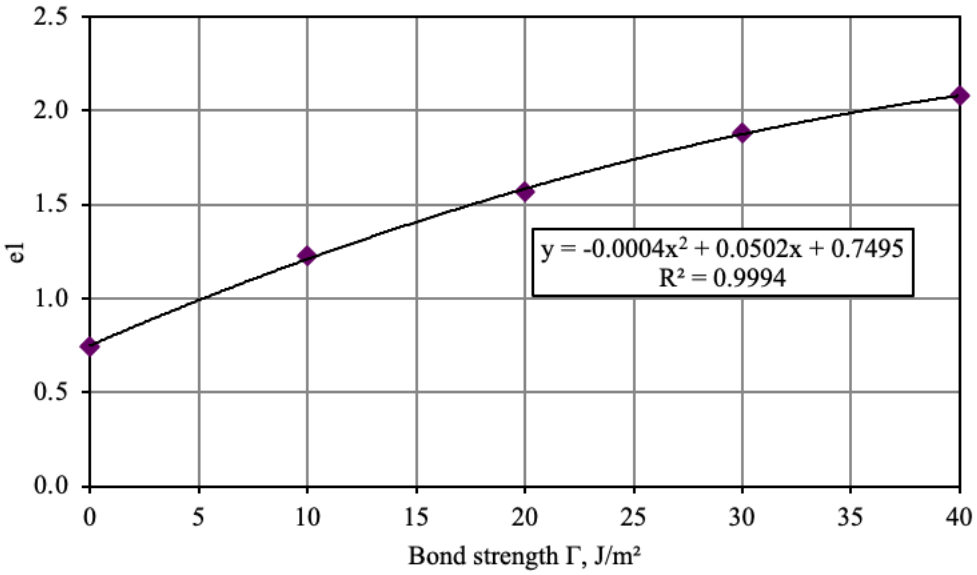

Figure 4. 22. Bond strength and intercept at 1 kPa of the CSL correlation for medium dense, medium loose and loose specimens (e - ln p' plane)

Furthermore, the following equation gives the CSL parameters e_1 and λ:

$$e = e_1 - \lambda \ln p' \tag{4.4}$$

where e is a critical state void ratio, e_1 is the value of e corresponding to p′= 1 kPa on the CSL, and λ is the CSL slope (e - $ln\ p'$). The slope of CSL (compression index) for all specimens, which is in the range of 0.007 to 0.175, increases in line with bond strength. Figures 4.21 and 4.22 illustrate the non-linear correlations between the parameters of CSL Γ and λ and between Γ and e_1 respectively.

4.5 Summary

Various values of bond strength, initial density and confining pressure have been applied to the conducting of triaxial compression tests simulations of cemented sandstone specimens using 3D DEM model. It is revealed by the results that the initial stiffness and peak strength increase in line with the initial density, bond strength, confining pressure. The samples display a greater dilation rate in the case of a higher initial density and bond strength; moreover, bond breakage was found to increase with confining pressure and decrease with initial density and bond strength. Furthermore, the parameters of Mohr-Coulomb strength criterion c' (the inherent shear strength) and φ' (the friction angle) were obtained; and the correlations between the bond strength and shear strength parameters were determined. Subsequently, these relationships were applied to evaluate the bond strength to be used for comparing with the findings of laboratory triaxial tests; moreover, it was evident that the numerical specimens' stress-strain curves conformed to the experimental results of the cemented sandstone regarding the shear strength. The CSL for medium-dense, medium loose and loose systems indicate the independence of the critical ratio of the initial density, despite the fact that this increases as bond strength increases. An increase in bond strength leads to an increased dilation, thereby resulting in a greater critical state void ratio.

The mechanical properties, the PSD and the identified value of bond strength (Γ = 20 J/m^2) of medium dense sandstone sample will be used in further simulations of CPT test in cemented sandstone using 3D DEM approach. These numerical simulations of CPT tests will be then used in sand production simulations as physically penetrated sandstone samples (Chapter 6). The sanding mechanism near the perforation cavity will be further studied.

Chapter 5 – Perforation penetration simulation and validation

5.1 Introduction

In geotechnical engineering, the CPT test is principally used for stratigraphic profiling as well as for the identification and categorisation of soil types. A cone with a sleeve is moved into the ground in order to conduct a field CPT test. The force needed to push the tip of the cone is known as the cone resistance, whereas the force required to push the sleeve through the ground is referred to as the sleeve friction. Moreover, the friction ratio can be identified by the ratio between sleeve friction and cone penetration resistance. These fundamental data can identify the categorisation of the soil type.

In this study, the principal objectives of the numerical investigation of CPT tests were as follows:

- To prepare a physically penetrated numerical sample that can be used to study sand production near the perforation hole (damage zone).
- To use as an application and validation of a developed 3D contact bond model for cemented sandstone.
- To identify and classify the soil type using the SBT classification system.

A concise summary is given in this chapter of the literature associated with the CPT test in granular media, having been explored numerically by applying the DEM method developed by Cundall and Strack (1979). The deep penetration mechanism in granular soils has been numerically (2D) studied by Huang and Ma (1994) and Jiang et al. (2006). Furthermore, the mechanism of inclined CPT tests in the granular ground was numerically (2D) investigated by Jiang et al. (2014). Furthermore, they numerically (2D) studied the CPT mechanism according to various conditions of gravity. Additionally, the CPT test in a calibration chamber was numerically (3D) modelled by Arroyo et al. (2011), Butlanska et al. (2010, 2014) and Cianita et al. (2016). Finally, 3D DEM simulations of CPT tests in sand material (upscaled Ottawa 20-30 sand) were conducted by Khosravi et al. (2019), in which the authors used the SBT charts to interpret the material response as coarse-grained soil.

In this chapter, results from the CPT tests simulations of medium dense cemented sandstone specimens using 3D DEM method are presented. This research extends the recent development of a simple 3D bond contact model for cemented sandstone material presented in Chapter 4.

This Chapter 5 is organized as follows. The numerical simulation of CPT test details and procedure are presented in Section 5.2. The numerical results are described in Section 5.3 and the summary of this chapter is reported in Section 5.4.

5.2. Numerical simulations

Particles in every simulation were regarded as being frictional and elastic, in which the Hertz (1881) theories were applied to calculate the interparticle and wall-particle contact forces with no adhesion. Such calculations established the normal force, and in order to calculate the tangential interaction force, where Mindlin's theory (1949) was utilised. The normal contact force with adhesion was calculated by utilizing a simple 3D bond contact model for cemented sandstone material, and for the tangential interaction force the Mindlin's (1949) no-slip model is used. The detailed information of each interaction force is given in Section 3.3 in Chapter 3.

CPT tests comprised four steps: particle generation, pluvial deposition, compression and cone penetration (Figure 5.1). 10000 frictional elastic spheres were utilised to undertake three-dimensional DEM simulations of CPT tests. Such spheres were bonded together across a range of bond strengths of Γ = 0, 5, 10, 20 J/m^2 (interface energy of adhesion), where Γ = 0 J/m^2 is represented as an uncemented sample. All samples were compressed at 1 MPa of overburden pressure, and particle rotations were prevented in all simulations.

5.2.1 Particle generation

Previously selected 8 various PSD data and material properties of the Ustyurt-Buzachi Sedimentary Basin synthetic samples (Figure 4.1) were reused. These were assessed by the Qicpic dynamics image analyser (Shabdirova et al., 2016). 10000 particles were

randomly generated within a thin rectangular parallelepiped workspace of 8.4 mm width, 21 mm height and 1.4 mm thickness as follows (Figure 5.1a): 0.355 mm (306), 0.3 mm (610), 0.275 mm (1119), 0.25 mm (1973), 0.22 mm (1558), 0.2 mm (1505), 0.18 mm (1750), and 0.15 mm (1179).

According to the Unified Soil Classification System (USGS Open-File Report 2006-1195), these grains passes sieve sizes #45-100, thereby demonstrating that the soil type is S – sand with a subdivision of fine sand. The workspace comprised small 720 DEM boxes (of 0.0007 mm dimension): 30 boxes in height; 12 in width; and 2 in thickness. The following material properties were utilised for all particles: ρ = 2605 kg/m^3 – experimental particle density, ν = 0.3 – Poisson ratio and E = 70 Gpa – Young's modulus.

5.2.2 Pluvial Deposition

A vertical gravity field was applied to the system with every particle being pluvially deposited and forming the initial homogeneous bed (Figure 5.1b). At the workspace base, one finite wall was generated in order to avoid the condition of the periodic boundary at this side. In all walls, the following material attributes of iron were utilised: ρ = 7 900 kg/m^3 – density, ν = 0.29 – Poisson ratio, and E = 210 Gpa – Young's modulus.

5.2.3 Compression

At the top of the deposited specimen, three finite walls were constructed and subsequently moved down, having a 0.1 m/s wall velocity for the purpose of vertically compressing the sample, with such walls imitating the well casing (Figure 5.1c). The interparticle friction and wall friction coefficients were set to $\mu_p = 0.3$ and $\mu_w = 0.3$ respectively, while the vertical stress level (S_v overburdened pressure) attained S_v = 500 kPa. At this point, the bond strength value of Γ = 0, 5, 10, 20 J/m^2 was set and, from that instant, counting commenced on any bond breakage event. The top three wall velocities were reset to 0 when the overburdened pressure reached S_v = 1 MPa.

The overburden pressure is defined as:

$$S_v = \int_0^z \rho(z) g \mathrm{d}z \approx \rho_r g z \tag{5.1}$$

where g is gravitational acceleration, ρ_r is rock density, and z is the depth of interest. The depth of interest, which is equal to 39.1 m, was found by using Equation 5.1.

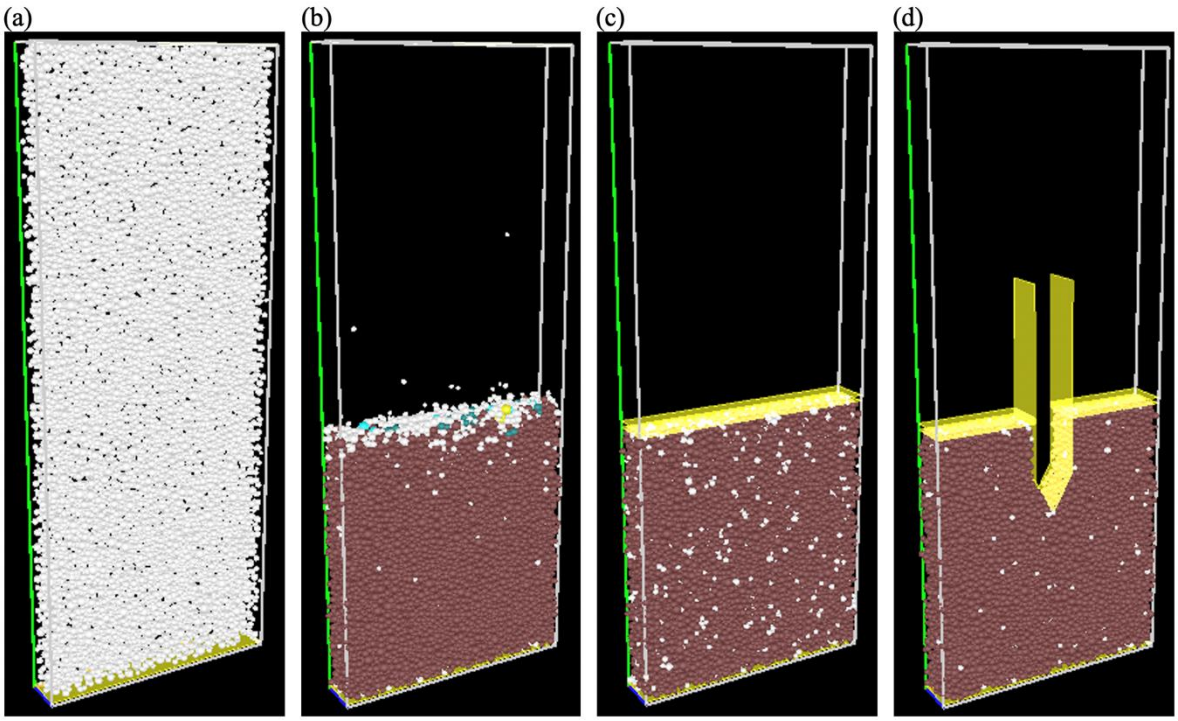

Figure 5. 1. Stages of CPT simulations: (a) particle generation; (b) pluvial deposition; (c) compression; (d) cone penetration. The various colors indicate the cluster size: white particles have one particle in one cluster

5.2.4 Cone Penetration

The top middle finite wall was removed subsequent to the compression of DEM cemented sandstone. At this point, in order to prevent computational cost, a standard cone penetrometer was initially generated above the bed and subsequently pushed down at a high constant rate of 0.1 m/s. The radius (R) of the penetrometer was 0.7 mm and the apex angle was 60^o (Figure 5.2). This was defined as two rigid frictional walls that were inclined at 60^o to the X-axis in order to simulate the cone penetrometer (Jiang et al., 2006), and also two rigid vertical walls whose purpose was to model the sleeve of penetrometer. In the course of simulations, the cone of penetrometer was in contact in about 33-35 particles, thereby providing the resistance value. The initial ground surface is considered as an origin of bed,

and the between the origin and the lowest point of tip is considered as the penetration depth *y*. When the cone tip attained two-thirds of the bed depth, the cone penetrometer was removed from the penetrated specimen.

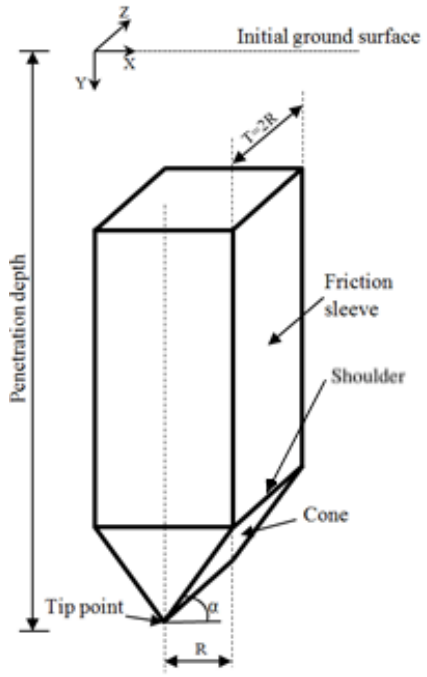

Figure 5. 2. Cone penetrometer (previously modified from Jiang et al., 2006)

5.3 Numerical results

Figures 5.3a, 5.3b and 5.3c indicate the evolution of cone resistance, sleeve friction and friction ratio data at various penetration depths for Γ = 0, 5, 10, 20 J/m^2, respectively. The cone resistance is the vertical pressure measured on the cone:

$$q_c = \frac{\sum f_y}{2Rt} \tag{5.2}$$

where f_y is the contact force acting vertically on the inclined wall (cone), *R* is the cone radius, *t* is the thickness of the bed (*t=2R*), and the sleeve friction f_s is defined as:

$$f_s = \frac{\sum f_y}{2Ht} \tag{5.3}$$

where f_y is the vertically acting contact force on the sleeve and H is the sleeve height within the ground.

It is evident that as the depths increase, the sleeve friction and the cone penetration resistance also increase. The behaviour of a similar character was numerically obtained by Huang and Ma (1994) and Jiang et al. (2006) as well as in the actual field CPT data (Robertson, 1990).

The friction ratio, R_f, was calculated as:

$$R_f = \frac{f_s}{q_c} \cdot 100\% \tag{5.4}$$

where q_c is from Equation 5.2 and f_s from Equation 5.3. The results indicated that the cone resistance and side friction decrease when the bond strength increases.

It is believed that an increase in bond breakage during the penetration procedure might influence the reduction of cone resistance. It was demonstrated by the previous study that bond breakage is more likely to happen for smaller bond strength values of lightly cemented sandstone (Γ = 5, 10 and 20 J/m^2), thereby resulting in displacement or rearrangement of damaged particles. As a result, the number of contacts changes (Figure 5.3d) as do the mechanical average coordination numbers (Figure 5.3e).

The initial number of contacts (at the beginning and end of penetration) increased from 23804 to 30814 (29.45 %), 24075 to 30821 (28.02 %), 23987 to 30713 (28.04 %) and 23683 to 30473 (28.67 %) for bond strength values Γ = 0, 5, 10 and 20 J/m^2 respectively. The increase in the mechanical average coordination number was from 5.33 to 6.373 (19.57 %), 5.347 to 6.392 (19.54 %), 5.322 to 6.353 (19.37 %) and 5.29 to 6.302 (19.13 %) for bond strength values Γ = 0, 5, 10 and 20 J/m^2 respectively. Figure 5.3d indicates that the total number of contacts increases as bond strength decreases. Furthermore, an initial reduction in the number of contacts, when $\Gamma > 0$, which is caused by breaking bonds; subsequently, the increase of the number of bonded contacts and unbonded new ones is at a decreasing rate, being consistent with the previous study (Chapter 4, Figures 4.6 and 4.7).

A high mechanical average coordination number occurs in the case of more/additional contacts between the sand grains. It is possible that mechanical average coordination numbers and/or the high number of contacts could generate a strong force

network. They can also transmit the applied force from the cone and penetrometer sides as noted by Butlanska et al. (2014) and Butlanska (2014).

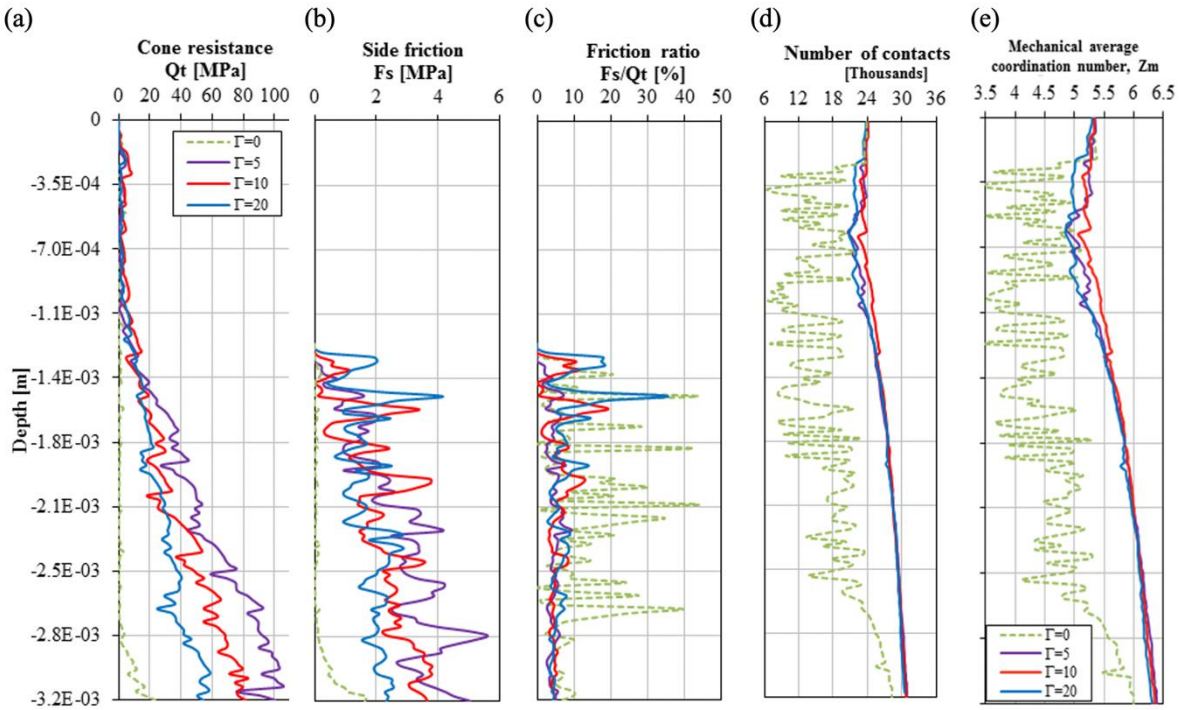

Figure 5. 3. CPT data: (a) resistance of cone; (b) side friction; (c) friction ratio; (d) number of contacts; (e) mechanical average coordination number

Moreover, in this study, the SBT classification system chart (Robertson et al., 1986; Robertson, 1990) is utilized. Geotechnical engineers widely use this chart to interpret/identify the soil type based on the data obtained from the field CPT works.

Use is made of the categorisation system chart, according to the fundamental CPT field (Robertson et al., 1986; Robertson, 1990), only in the case of the sleeve friction, f_s and the total cone penetration resistance, q_t being available (Figure 5.4). The cone resistance may be adjusted in accordance with the cone's total resistance (Campanella and Robertson, 1982) as:

$$q_t = q_c + u(1 - a) \tag{5.5}$$

where u is the pore pressure measured between the sleeve friction and the tip of the cone, and a is the net area ratio calculated as $a=d^2/D^2$, where D is the cone diameter, and d is the sleeve friction diameter. This adjustment ought to consider the impacts of the unequal end area as the water pressure has an effect on the area located immediately behind the cone tip. The

numerical simulations of CPT tests were conducted on dry particles. therefore, the net area, a, was equal to 1 and the presupposition of $q_c = q_t$ was made.

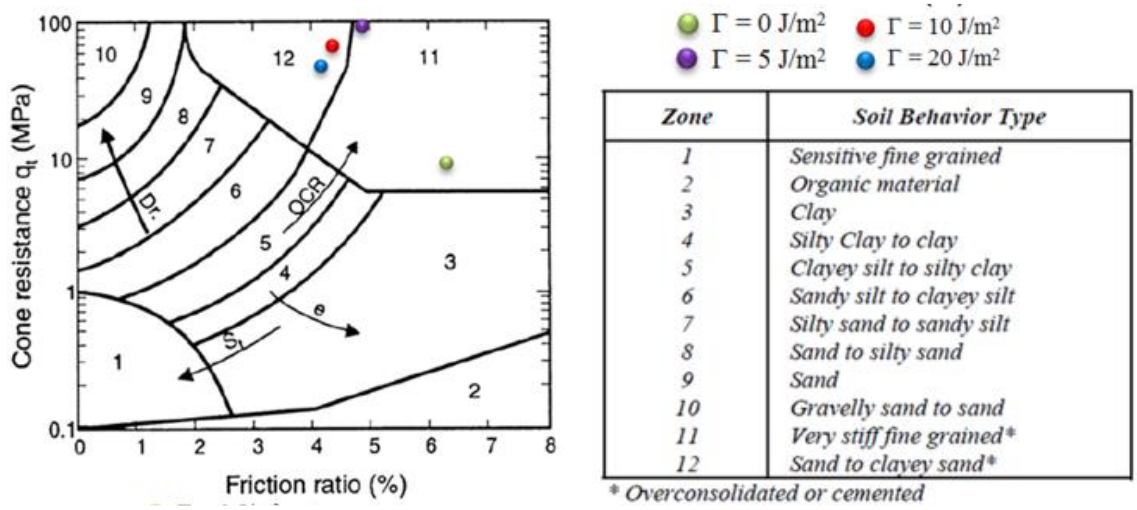

Zone	Soil Behavior Type
1	Sensitive fine grained
2	Organic material
3	Clay
4	Silty Clay to clay
5	Clayey silt to silty clay
6	Sandy silt to clayey silt
7	Silty sand to sandy silt
8	Sand to silty sand
9	Sand
10	Gravelly sand to sand
11	Very stiff fine grained*
12	Sand to clayey sand*

* Overconsolidated or cemented

Figure 5. 4. SBT categorisation technique from CPT data (Robertson et al., 1986)

The CPT data from DEM simulations are further added to the SBT classification chart (Figure 5.4). The numerical CPT data averaged when they became more stable (from a depth of 2.5 mm). The CPT data of samples having higher bond strengths of Γ = 10 and 20 J/m^2 were located in the SBT Zone 12, and recognised as being over-consolidated or cemented sand to clayey sand. Furthermore, Γ = 0 and 5 J/m^2 were located in SBT Zone 11, which behaves as a particularly stiff, over-consolidated fine-grained sand.

The material that exclusively comprises fine sand particles (Figure 4.1, Chapter 4) had a porosity of about 0.38 (end of the compression step). This resembles the porosities that were obtained for medium dense cemented sandstone samples (triaxial compression test simulations) that were compressed at 1MPa and Γ = 0, 5, 10, 20 J/m^2. Consequently, the location of data points for all samples in SBT zones 11 and 12 could be clarified by this.

At the lowest value of bond strength (Γ = 5 J/m^2), it became clear that the bond strength was soft; therefore, more bonds were broken. In comparison with higher bond strength values of Γ = 10 and 20 J/m^2, the Γ = 5 J/m^2 tended to have a behaviour similar to that of uncemented sand and this may explain its location in SBT zone 11. For uncemented sand (Γ = 0 J/m^2), the SBT Zone 11 may be interpreted by an increase in confining pressure and/or initial density, in which case the sand becomes stiffer (frictional response). This type

of behaviour has been obtained from that of fine sand, both numerically in Chapter 4 and experimentally (Kabir et al., 2010).

5.4 Summary

This study used the DEM method in order to conduct the three-dimensional CPT tests simulations in cemented sandstone. Moreover, the Ustyurt-Buzachi Sedimentary Basin synthetic samples were used to generate the actual PSD of sandstone in the numerical simulations. Several numerical CPT tests were undertaken at various bond strength values during which the penetrometer vertically moved down at a constant rate. According to the outcome of the realistic PSD, with increasing depths, the side friction and the penetration resistance increased. Furthermore, as the bond strength increases, the side friction decreases, whereas the friction ratio increases. It was found that the result of numerical CPT tests in cemented sandstone conformed to the SBT categorisation method from CPT data.

These numerical simulations of CPT tests will be then used in sand production simulations as physically penetrated sandstone samples (Chapter 6). The sanding mechanism near the perforation cavity will be studied.

Chapter 6 – Sand production simulations in oil wells

6.1 Introduction

The prediction of the amount of sand production remains a serious problem in the oil and gas industry. Three categories of classified factors and parameters that have an impact on sand production were introduced by Veeken et al. (1991), namely formation, completion and production (detailed information are given in Chapter 2, Subsection 2.1.1). According to these parameters, differences will be apparent in the types of sanding mechanisms (tensile and shear failures, and erosion) and sand production (transient, continuous and catastrophic). Numerical and experimental models of issues involving sand production are the principal means of resolving the sand production difficulty. Nowadays, as computing power has increased the numerical modelling has become a powerful tool for forecasting sand production (Rahmati et al., 2013). Furthermore, in order to improve the modelling of the detachment of particles from the intact sandstone and their transportation with the fluid flow, this may be developed by assimilating the physics of solid and fluid interactions at the micro scale. In order to achieve this, it is necessary for the coupled modelling method to combine the DEM and CFD. The DEM, being a strong instrument for modelling sanding mechanism in which every sand particle is regarded as being a separate entity, was first introduced in 1979 by Cundall and Strack. This technique may be utilised to model the disaggregation of particles from the rock matrix, such as distribution and degradation of rock caused by erosion into small sand particles. This method enables the calculation of the volume and mass of the produced sand and the study of its production mechanism.

Many researchers have conducted numerical studies of the sand production phenomena during the past ~30 years by applying the CFD-DEM since it was introduced by Tsuji et al. (1993). Darcy's Law and the 2D continuity equation were implemented by O'Connor et al. (1997) and Jensen and Preece (2000), who also introduced the usage of 2D CFD-DEM modelling to simulate the sanding problem in oil recovery. They utilised the FEM into the 2D DEM code (MIMES) that was developed at the Massachusetts Institute of Technology. The authors examined the function of the flow rate on the matrix collapse and

the bond strength magnitude respectively. Jensen and Preece (2000) utilised n-sided polygon shapes as sand grains, whereas O'Connor et al. (1997) used irregular particle shapes. The particles, in both studies, were bonded together by cohesive strength, thereby representing cementation of sand particles, in which case consideration was given only to the tensile bond failure mode. Jensen and Preece (2000) stated that the number of particles breaking free from the matrix increased as the bond cohesion decreased.

The 2D Darcy's Law was implemented by Li and Holt (2002) into the 2D DEM code (PFC2D), in which case the fluid flow paths and networks connecting the voids through pipes were modelled. Moreover, in order to study the sanding mechanism, Li et al. (2006) modelled the hollow cylinder tests with fluid flow, thereby solving the 2D Darcy's equation by the FEM with a 2D mesh in the 2D code (PFC2D). Consideration was given to the usage of scaled-up circular disks as particle shapes and bonds between them, thereby presupposing them to be simple beams with strength and normal and shear stiffness. Li et al. (2006), in their simulations, received 3 typical failure patterns similar to those observed in experimental works. If, in the first instance, the material tends towards localised compressive failure because of grain crushing, the failure pattern is a slit-like breakout. With regard to the uniform failure of material adjacent to the borehole, the material was weak in the case of a low tensile strength. Finally, the observed failure pattern was that of dog-eared breakouts when the material was comparatively strong without forming shear bands.

Darcy's Law was applied for all the aforementioned coupling methods for the sand production simulation. However, the Darcy fluid flow is not the ideal way of describing the physics in which the fluid is transporting particles, for the following reasons: 1) it is insufficient to represent the true 3D fluid flow impact during the oil recovery procedure; 2) it is valid only for viscous and slow flow. In order to avert the impact of boundaries, O'Connor et al. (1997) and Jensen and Preece (2000) advocated the use of a considerably greater number of particles. Rahmati et al. (2013) reported that 2D simulations cannot represent tree-dimensional pore flow networks, therefor there is a need of 3D CFD-DEM models to simulate the sand production problem.

In order to simulate the fluid flow effect on sand production, the simplified 1-D fluid scheme was implemented by Cheung (2010) for the sole purpose of calculating the continuity equation into the PFC3D. The scaled-up DEM particles were created in a block sample, and were subsequently bonded by parallel bonds, then compressed for the perforation

simulations. Furthermore, a cylindrical specimen was cut from this block sample, then the inner cylindrical hole was created artificially in order to imitate the perforation hole. Subsequently, this specimen was overlain by fluid cells with cylindrical coordinates, where it was presupposed that the fluid would flow radially from the outer cylinder to the inner perforation hole. This simplified 1-D fluid scheme failed to simulate the total impact of fluid flow because vertical and circumferential flow were regarded as insignificant when the drag force was applied unidirectionally. Although the impact of the fluid flow on the particles was considered, that of the particles on the fluid flow was not. Furthermore, the radial flow was not representative at the perforation tip, due to the multidirectional flow.

In order to model erosion of sand by fluid flow in a lightly-bonded sand material, Zhou et al. (2011) coupled 3D CFD based on the Navier-Stokes equations into the 3D DEM code (PFC3D). Part of the cylindrical domain was utilised as geometry, in which spherical particles (without upscaling) were bonded together; also the linear-elastic law was applied in order to compute the contact forces between particles. They simply created an inner cylindrical hole for the purpose of imitating a perforation hole. The authors deduced that the properties of bond and the fluid flow rate had a major impact on sand erosion. By increasing the fluid rate and decreasing the sand strength, the erosion rate increased. By simulating the simplified conditions, they verified the positive applicability of microscale modelling for the study of sand erosion. The authors suggested to use model boundary conditions to represented field and laboratory conditions in a better way.

Further, 3D CFD model with the Navier-Stokes solvers (PFC3D) was coupled with 3D DEM code by Climent (2016). A sandstone analogue, prepared by Cheung (2010), was utilised by the author for testing under various fluid flow conditions. The author found that as flow velocity increased, the sand production rate and the size of the plastic zone also increased. Nevertheless, this model was limited to considering the impact of pressure gradient on particles, but was unable to represent the fluid pressure on each particle.

By applying Darcy's Law equations, Cui et al. (2016) developed a particle-fluid model (PFC3D), and also suggested a new methodology for porosity dissemination and grid block permeability in response to sanding and deformation. Furthermore, they applied a novel technique for the calculation of sand grain seepage force. Scaled-up spherical particles (bonded by parallel bonds) were created within a rectangular DEM box, which was

subsequently covered with fluid cells in a cylindrical coordinate technique. In order to mimic the perforation hole, the cylindrical borehole was made by a slow grain stiffness reduction within the borehole to zero; moreover, the grains inside the borehole were eliminated. Several tests were conducted on this block-shaped sample under various far-field stresses and pressure conditions. The authors deduced that the following factors influence the size and failure mode: sand production, breakout zone, fluid flow, and also the boundary. Less amount of sand production occurred when the fluid pressure and boundary stresses were high. However, moderate sand production occurred when the strong frictional interlocking as a results of high tangential stresses around the borehole (due to high confining stress). Despite lower far-field stress, a considerable volume of sand was produced at high flow rates.

All of the aforementioned coupling methods utilising sand production simulations and 3D CFD-DEM models were undertaken in PFC3D. With the exception of Zhou et al. (2011), all authors utilised scaled-up DEM particles which they bonded with parallel bonds and a basic perforation method. The authors advocated conducting physical perforation tests and the use of periodic boundaries in order to enhance the calibration procedure. For future work, they suggested the application of DEM particles that resemble authentic grain sizes. Climent (2016) deduced that the parallel bond paradigm calibration remained overly simple. Consequently, the author suggested the need for an improved calibration system having more macro parameters, and also that it would be desirable to upscale the model in capturing the behaviour of fine scale systems in order to extend the knowledge of the fluid-particle interaction in the multiscale method.

This chapter considers all the aforementioned suggestions and presents the three-dimensional CFD-DEM-IBM simulations of sand production problems in oil wells with the sample preparation technique and model setup. The IBM technique is optimised in order to simulate the complicated interaction between the geometry associated with the well completion opening, the fluid flow and the weakly-cemented sandstone under the overburdened pressure and drawdown. The paper presents this technique's ability to capture damage zone caused by the perforation penetration, sand arching, and sanding mechanism (erosion adjacent to the perforation hole) caused by the fluid flow.

This chapter is organized as follows. The model setup and numerical simulation of sand production are presented in Section 6.2, whereas the numerical results are explained in Section 6.3, and Section 6.4 summarises the chapter.

6.2 Model setup and numerical simulation of sand production

Predicting sand production involves numerous multidisciplinary areas, which include: drilling; fluid mechanics; geology; geomechanics; geophysics; petroleum, reservoir and production engineering. Furthermore, a hydrocarbon's field life with its three stages (exploration, development and production) needs to be considered and comprehensively studied. Each stage has particular targets and involves the collection of massive amounts of data for sand production issues. Consequently, it is a difficult and complicated assignment. Veeken et al. (1991) categorised the parameters that affect sand production. However, the numerical modelling of sanding mechanisms is difficult, such models face with numerous limitations. Consequently, this study's objective was not to simulate the actual downhole conditions, but rather to simply them and to reduce the number of parameters. The system configuration considered in the sand production simulations based on the well geometry and design, its trajectory in the formation, and the way it is completed as described in Chapter 2, Section 2.2. As a simulation case and geometry, a cased horizontal well (Figure 6.1a) having a small perforation cavity (Figure 6.1b) that was made by a shaped charge perforation gun (Figure 6.1c) was selected. Its purpose was to attain simplification while imitating the actual conditions for the well-completion category.

All hydrocarbon reservoirs are complex geological heterogeneous bodies having properties such as saturation, permeability and porosity. These vary within the reservoir and are not the homogeneous porous media that are frequently applied in calculations and presented in papers (Dawe, 2004). The objective of current research was to examine the sandstone behaviour and its sanding mechanism. Furthermore, the scale of the area being considered is small (about one small perforation hole); therefore, one lithology regarding cemented sandstone has been selected and considered to be a homogeneous medium. Finally, one liquid phase — oil with low viscosity and density was considered for the fluid characterisation portion.

The previous research on triaxial compression test simulations on medium dense samples (Chapter 4) was used for the rock characterisation part, where a developed simple 3D bond contact model for cemented sandstone material was used. Shabdirova et al. (2016) experimentally studied the material properties of the Ustyurt-Buzachi Sedimentary Basin

synthetic samples which were subsequently reproduced for the numerical specimens (it is worthy of mention that the cemented analogue samples that were studied experimentally were not the core samples of overburdened formations; Zoback (2017) stated that the core samples are never available for extensive laboratory testing). However, the numerical study did not upscale the spherical DEM particles' sizes, meaning that these equalled the actual grain sizes with the particles being connected by interface energy. Every simulation was performed within a periodic cell, thereby indicating an infinite 'sample size' with no 'loading boundaries', there being no finite size impact that could influence the results. Furthermore, the Mohr-Coulomb strength criterion parameters c' (the inherent shear strength) and φ' (the friction angle) were obtained. It was found that these had the optimal match with the experimental results for strength parameters. The stress-strain curves for the numerical samples conformed to the experimental results of the cemented sandstone regarding the shear strength (Figure 4.15, Chapter 4), and the numerical results could explore the microscopic response of experimental cemented sandstone material. Finally, the identified bond strength value for medium dense cemented sandstone sample (Γ = 20 J/m^2) used for comparing with the findings of experimental triaxial tests is utilized for sand production simulations.

Lastly, the sand production simulations were split into five phases: particle generation, pluvial deposition, compression, perforation penetration and sand production. These stages will mimic aforementioned real field conditions: deposition, cementation, compaction, lithification, drilling and completion with casing and cementation (in this study well drilling and cementation are simplified), perforation of sandstone and sand production. The 3D DEM simulations of CPT tests in cemented sandstone with its four phases, undertaken in Subsections 5.2.1-5.2.4, Chapter 5, were reused as a physically penetrated sandstone samples in this research.

The objectives of the current simulation work are 1) to study the sand production mechanism in general; 2) and in particular to study the impact of bond strength and relative gravity (to imitate the vertically upward and downward perforation cavities) on sanding problem. As a result of time limitations, four sand production simulation tests were conducted on medium dense samples and only the initial 0.1 seconds of sanding process immediately subsequent to the perforation penetration in oil wells are studied. These involved a range of bond strengths (interface adhesion energy) of Γ = 5 and 20 J/m^2 that were compressed at 1 MPa of overburdened pressure in upward and downward gravity directions.

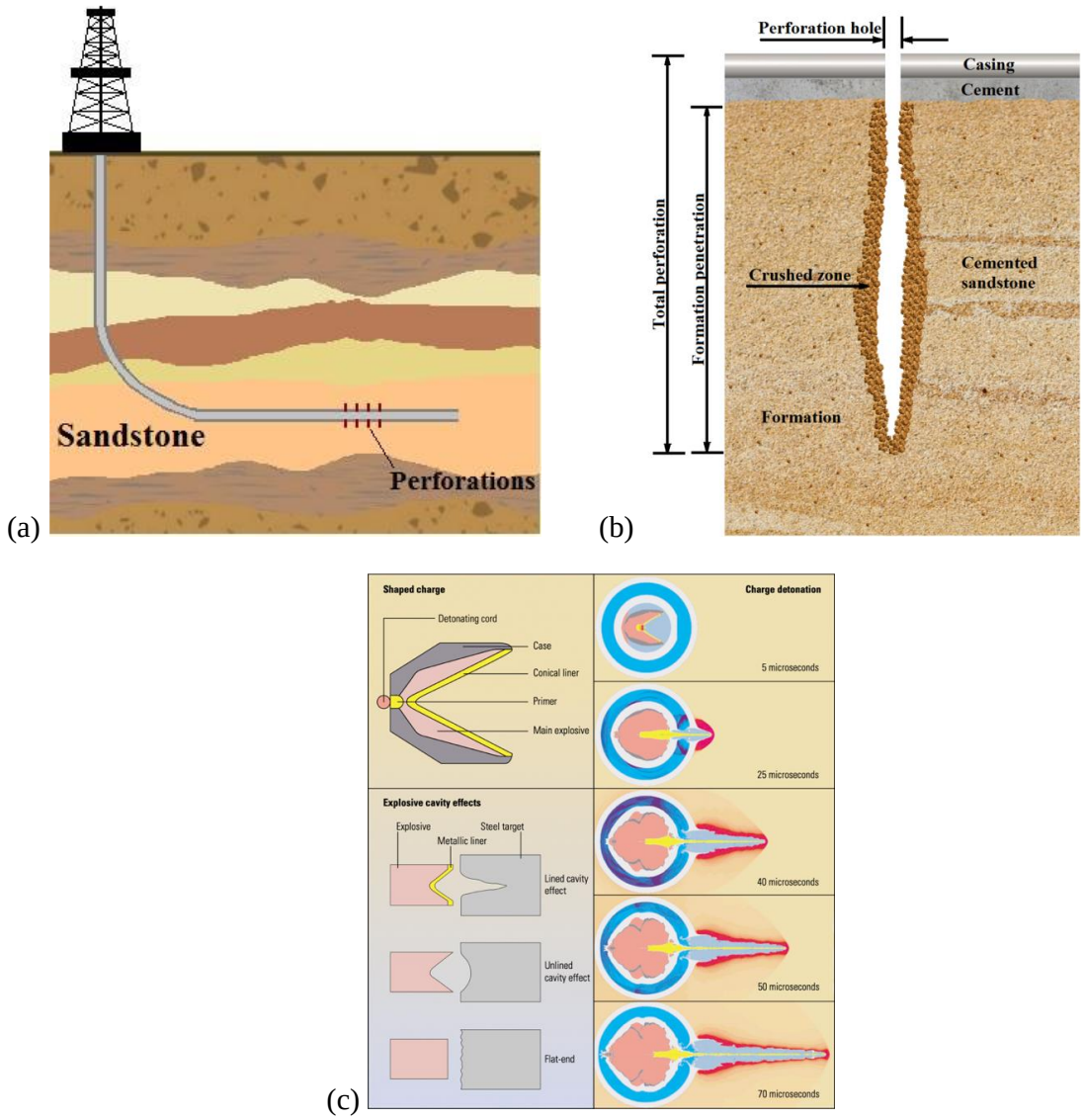

Figure 6. 1. Well-completion: (a) Horizontal well at field scale; (b) Perforation hole; (c) Shaped charge perforation gun (Figure 6.1c adopted from Behrmann et al., 2000)

6.2.1 Sand Production

The oil with a density of ρ_{oil} = 850 kg/m^3 and shear viscosity η_{oil} = 0.52·10^{-3} Pa·s^{-1} were utilised as reservoir fluid properties for sand production simulation (Agada et al., 2014). The following fluid boundary conditions were set for numerical samples: impermeable free

slip for the front and back sides, periodic boundaries for right and left sides, and prescribed pressure for the top and bottom sides.

Further, the top two walls represented the horizontal well with a cased and perforated completions. They are not necessarily located to coincide with any fluid cell boundary since their locations depends on desired value of overburden pressure. Therefore, it was essential to ascribe the two walls with a vertical thickness at least equal to the fluid cell dimension for the purpose of regarding them as immersed boundaries. Consequently, the top and bottom boundaries of the 'thick' walls were mapped into various fluid cells, each of which could be considered to be an immersed boundary (with slip and impermeable conditions) utilising IBM.

In order to imitate the actual field pressure drawdowns, various pressures were specified for the bottom and top boundaries. These drawdowns were the difference between the reservoir pressure P_r and the flowing wellbore pressure P_w that drives fluids into the wellbore from the reservoir.

It was presupposed that the reservoir pressure would equal the pore pressure at depth, where it is defined as a scalar hydraulic potential acting in an interconnected pore space at depth:

$$P_p \approx P_r = \int_0^z \rho_{oil}(z) g \mathrm{dz} \approx \rho_{oil} g z_{oil} \tag{6.1}$$

where, z_{oil} = z = 39.1 m, being a depth of interest (depth, where oil locates). The depth of interest was computed by applying Equation 5.1, and the reservoir pressure at 39.1 m was found by using Equation 6.1, being equal to P_r = 326 296 Pa (pressure at the bottom side of specimen). It was presupposed that the wellbore pressure would equal P_w = 101 325 Pa (pressure at the top side of the specimen).

6.3 Numerical Results

Figure 6.2 depicts the sand production at 0.1 sec for bond strength values Γ=5 and 20 J/m^2 for downward perforation geometry as shown in Figure 6.1b. Furthermore, Figures 6.3a and 6.3b indicate their cumulative amount and mass of produced sand grains. At 0.1 sec, the number of produced sand grains (Figure 6.3a) were 705 and 606. The masses (Figure 6.3b)

were 11.54 mg (6.7 % of the total mass) and 9.78 mg (5.6 %) for bond strength values Γ=5 and 20 J/m^2 respectively. It is evident that the number of produced sand particles increases as the bond strength value decreases.

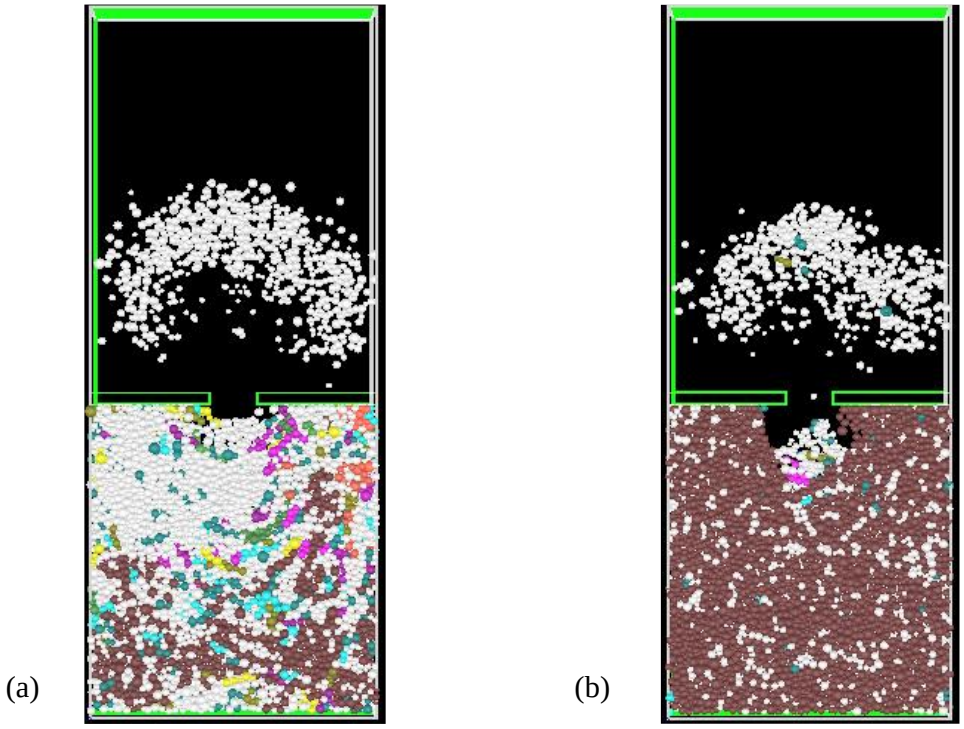

Figure 6. 2. Sand production at 0.1 sec: a) Γ=5 J/m^2; b) Γ=20 J/m^2. The various colours represent the cluster size: white particles have one particle in one cluster; light cyan – 2; dark cyan – 3; light yellow – 4; dark cyan – 5; magenta -10; green -50; brown – over 2000 particles)

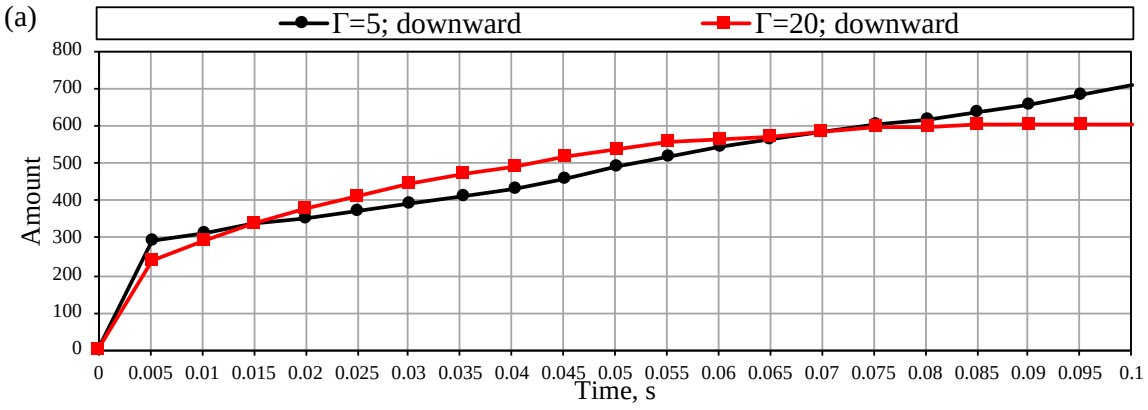

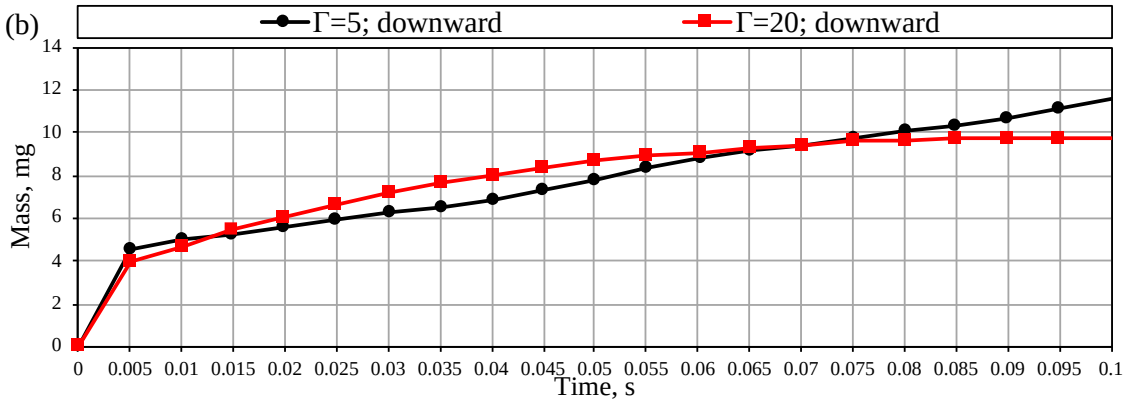

Figure 6. 3. Sand production at 0.1 sec: a) cumulative amount of produced sand grains; b) cumulative mass of produced sand

6.3.1 Impact of relative gravity direction

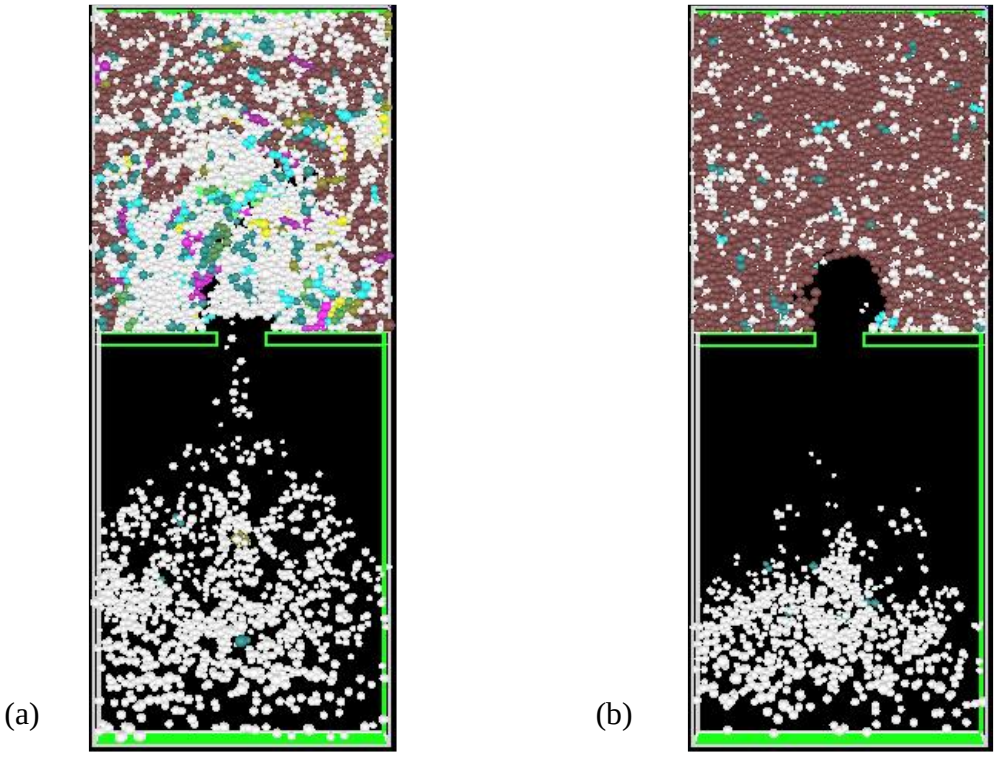

Figure 6. 4. Sand production at 0.1 sec: a) Γ=5 J/m^2; b) Γ=20 J/m^2

Figure 6.1a shows that the perforation may be vertically upwards in horizontal cased oil wells. In these simulations, this simply needs the gravity direction and the visualisations to be rotated through 180 degrees. Furthermore, Figures 6.4a and 6.4b indicate the sand production at 0.1 sec for bond strength values Γ=5 and 20 J/m^2 with vertically upward perforation penetrations respectively. Figures 6.5a and 6.5b demonstrate the comparison of the cumulative amount and the mass of produced sand grains for vertically downward (solid lines) and upward (dash lines) perforation penetrations respectively. At 0.1 sec, the number of produced sand grains for vertically upward perforations are 1052 and 720 (Figure 6.5a). The masses are 17.49 mg (10.1 %) and 11.64 mg (6.7 %) for bond strength values Γ=5 and 20 J/m^2 (Figure 6.5b) respectively. In the same way as with the vertically downward perforations, it was evident that the number of produced sand particles increases as bond strength value decreases. In comparison with the upward penetrated samples, vertically downward penetrated sandstone samples produced fewer sand particles. Furthermore, as depicted in figures 6.2a and 6.2b, produced sand particles from downward perforated samples began to settle onto the well casing surface because of the direction of downward gravity.

The behaviour of sanding initiation for vertically upward perforated sample with Γ = 20 J/m^2 until 0.055 sec was next analysed. When the sand production simulation started, at 0.001 sec the number of tensile forces increased at the cavity wall in all samples and the perforation cavity formed the shape of a spherical cavity (Figure 6.6). As witnessed by Bratli and Risnes (1981), the sand production commenced when the tensile failure criterion occurred and the thin inner shells around cavities in unconsolidated and wet sand collapsed. Moreover, Van den Hoek et al. (2000a) stated that tensile failure may not occur in open holes, but only in small holes such as perforations. This is because, for a large cavity such as an open hole, shear failure always precedes tensile failure. The size impact means that a small cavity, such as a perforation, has a considerably greater threshold for shear failure. Consequently, although tensile failure may happen first, this will only just precede shear failure, even in the case of small cavities.

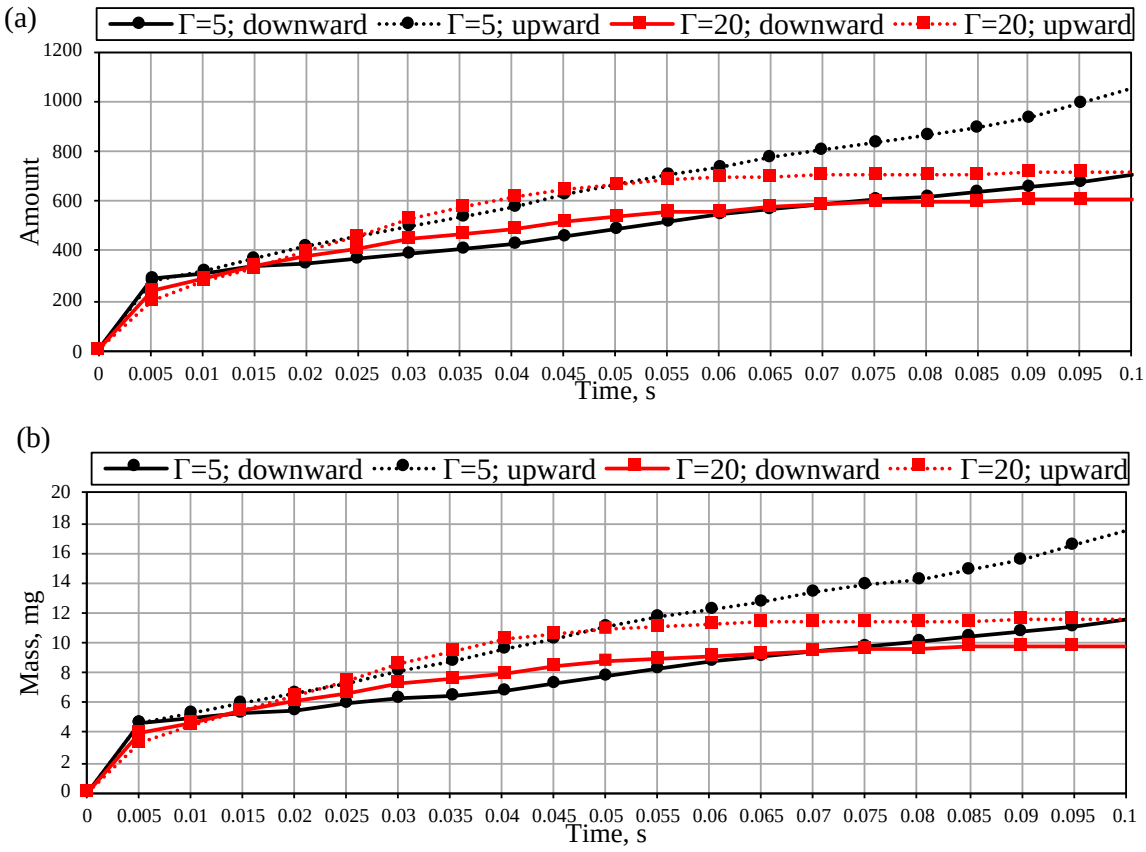

Figure 6. 5. Sand production at 0.1 sec: a) cumulative amount of produced sand grains; b) cumulative mass of produced sand

A sand arch formed around the cavity at 0.001 sec (Figure 6.6), whereas Han and Cundall (2016) numerically captured the same arch for unbonded particles. However, the authors indicate that the arch's self-sustaining ability is exclusively provided by the frictional resistance of contacts. Moreover, after 0.025 sec, the sand arch began to collapse, and a bunch of particles was produced for a short time at 0.03 sec. Consequently, at 0.03 sec, the peak of the amount of sand grains and the mass of produced sand was detected, and the particles appeared late in comparison with lowest bond strength values because of the arch's stability. Subsequently, the arches collapsed and reformed. All of the sand particles located above the formed sand arch washed out from the previously collapsed arch (within the time range of 0.01 – 0.025 sec). This procedure happened in all samples in which the peaks of produced sand grains (amount or/and mass) showed when the sand arches had collapsed.

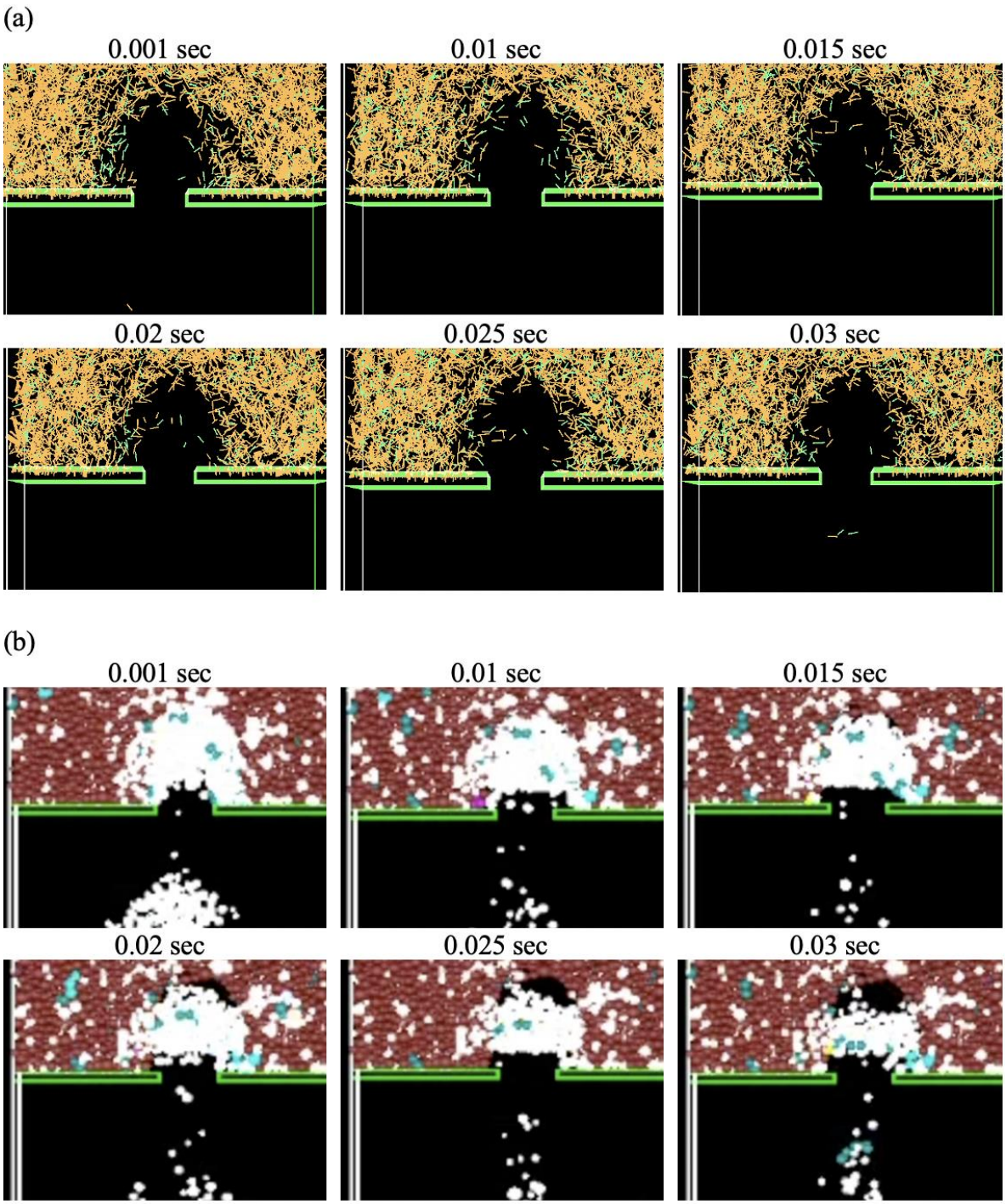

Figure 6. 6. Sand arch regarding (a) contact forces: compressive (orange) and tensile (mild green); (b) clusters for vertically upward perforated sample with $\Gamma = 20$ J/m^2

If only bond-free particles in the perforation zone (uncemented particles) are considered, then there is a possibility of sand arching only when a specific number particles attempts to exit through a narrow tunnel simultaneously, thereby creating a chain. Unless

there is a sufficient number of particles, it is impossible to form the arch, and the number is determined by the perforation hole size. Therefore, until this happens, it is impossible for unbonded particles to emerge, in the same way as crowds during an evacuation.

According to Carlson et al. (1992), the fluid flow initiation and the drag forces related to it cause the sanding onset, whereas the sand particles detach from the rock matrix and then moves to the perforation cavity. The authors are of the opinion that a stable arch is formed in the vicinity of the entrance to a perforation cavity. The impact is in direct proportion to the fluid viscosity and velocity, as well as to the high-pressure differentials during drawdown. The arch's stability is dependent on the constant flow velocity and drawdown. Furthermore, when the flow velocity and the drawdown change, the arch collapses and a new one is created.

The sand arches were also reformed for the lowest bond strength values (Γ = 5 J/m^2); however, they were unstable, and collapsed rapidly until 0.005 sec was reached. In the case of highly damaged sandstone, where the cavity size of the perforation expands, it became apparent that the impact of the arch was invisible. However, the sand arches were more stable with greater bond strength values (friction angle and cohesion intercept).

Figures 6.7a and 6.7b depict the average porosity contours, whereas figures 6.8a and 6.8b indicate the contours of mechanical average coordination number of weakly-cemented sandstone at the beginning of sand production (0 sec) for Γ = 5 and 20 J/m^2 respectively. Figures 6.9a and 6.9b indicate the average porosity contours at 0.1 sec of sand production for vertically upward, while figures 6.9c and 6.9d depict the sample for downward perforation cavities for Γ = 5 and 20 J/m^2 respectively. It was evident that sand erosion at 0.1 sec caused the porosity of samples to become looser, in comparison with their initial conditions at 0 sec. It was also apparent that the erosion of sandstone samples with upward and downward perforations was extended continuously from 1 - 1.5R until ~6R for Γ=5 J/m^2; and ~3R for Γ=20 J/m^2.

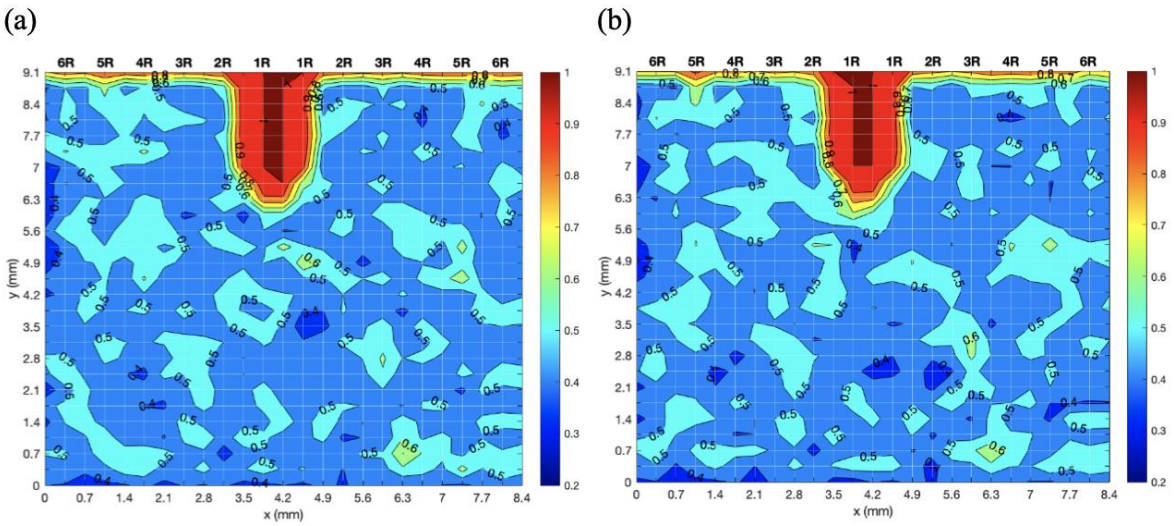

Figure 6. 7. Contours of average porosity at 0 sec of sand production / end of perforation penetration: (a) Γ=5 J/m^2; (b) Γ=20 J/m^2

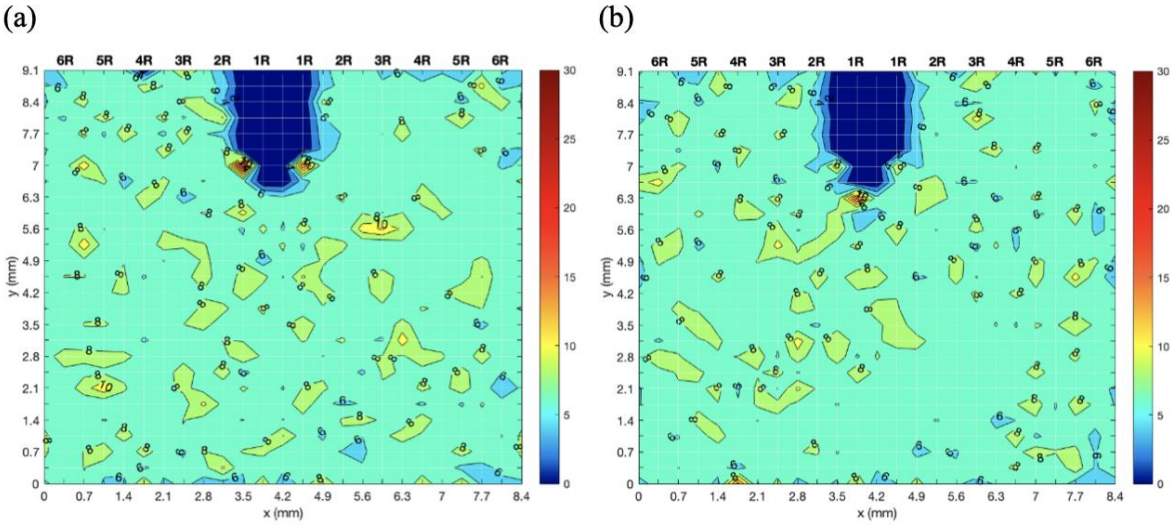

Figure 6. 8. Contours of mechanical average coordination number at 0 sec of sand production / end of perforation penetration: (a) Γ=5 J/m^2; (b) Γ=20 J/m^2

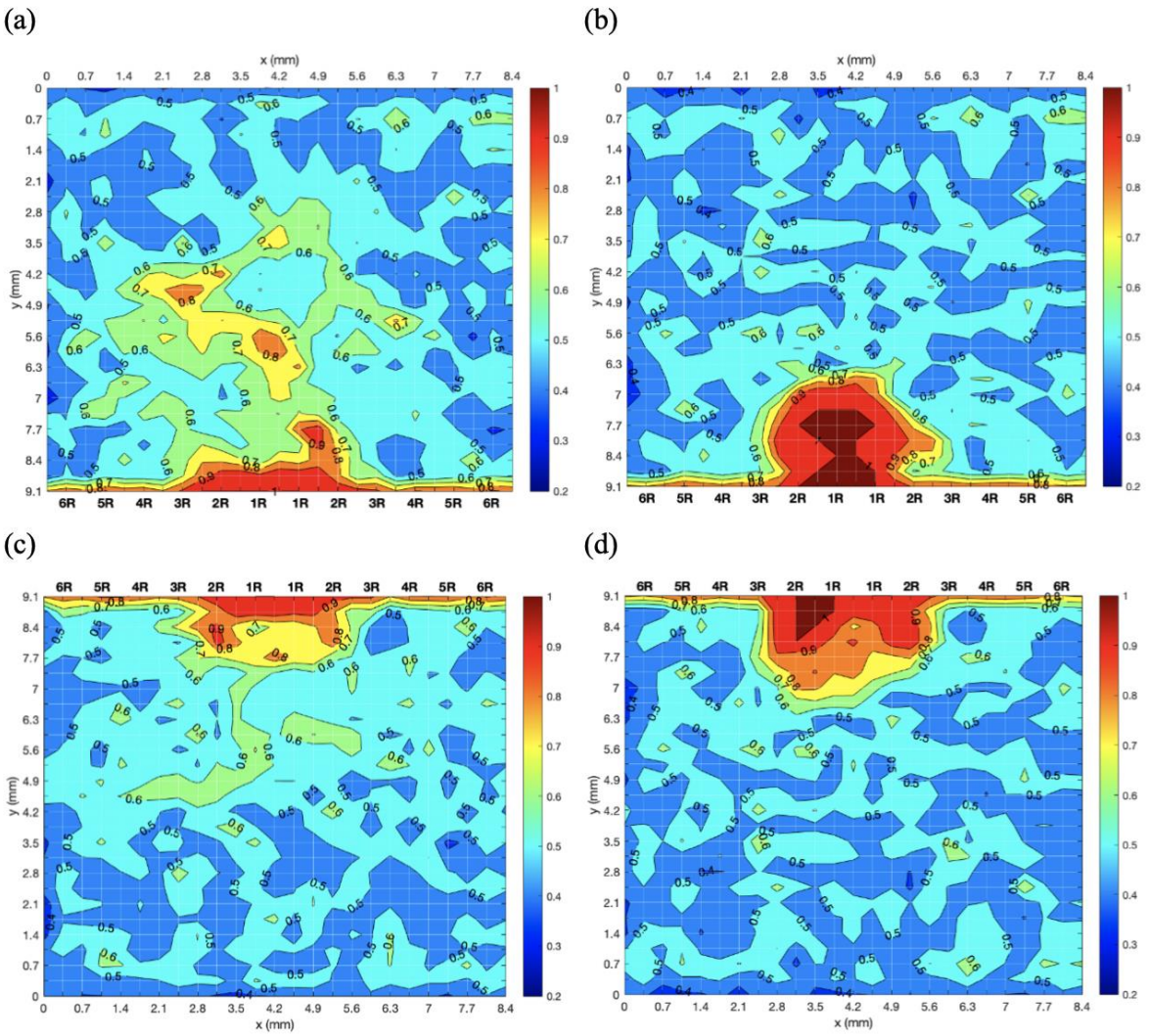

Figure 6. 9. Contours of average porosity at 0.1 sec of sand production for upward: (a) Γ=5 J/m2; (b) Γ=20 J/m2; and downward perforation cavities: (c) Γ=5 J/m^2; (d) Γ=20 J/m^2

Moreover, the mechanical average coordination number contours were plotted for vertically upward (Figures 6.10a and 6.10b) and downward perforations (Figures 6.10c and 6.10d) at 0.1 sec of sand production for Γ=5 J/m^2 and Γ=20 J/m^2 respectively. It was evident that mechanical average coordination numbers were subject to noticeable change adjacent to the perforation cavity. Furthermore, the reduction in mechanical average coordination numbers, which corresponds to an increase in porosity, was extended until ~6R zone for Γ=5 J/m^2; and ~3R for Γ=20 J/m^2. Particles located within the deep blue zone carry a possible risk area for sand production. Figures 6.10a and 6.10c distinctly indicate the skeleton of the remaining cemented sand for Γ=5 J/m^2 for both upward and downward perforations at 0.1 sec.

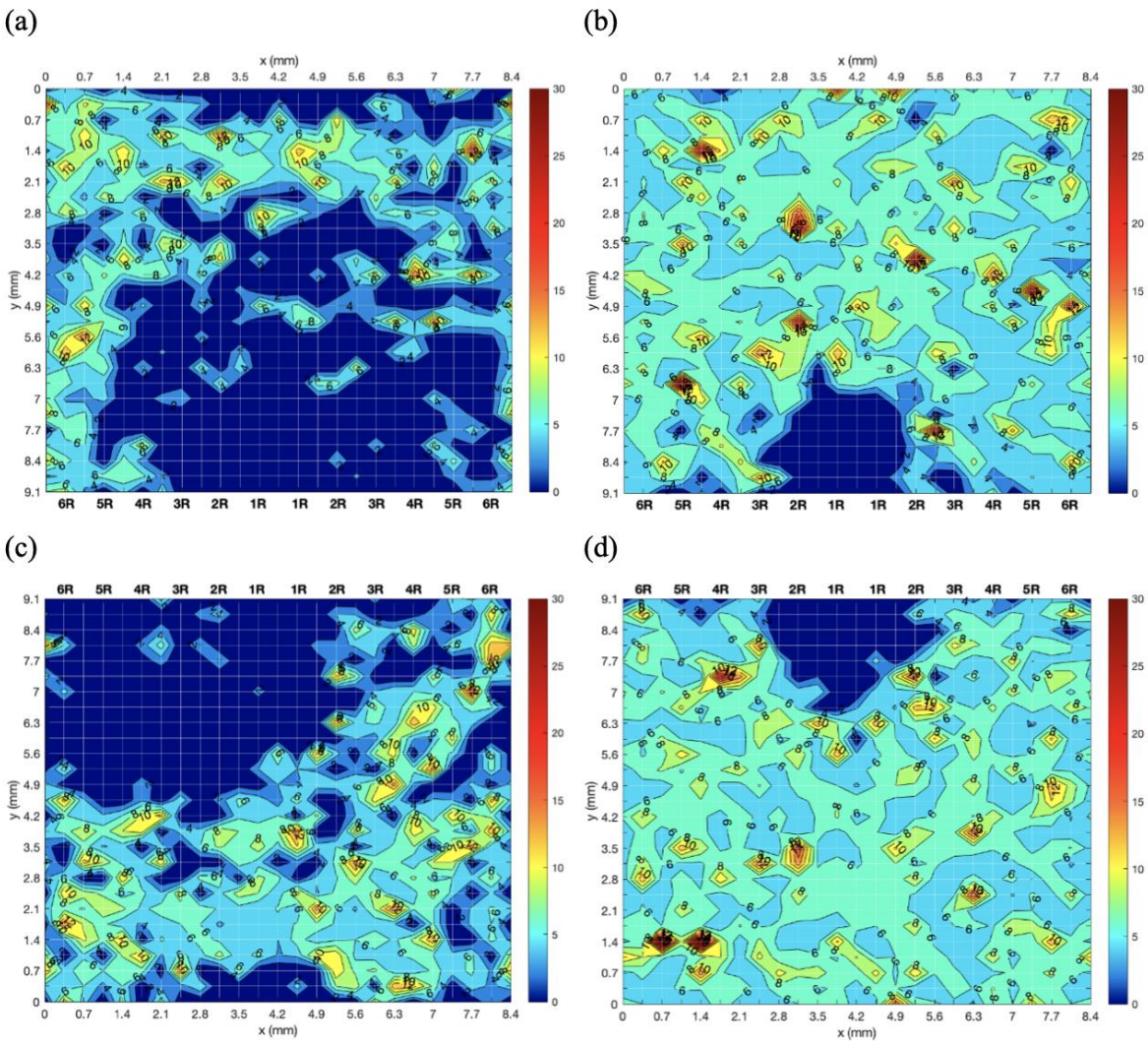

Figure 6. 10. Contours of mechanical average coordination number at 0.1 sec of sand production for upward: (a) Γ=5 J/m^2; (b) Γ=20 J/m^2; and downward perforation cavities: (c) Γ=5 J/m^2; (d) Γ=20 J/m^2

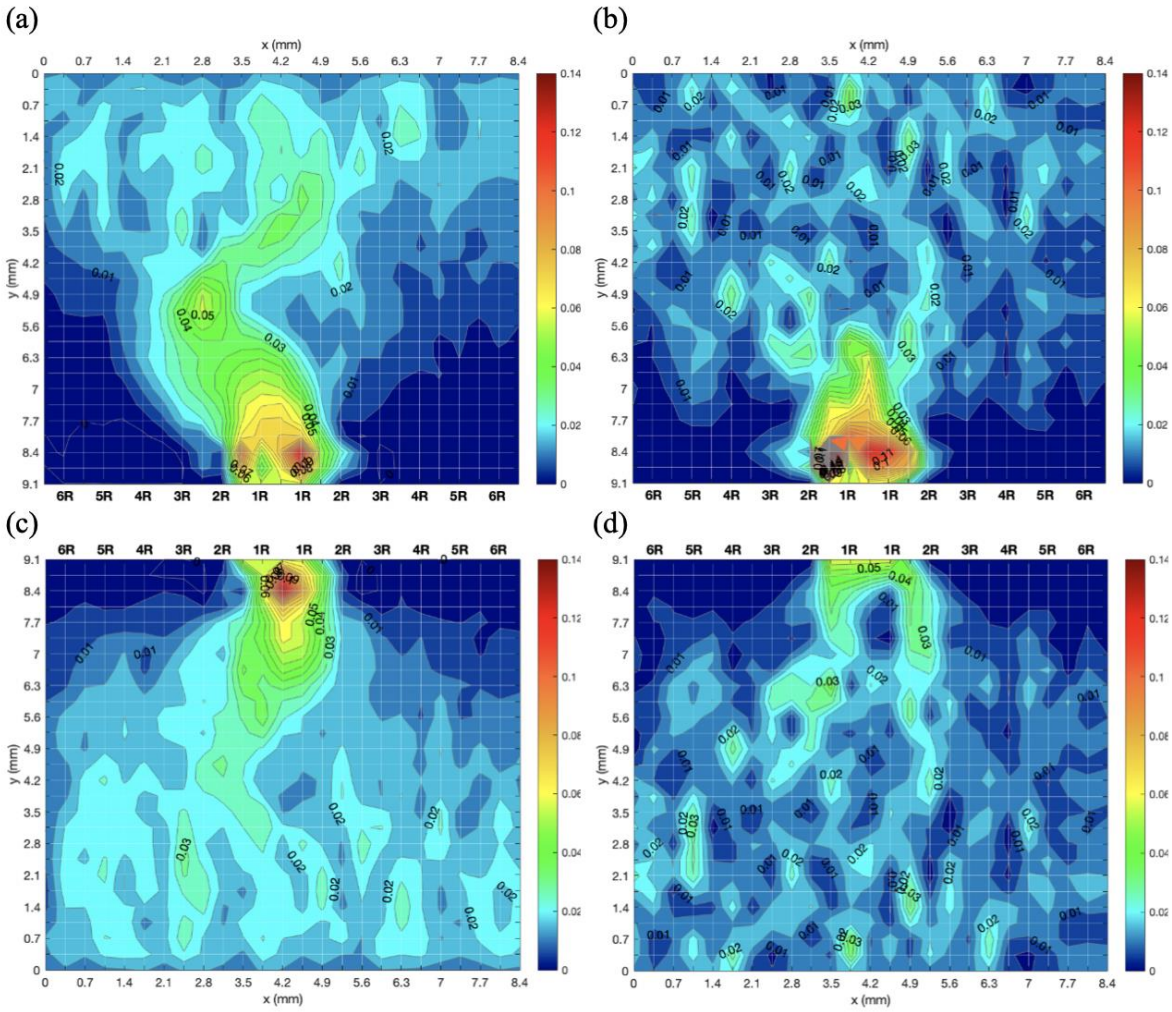

Figure 6. 11. Contours of average oil velocity caused by pressure drawdown at 0.1 sec for upward: (a) Γ=5 J/m^2; (b) Γ=20 J/m^2; and downward perforation cavities: (c) Γ=5 J/m^2; (d) Γ=20 J/m^2

Figures 6.11a, 6.11b, 6.11c and 6.11d depict the average oil velocity contours in porous media as determined by the pressure drawdown at 0.1 sec for Γ=5 and 20 J/m^2 for both upward and downward perforation cavities respectively. It was apparent that the fluid velocity was close to zero in the vicinity of the impermeable IBM casing walls. Bernoulli's effect for an orifice plate occurred adjacent to the perforated well casing, in which the oil velocity increases close to the perforation cavity where it reaches its maximum because of the sharp pressure drop. Resultantly, the associated drag forces applied on the weakened formation cause erosion at the sandface, and sand grains are transported up into the wellbore.

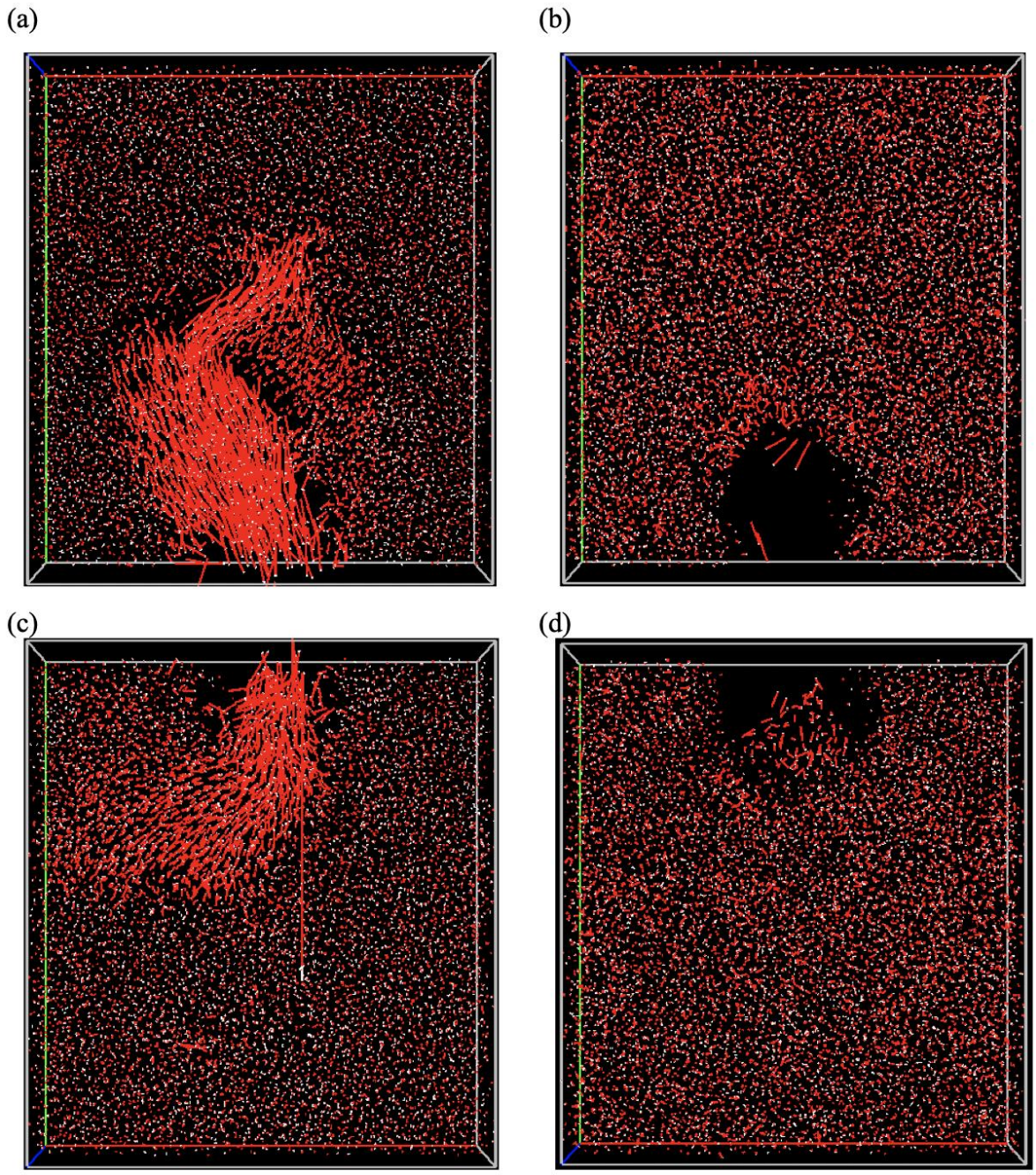

Figure 6. 12. Particle velocity at 0.1 sec for upward: (a) Γ=5 J/m^2; (b) Γ=20 J/m^2; and downward perforation cavities: (c) Γ=5 J/m^2; (d) Γ=20 J/m^2

Figures 6.12a, 6.12b, 6.12c and 6.12d indicate the particle velocity vectors at 0.1 sec for Γ=5 and 20 J/m^2 with both downward and upward gravity directions respectively. Furthermore, maximum particle velocity is shown by long light red vectors, whereas white tick marks show their directions. It was apparent that oil and particle velocity patterns coincided with one another, and it is anticipated that particles having high oil velocity and

maximum velocity vectors in these areas will be exposed to the risk zone in the same way as the mechanical average coordination numbers.

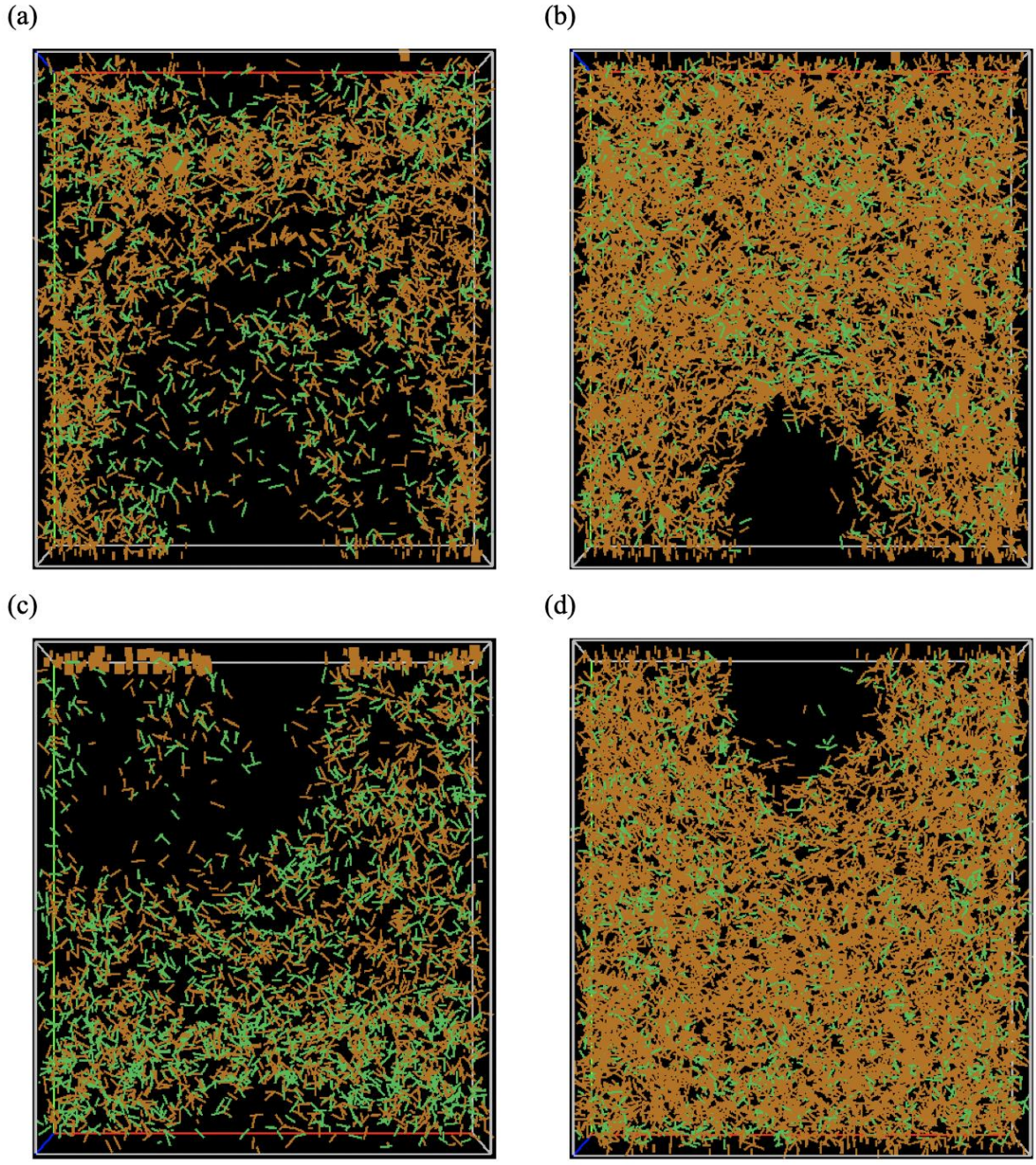

Figure 6. 13. Contact forces (compressive – orange; tensile – mild green) at 0.1 sec for upward: (a) Γ=5 J/m^2; (b) Γ=20 J/m^2; and downward perforation cavities: (c) Γ=5 J/m^2; (d) Γ=20 J/m^2

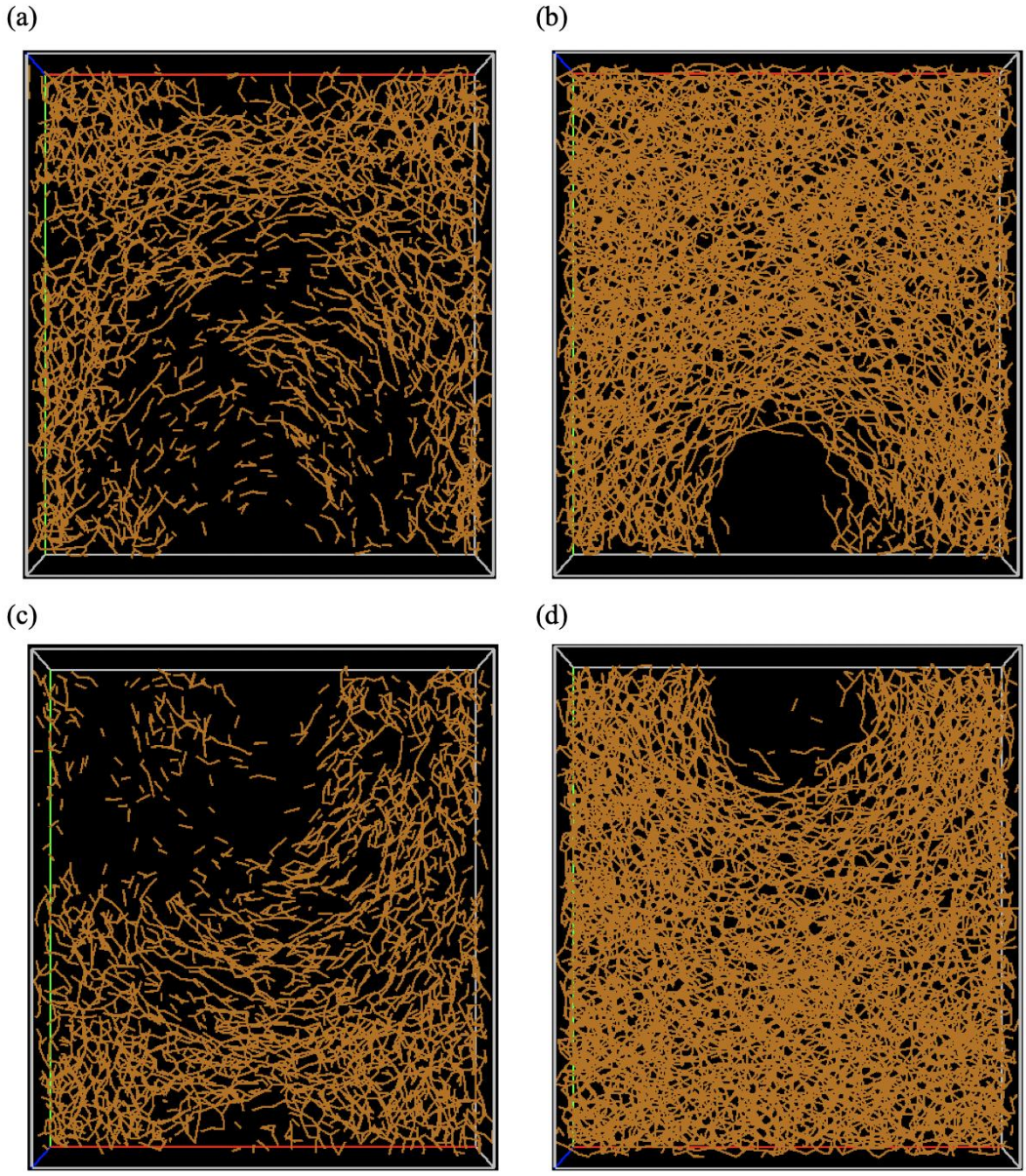

Figure 6. 14. Connection diagram at 0.1 sec for upward: (a) Γ=5 J/m^2; (b) Γ=20 J/m^2; and downward perforation cavities: (c) Γ=5 J/m^2; (d) Γ=20 J/m^2

Figures 6.13a, 6.13b, 6.13c and 6.13d depict the tensile and compressive contact forces. The contact forces are plotted by lines passing through the contact point (lines oriented in the direction of the force). Compressive and tensile forces are identified with orange and mild green colours, respectively. The thickness of each line is proportional to the magnitude of the contact force (scaled to the current maximum force). Information on

contacts and contact forces are provided in Table 6.1 provides the minimum, maximum and average compressive and tensile forces range. Moreover, figures 6.14a, 6.14b, 6.14c 6.14d show the connection diagram at 0.1 sec for Γ=5 and 20 J/m^2 with both downward and upward gravity directions respectively. The connection diagram shows the contacts between the particles, where the centres of the particles involved in these contacts are joined with orange lines. It was apparent that at 0 sec, being the end of perforation stage when the penetrometer was inside the samples, as the bond strength value increased, there was a reduction in the number of sliding and compressive contacts, whereas the tensile contacts increased (Table 6.1). Fewer tensile and compressive contact losses happened at 0.1 sec of sand production in the case of a greater bond strength for both perforation directions, meaning that during the sanding procedure cemented sandstone was more stable. Furthermore, for lower cementation bond strength values, sandstone erosion caused an increase in the size of the perforation cavities.

Table 6. 1. Information on contacts and forces

time, sec	bond strength, J/m^2	perforation direction	max. compressive force, kg·m/s^2	min. tensile force, kg·m/s^2	av. compressive force, kg·m/s^2	av. tensile force, kg·m/s^2	no. of remaining compressive contacts	no. of remaining tensile contacts	no. of remaini sliding contact
0	5	downward	19.98	$-3.39\cdot10^{-3}$	1.28	$-1.59\cdot10^{-3}$	31229	17	30788
0	20	downward	16.96	$-1.69\cdot10^{-2}$	0.78	$-7.17\cdot10^{-3}$	30897	56	30509
0.1	5	upward	$1.05\cdot10^{-2}$	$-4.81\cdot10^{-3}$	$6.59\cdot10^{-4}$	$-2.07\cdot10^{-4}$	3535	1191	4608
0.1	20	upward	$3.97\cdot10^{-2}$	$-2.57\cdot10^{-2}$	$3.47\cdot10^{-3}$	$-1.35\cdot10^{-3}$	10505	1809	12129
0.1	5	downward	$3.14\cdot10^{-3}$	$-2.33\cdot10^{-3}$	$1.40\cdot10^{-4}$	$-4.13\cdot10^{-5}$	2374	1833	4101
0.1	20	downward	$7.01\cdot10^{-2}$	$-2.95\cdot10^{-2}$	$4.24\cdot10^{-3}$	$-1.64\cdot10^{-3}$	11278	1823	12922

6.3.2 Comparison and validation

The comparison of the 3D CFD-DEM-IBM simulations of sand production result with the lab and well data, the CFD-DEM model, and the semi-analytical model data has shown in Figure 6.15. The qualitative comparisons show a similar tendency of decreasing sand production increments from an initial maximum sand rate besides of wide range of geometrical scale, (low) overburden pressure and drawdown, and boundary conditions in these studies. For the comparison of data, the data normalization was adopted from Khamitov et al., 2021 in order to calculate the dimensionless parameters are given below: $\boldsymbol{t_d}$ –

dimensionless time interval, $\boldsymbol{Mcum_d}$ – dimensionless cumulative sand production, and $\boldsymbol{M_d}$ – sand production increments.

$$t_d = \left(\frac{\mathrm{t}}{t_{end}}\right) \tag{6.2}$$

where, t is current time; t_{end} is end time sand production during the hydrocarbon production; $0 < t_d < 1$.

$$Mcum_d^t = \left(\frac{\int_{t=0}^{t} M_t dt}{\int_{t=0}^{t^{end}} M_t dt}\right) \tag{6.3}$$

where $M_t$is instantaneous sand rate and dt is time interval.

The increments in sand production for various rates of sand at different time intervals ($i \in t_d$) are:

$$M_d^i = \left(Mcum_d^i - Mcum_d^{i-1}\right) \tag{6.4}$$

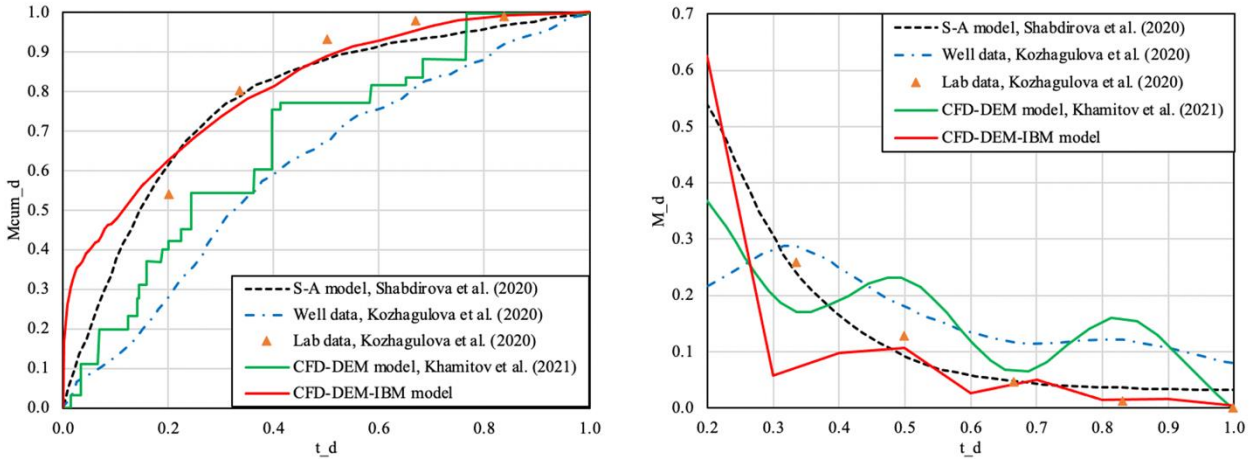

Figure 6. 15. Comparison of the 3D CFD-DEM-IBM simulation results with the laboratory, well, semi-analytical and 3D CFD-DEM model data: a) the dimensionless cumulative sand production; b) the sand production increment (adopted from Khamitov et al., 2021)

6.4 Summary

In this chapter, the CFD-DEM-IBM approach has been used to perform the 3D simulations of sand production in weakly cemented sandstone formations. In all simulations periodic boundaries have been used, where 10000 frictional elastic spheres were generated,

then bonded together and compressed at 1 MPa of overburden pressure (1MPa of overburden pressure is not a real downhole condition, and it was prescribed because of the availability of experimental and analytical results and data for comparison and validation). Sand production simulation geometry and model setup were suggested, where the CPT test was applied in order to examine the sanding mechanism near the physical perforation penetration of the cemented sandstone material. This involved the realistic PSD from the Ustyurt-Buzachi Sedimentary Basin. In order to simulate the fluid flow adjacent to the well casing, the IBM method was modified for the sand production simulation geometry. Oil, having a low density and viscosity was utilised as an injection (reservoir) fluid. This study demonstrated sanding initiations during the first 0.1 sec immediately subsequent to the perforation of the cased horizontal oil well. The pressure drawdown caused erosion in the vicinity of the perforation tunnel. Near the perforation hole, sand particle production was initiated in the course of the first flow as a result of the drag force which lifted the sand particles from the perforation damage area. A sand arch was captured in the area surrounding the perforation tunnel at the commencement of the simulation. However, the fluid flow caused this to collapse, leading to an increase in the size of the perforation cavity. The number and mass of the produced sand particles were computed.

Chapter 7 – Conclusions and recommendations for future work

7.1 3D DEM simulations of triaxial compression tests of cemented sandstone

Three-dimensional DEM simulations of triaxial compression tests have been conducted in periodic cells on medium-dense, medium-loose and loose samples, and material properties of the Ustyurt-Buzachi Sedimentary Basin synthetic samples (experimentally examined by Shabdirova et al., 2016) were recreated for the numerical specimens. Particle rotations were prevented, and 60 simulations were conducted with 5206 frictional elastic spherical particles at various values of bond strength and confining pressure. The findings reveal that peak strength and initial stiffness increase in line with confining pressure, initial density and bond strength; whereas for an initial density and a higher bond strength, the stress attains a peak at a lower axial strain. Although the samples show a higher dilation rate for higher bond strengths, the volumetric dilation decreases as the confining pressure increases. Furthermore, in the case of a higher bond strength for medium-dense, medium-loose and loose systems, there is less occurrence of bond breakage.

The Mohr-Coulomb strength criterion parameters φ' and c' were acquired for medium-dense, medium-loose and loose systems. Moreover, the bond strength and the Mohr-Coulomb shear strength parameters were correlated in order to detect the bond strength values to be compared with the experimental findings. This demonstrated that the numerical samples' stress-strain responses conformed to the experimental results, at least with regard to the shear strength.

When conducting the simulations, it is significant that the usage of a periodic cell enables a homogeneous deformation throughout the test, and that there is no strain localisation. As a result of this, strain softening persists until the attainment of the critical state. Therefore, in principle, the critical state void ratio is a function of the bond strength. Furthermore, higher bond strength values result in higher critical state void ratios, because a greater dilation rate is induced with a high bond strength.

Recommendation for future work: the original result which has been obtained by the author shows that it is possible to calibrate the basic contact interaction model in order to acquire stress-strain curves that conform to the experimental data. Nevertheless, the amount of contraction evident in the laboratory tests cannot be predicted by this basic model. Therefore, it is recommended that in any future work, Shen et al's. (2016) contact interaction model will be applied for the purpose of modelling the cement bonds' crushability and compressibility. Furthermore, high confining stress levels should be used to study the material behavior at actual reservoir conditions (200-500 m depth) since the main limitation of current triaxial simulation works were the low confining stress levels. The confining stress levels 100-1000 kPa were selected because of the availability of experimental data and results for comparison and validation. In the experimental study, the maximum limit of allowable confining stress level in a triaxial apparatus was 700 kPa. Therefore, Shabdirova et al. (2016) conducted the triaxial test at 300 kPa, 500 kPa and 700 kPa and the authors didn't consider a reservoir depth of 200-500m. The developed methods and simulation procedures can be readily used for simulation of real-life cases with a reservoir depth of 200-500 m, but there is no available experimental data of the Ustyurt-Buzachi Sedimentary Basin synthetic samples to validate the results. The assumption was made that the developed contact bond model for cemented sandstone needs to be carefully examined and validated by experimental data before performing the triaxial test simulations with large confining stress levels.

7.2 3D DEM simulations of cone penetration tests in cemented sandstone

The previously developed 3D bond contact model for bonded granular material was applied in this chapter for 3D DEM modelling of CPT test in weakly-cemented sandstone. Realistic PSD and material properties of the Ustyurt-Buzachi Sedimentary Basin synthetic samples were recreated with the numerical samples. The bond strength values that had been found and authenticated with experimental results (Chapter 4) were utilised for the simulations of the CPT test. Moreover, the study was undertaken on the impact of various cementation bond strengths.

According to the results, side friction and cone resistance increase as penetration depths increase. With decrease in bond strength the cone resistance and side friction increase. Bond breakage causes lower bond strength values to have a higher mechanical average coordination number, as well as more contacts (wall-particle and interparticle). This may also result in an increase in cone resistance and side fiction in lightly or weakly-cemented sandstone material.

Furthermore, the number of contacts between particles and penetrometer wall occupies a significant role because a limited number of particles are in contact with the vertical (sleeve) and inclined (cone) walls. Therefore, with increase in particle-wall contact number during the cone penetration process, the vertically acting contact force (f_y) on the cone and side walls may increase.

It has shown that the numerical CPT test results of cemented sandstone conform to the SBT categorisation method from CPT data. The results imply that this technique has the potential to be useful for practising engineers to control the cone penetration test within the sandstone field.

7.3 3D CFD-DEM-IBM simulations of sand production in oil wells

This research extends the 3D DEM simulations of cone penetration within cemented sandstone (Chapter 5). This involved realistic PSD and material properties of the Ustyurt-Buzachi Sedimentary Basin synthetic samples. Previously, numerically penetrated sandstone samples having a bond strength of Γ=5 and 20 J/m^2 were utilised in order to conduct the numerical simulation of sand production in horizontally cased wells. This study applied the 3D CFD-DEM-IBM coupled modelling technique, in which the IBM part was modified and optimized for numerical sample geometry. The computational cost resulted only in the first 0.1 sec of sanding initiation having 10000 frictional elastic spherical particles to be addressed. Sanding mechanisms due to the pressure drawdown was examined. In this study, the fluid (oil) flows were driven by the differences between the top and base boundary pressures of the workspace, and also lifted the eroded sand particles. The findings revealed that all of the produced sand particles emanated from the perforation damaged area.

Rahmati et al. (2013) indicated the necessity for capturing sand arching requiring complicated interactions between the geometry of the opening in the completion and the disaggregated rock mass attributes under prevailing state of stress. A sand arch was numerically captured in the study, and the arch collapse caused the perforation cavity to become larger. For the first time it has been shown that the suggested sample preparation and IBM techniques with complicated boundaries under overburden pressure and pressure drawdown are appropriate for capturing the sand arches. The mass and amount of produced sand particles were calculated for the four samples at various bond strength values as well as vertically upward and downward perforation cavities. In the case of the bond strength being higher, the samples produced fewer sand particles and the sand arches became more stable.

The aim of the current research was limited only with development of a new complex sand production simulation geometry and procedures with a physical perforation penetration and immersed complex boundaries using the 3D CFD-DEM-IBM modelling and to show the capability of the current modelling approach to study the sanding mechanism at micro and macro scales, capturing of sand arch. It should be noted that 1 MPa of overburden pressure is very low for the simulations of sand production problem. This work does not support that the obtained results are applicable too high depth and high confining stress faced in actual conditions. The 1Mpa overburden pressure is prescribed because of the availability of experimental and analytical results and data for comparison and validation. The methods developed can be readily used for simulation of real life cases with very large overburden pressures, but there is no available experimental data to validate the results. The assumption was made that the developed contact bond model for cemented sandstone needs to be carefully examined and validated by experimental data before performing the simulations of perforation penetration and sand production with large overburden pressures.

Another limitation of the current simulations is that due to time constraints, plane strain and quasi-3D simulations of cone penetration and sand production were performed. Fully 3D simulations of cone penetration and sand production tests in cemented sandstone with real-world PSD are excessively time consuming.

Recommendation for future work: For any future simulations it would be worthwhile to use large numerical specimens with several hundred thousand or million particles compressed at high overburden pressure in order to mimic the real downhole conditions; and to investigate quantitative comparisons and validations of the obtained results with real field

or experimental data. Furthermore, it will be interesting to see what occurs during the initial 1-10 seconds of sanding initiation immediately subsequent to the perforation penetration in oil wells.

The perforation may be carried out in four conditions based on the pressure difference between reservoir and wellbore: underbalanced - wellbore pressure is lower than reservoir pressure; balanced - wellbore and reservoir pressure are equal; overbalanced - wellbore pressure is greater than reservoir pressure; and extreme overbalanced - wellbore pressure greatly exceed rock strength and reservoir pressure (Behrmann et al., 2000).

This research has performed the simulation of the physical perforation penetration and the first flow immediately after the perforation under pressure drawdown (the reservoir pressure was higher than wellbore pressure). This case can 'mimic' the underbalanced perforation and first flow after it. Behrmann et al., 2000 reported that in underbalanced conditions, there is instant decompression of reservoir fluids around a perforation immediately after perforating. The dynamic forces (drag and pressure drawdown) that reduce permeability damage by eroding and washing/lifting fractured formation grains from perforation cavity walls are highest at this time. Furthermore, the underbalanced condition is required to effectively clean-up of crushed-zone damage (Behrmann et al., 1991).

It will be interesting to extend this research by investigation the perforation penetration and sand production simulations under different pressure drawdowns (to mimic the balanced, overbalanced and extreme overbalanced conditions), and to study the sandstone formation behaviour and its sanding mechanism of near the perforation cavity.

Bibliography

Acar, Y. B., & El-Tahir, E. T. A. (1986). Low strain dynamic properties of artificially cemented sand. *Journal of Geotechnical Engineering*, *112*(11), 1001-1015.

Agada, S., Chen, F., Geiger, S., Toigulova, G., Agar, S., Shekhar, R., ... & Immenhauser, A. (2014). Numerical simulation of fluid-flow processes in a 3D high-resolution carbonate reservoir analogue.

Airey, D. W. (1993). Triaxial testing of naturally cemented carbonate soil. Journal of Geotechnical Engineering, 119(9), 1379-1398.

Al-Awad, M. N. (2001). The mechanism of sand production caused by pore pressure fluctuations. Oil & Gas Science and Technology, 56(4), 339-345.

Al-Shaaibi, S. K., Al-Ajmi, A. M., & Al-Wahaibi, Y. (2013). Three dimensional modeling for predicting sand production. Journal of Petroleum Science and Engineering, 109, 348-363.

Alvarado, G., Coop, M. R., & Willson, S. (2012). On the role of bond breakage due to unloading in the behaviour of weak sandstones. Géotechnique, 62(4), 303-316.

Anderson, T. B., & Jackson, R. (1967). Fluid mechanical description of fluidized beds. Equations of motion. Industrial & Engineering Chemistry Fundamentals, 6(4), 527-539.

Arroyo, M., Butlanska, J., Gens, A., Calvetti, F., & Jamiolkowski, M. (2011). Cone penetration tests in a virtual calibration chamber. Géotechnique, 61(6), 525-531.

Balgobin, C. J. (2005, January). Sand management of ultra-high-rate gas wells. In SPE Latin American and Caribbean Petroleum Engineering Conference. Society of Petroleum Engineers.

Baxter, D., Behrmann, L. A., Grove, B., Williams, H., Heiland, J., Hong, L. J., ... & Suppiah, R. R. (2009). Perforating–when failure is the objective. Oilfield Review, 21(3), 4-17.

Behrmann, L., Brooks, J. E., Farrant, S., Fayard, A., Venkitaraman, A., Brown, A., ... & Underdown, D. (2000). Perforating practices that optimize productivity. Oilfield Review, 12(1), 52-74.

Behrmann, L. A., Pucknell, J. K., Bishop, S. R., & Hsia, T. Y. (1991, January). Measurement of Additional Skin Resulting From Perforation Damage. In SPE Annual Technical Conference and Exhibition. Society of Petroleum Engineers.

Bird, R. B., Stewart, W. E., & Lightfoot, E. N. (1960). Transport Phenomena John Wiley & Sons. New York, 413.

Bjorlykke, K. (2010). Petroleum geoscience: From sedimentary environments to rock physics. Springer Science & Business Media.

Bradford, I. D. R., & Cook, J. M. (1994, January). A semi-analytic elastoplastic model for wellbore stability with applications to sanding. In Rock mechanics in petroleum engineering. Society of Petroleum Engineers.

Bratli, R. K., & Risnes, R. (1981). Stability and failure of sand arches. Society of Petroleum Engineers Journal, 21(02), 236-248.

Butlanska, J. (2014). Cone penetration test in a virtual calibration chamber. Ph.D. Thesis. Universitat Politècnica de Catalunya.

Butlanska, J., Arroyo, M., & Gens, A. (2010). Virtual calibration chamber cpt on ticino sand. In 2nd International Symposium on Cone Penetration Testing, Huntington Beach, CA, USA.

Butlanska, J., Arroyo, M., Gens, A., & O'Sullivan, C. (2014). Multi-scale analysis of cone penetration test (CPT) in a virtual calibration chamber. Canadian geotechnical journal, 51(1), 51-66.

Calvetti, F., & Nova, R. (2004). Micromechanical approach to slope stability analysis. In Degradations and instabilities in geomaterials (pp. 235-254). Springer, Vienna.

Campanella, R. G., & Robertson, P. K. (1982). *State-of-the-art in in-situ testing of soils; developments since 1978*. In Engineering Foundation Conference on Updating Subsurface Sampling of Soils and Rocks and Their In-Situ Testing, Santa Barbara, CA, USA.

Carlson, J., Gurley, D., King, G., Price-Smith, C., & Waters, F. (1992). Sand control: why and how. Oilfield Review, 4(4), 41-53.

Cavarretta, I., O'Sullivan, C., & Coop, M. R. (2009, June). Applying 2D shape analysis techniques to granular materials with 3D particle geometries. In AIP Conference Proceedings (Vol. 1145, No. 1, pp. 833-836). American Institute of Physics.

Cheung, L. Y. G. (2010). Micromechanics of sand production in oil wells (Doctoral dissertation, Imperial College London).

Ciantia, M. O., Arroyo, M., Butlanska, J., & Gens, A. (2016). DEM modelling of cone penetration tests in a double-porosity crushable granular material. Computers and Geotechnics, 73, 109-127.

Clough, G. W., Sitar, N., Bachus, R. C., & Rad, N. S. (1981). Cemented sands under static loading. Journal of Geotechnical and Geoenvironmental engineering, 107(ASCE 16319 Proceeding).

Collective industry effort. (2013). Kazakhstan upstream oil and gas technology and R&D roadmap, Kazakhstan.

Collins, B. D., & Sitar, N. (2011). Stability of steep slopes in cemented sands. Journal of geotechnical and geoenvironmental engineering, 137(1), 43-51.

Coop, M. R., & Atkinson, J. H. (1993). The mechanics of cemented carbonate sands. Geotechnique, 43(1), 53-67.

Coop, M. R., & Willson, S. M. (2003). Behavior of hydrocarbon reservoir sands and sandstones. Journal of Geotechnical and Geoenvironmental Engineering, 129(11), 1010-1019.

Crook, T., Willson, S., Yu, J. G., & Owen, R. (2003). Computational modelling of the localized deformation associated with borehole breakout in quasi-brittle materials. Journal of Petroleum Science and Engineering, 38(3-4), 177-186.

Cuccovillo, T., & Coop, M. R. (1999). On the mechanics of structured sands. Géotechnique, 49(6), 741-760.

Cui, Y., Nouri, A., Chan, D., & Rahmati, E. (2016). A new approach to DEM simulation of sand production. Journal of Petroleum Science and Engineering, 147, 56-67.

Cundall, P. A., & Strack, O. D. (1979). A discrete numerical model for granular assemblies. geotechnique, 29(1), 47-65.

Da Cruz, F., Emam, S., Prochnow, M., Roux, J. N., & Chevoir, F. (2005). Rheophysics of dense granular materials: Discrete simulation of plane shear flows. Physical Review E, 72(2), 021309.

Dawe, R. A. (2004). Miscible Displacement in heterogeneous porous Media. In The Sixth Caribbean Congress of Fluid Dynamics.

Detournay, C. (2009). Numerical modeling of the slit mode of cavity evolution associated with sand production. SPE Journal, 14(04), 797-804.

Detournay, C., Tan, C., & Wu, B. (2006). Modeling the mechanism and rate of sand production using FLAC.

Di Felice, R. (1994). The voidage function for fluid-particle interaction systems. International journal of multiphase flow, 20(1), 153-159.

Dresen, G., Stanchits, S., & Rybacki, E. (2010). Borehole breakout evolution through acoustic emission location analysis. International Journal of Rock Mechanics & Mining Sciences, 47, 426-435.

Druzin R. (2018, Sept 28). Fight over to site oilfield waste landfill pits tiny South Texas town against major corporation (available at houstonchronicle.com).

Dupas, J. M., & Pecker, A. (1979). Static and dynamic properties of sand-cement. Journal of the Geotechnical Engineering Division, 105(3), 419-436.

Fattahpour, V., Moosavi, M., & Mehranpour, M. (2012). An experimental investigation on the effect of rock strength and perforation size on sand production. Journal of Petroleum Science and Engineering, 86, 172-189.

Geilikman, M. B., & Dusseault, M. B. (1997). Fluid rate enhancement from massive sand production in heavy-oil reservoirs. Journal of Petroleum Science and Engineering, 17, 5-18.

Guo, Y., Wu, C. Y., & Thornton, C. (2013). Modeling gas-particle two-phase flows with complex and moving boundaries using DEM-CFD with an immersed boundary method. AIChE Journal, 59(4), 1075-1087.

Gutierrez, G. A. (2007). Influence of late cementation on the behaviour of reservoir sands (Doctoral dissertation, Department of Civil and Environmental Engineering, Imperial College London).

Hall Jr, C. D., & Harrisberger, W. H. (1970). Stability of sand arches: a key to sand control. Journal of Petroleum Technology, 22(07), 821-829.

Han, Y., & Cundall, P. A. (2011). Lattice Boltzmann modeling of pore-scale fluid flow through idealized porous media. International Journal for Numerical Methods in Fluids, 67(11), 1720-1734.

Hayavi, M. T., & Abdideh, M. (2017). Establishment of tensile failure induced sanding onset prediction model for cased-perforated gas wells. Journal of Rock Mechanics and Geotechnical Engineering, 9(2), 260-266.

Hertz, H. (1882). Ueber die Berührung fester elastischer Körper. Journal für die reine und angewandte Mathematik, 1882(92), 156-171.

Hezmi, M. A., Wheeler, S., & Gallipoli, D. (2009). On the preparation of soil samples with variable degrees of bonding. Unsaturated Soils, Two Volume Set: Experimental Studies in Unsaturated Soils and Expansive Soils (Vol. 1) & Theoretical and Numerical Advances in Unsaturated Soil Mechanics (Vol. 2), 2, 21.

Holt, R. M., & Kenter, C. J. (1992, January). Laboratory simulation of core damage induced by stress release. In The 33rd US Symposium on Rock Mechanics (USRMS). American Rock Mechanics Association.

Holt, R. M., Unander, T. E., & Kenter, C. J. (1993, December). Constitutive mechanical behaviour of synthetic sandstone formed under stress. In International journal of rock mechanics and mining sciences & geomechanics abstracts (Vol. 30, No. 7, pp. 719-722). Pergamon.

Huang, A. B., & Ma, M. Y. (1994). An analytical study of cone penetration tests in granular material. Canadian Geotechnical Journal, 31(1), 91-103.

Huang, J. T., & Airey, D. W. (1998). Properties of artificially cemented carbonate sand. Journal of Geotechnical and Geoenvironmental Engineering, 124(6), 492-499.

Ispas, I., McLennan, J., & Martin, W. (2006). Interim report on perforation testing for improved sand management. Technical report, BP and ASRC Energy Services and TerraTek.

Issa, R. I. (1986). Solution of the implicitly discretised fluid flow equations by operator-splitting. *Journal of computational physics*, *62*(1), 40-65.

Iversen, M., Broome, J. T., Mohamed, O. Y., & Ratterman, E. E. (2006, January). Next Generation of Mulitpath Screens Solves Deepwater Completion Challenges. In SPE International Symposium and Exhibition on Formation Damage Control. Society of Petroleum Engineers.

Jensen, R. P., & Preece, D. S. (2000). Modeling sand production with Darcy-flow coupled with discrete elements (No. SAND2000-2036C). Sandia National Labs., Albuquerque, NM (US); Sandia National Labs., Livermore, CA (US).

Jiang, M. J., Yu, H. S., & Harris, D. (2006). Discrete element modelling of deep penetration in granular soils. International journal for numerical and analytical methods in geomechanics, 30(4), 335-361.

Jiang, M., Dai, Y., Cui, L., Shen, Z., & Wang, X. (2014). Investigating mechanism of inclined CPT in granular ground using DEM. Granular Matter, 16(5), 785-796.

Jiang, M., Liu, F., Wang, H., & Wang, X. (2015). Investigation of the effect of different gravity conditions on penetration mechanisms by the Distinct Element Method. Engineering Computations.

Jin, Y., Chen, K. P., & Chen, M. (2011). Development of tensile stress near a wellbore in radial porous media flows of a high pressure gas. International Journal of Rock Mechanics and Mining Sciences, 48(8), 1313-1319.

Jing, L., & Stephansson, O. (2007). Fundamentals of discrete element methods for rock engineering: theory and applications. Elsevier.

Johnson, K. L. (1977). Adhesion at the contact of solids. Theoretical and applied mechanics, 133-143.

Johnson, K. L., Kendall, K., & Roberts, A. (1971). Surface energy and the contact of elastic solids. Proceedings of the royal society of London. A. mathematical and physical sciences, 324(1558), 301-313.

Jung, J.W., Santamarina, J.C., Soga, K. (2012). Stress-strain response of hydrate-bearing sands: numerical study using discrete element method simulations. Journal of Geophysical research 117: 1-12.

Kabir, M. E., Song, B., Martin, B. E., & Chen, W. (2010). Compressive behavior of fine sand. Sandia National Laboratories, New Mexico.

Kafui, K. D., Thornton, C., & Adams, M. J. (2002). Discrete particle-continuum fluid modelling of gas–solid fluidised beds. Chemical Engineering Science, 57(13), 2395-2410.

Kafui, D. K., Johnson, S., Thornton, C., & Seville, J. P. K. (2011). Parallelization of a Lagrangian–Eulerian DEM/CFD code for application to fluidized beds. Powder Technology, 207(1-3), 270-278.

Kajishima, T., Takiguchi, S., Hamasaki, H., & Miyake, Y. (2001). Turbulence structure of particle-laden flow in a vertical plane channel due to vortex shedding. JSME International Journal Series B Fluids and Thermal Engineering, 44(4), 526-535.

Khosravi, A., Martinez, A., & DeJong, J. T. (2020). Discrete element model (DEM) simulations of cone penetration test (CPT) measurements and soil classification. Canadian Geotechnical Journal, 57(9), 1369-1387.

Kim, S. H., Sharma, M. M., & Fitzpatrick, H. J. (2011, November). A Predictive model for sand production in poorly consolidated sands. In International Petroleum Technology Conference. OnePetro.

King, G. E., Wildt, P. J., & O'Connell, E. (2003, January). Sand control completion reliability and failure rate comparison with a multi-thousand well database. In SPE Annual Technical Conference and Exhibition. Society of Petroleum Engineers.

Kuipers, J. A. M., Van Duin, K. J., Van Beckum, F. P. H., & van Swaaij, W. P. M. (1993). Computer simulation of the hydrodynamics of a two-dimensional gas-fluidized bed. Computers & chemical engineering, 17(8), 839-858.

Lade, P. V., & Overton, D. D. (1989). Cementation effects in frictional materials. Journal of Geotechnical Engineering, 115(10), 1373-1387.

Lantz, J. R., & Ali, N. (1991). Development of a mature giant offshore oil field. Journal of Petroleum Technology, 43(04), 392-454.

Leroueil, S., & Vaughan, P. R. (1990). The general and congruent effects of structure in natural soils and weak rocks. Géotechnique, 40(3), 467-488.

Li, L., & Holt, R. M. (2002). Particle scale reservoir mechanics. Oil & Gas Science and Technology, 57(5), 525-538.

Li, L., Papamichos, E., & Cerasi, P. (2006). Investigation of sand production mechanisms using DEM with fluid flow. Multiphysics Coupling and Long Term Behaviour in Rock Mechanics, 1, 241-247.

Maccarini, M. (1987). Laboratory studies for a weakly bonded artificial soil. PhD Thesis, University of London.

MacCormack, R. W. (1971). Numerical solution of the interaction of a shock wave with a laminar boundary layer. In Proceedings of the second international conference on numerical methods in fluid dynamics (pp. 151-163). Springer, Berlin, Heidelberg.

Mahmud, H. B., Leong, V. H., & Lestariono, Y. (2020). Sand production: A smart control framework for risk mitigation. Petroleum, 6(1), 1-13.

Miller, G. F., Pursey, H., & Bullard, E. C. (1955). On the partition of energy between elastic waves in a semi-infinite solid. Proceedings of the Royal Society of London. Series A. Mathematical and Physical Sciences, 233(1192), 55-69.

Mindlin, R. D. (1949). Compliance of elastic bodies in contact. J. Appl. Mech., ASME, 16, 259-268.

Morad, S., & Worden, R. H. (Eds.). (2003). Clay mineral cements in sandstones. Blackwell Publishing.

Morgan, N. (2006). Saving sand dollars, Frontiers: 6, August.

Morita, N., Whitfill, D. L., Fedde, O. P., & Lovik, T. H. (1989a). Parametric study of sand production prediction: analyticl approach. SPE Production Engineering, 4(1), 25- 33.

Morita, N., Whitfill, D. L., Masssie, I., & Knudsen, T. W. (1989b). Realistic sand production prediction numerical approach. SPE Production Engineering, 4(1), 15-24.

Mühlhaus, H. B., & Vardoulakis, I. (1987). The thickness of shear bands in granular materials. Geotechnique, 37(3), 271-283.

Musa, L. A., Temisanren, T., & Appah, D. (2005, January). Establishing Actual Quantity of Sand Using an Ultrasonic Sand Detector; The Niger Delta Experience. In Nigeria Annual International Conference and Exhibition. Society of Petroleum Engineers.

Nicholson, E. D., Goldsmith, G., & Cook, J. M. (1998, July). Direct observation and modeling of sand production processes in weak sandstone. In SPE/ISRM Rock Mechanics in Petroleum Engineering. OnePetro.

Nouri, A., Kuru, E., & Vaziri, H. (2007, January). Enhanced modelling of sand production through improved deformation and stress analysis. In Canadian International Petroleum Conference. Petroleum Society of Canada.

Nouri, A., Kuru, E., & Vaziri, H. (2009). Elastoplastic modelling of sand production using fracture energy regularization method. Journal of Canadian Petroleum Technology, 48(04), 64-71.

Nouri, A., Vaziri, H., Belhaj, H. & Islam, R. (2004). Sand production prediction: a new set of criteria for modeling based on large-scale transient experiments and numerical investigation. 2004 SPE Annual Technical Conference and Exhibition. Houston, US. SPE 90273.

Nouri, A., Vaziri, H., Belhaj, H., & Islam, R. (2004, January). Sand production prediction: a new set of criteria for modeling based on large-scale transient experiments and numerical investigation. In SPE Annual Technical Conference and Exhibition. Society of Petroleum Engineers.

Nouri, A., Vaziri, H., Kuru, E., & Islam, R. (2006). A comparison of two sanding criteria in physical and numerical modeling of sand production. Journal of petroleum science and engineering, 50, 55-70.

O'Connor, R.I.M., Torczynski, J.R., Preece, D.S., Klosek, J.T., Williams, J.R. (1997). Discrete element modeling of sand production. International Journal of Rock Mechanics and Mining Sciences, 34(3), 373-373.

Obermayr, M., Dressler, K., Vrettos, C., & Eberhard, P. (2013). A bonded-particle model for cemented sand. Computers and Geotechnics, 49, 299-313.

Ong, S., Ramos, R., & Zheng, Z. (2000, January). Sand production prediction in high rate, perforated and open-hole gas wells. In SPE International Symposium on Formation Damage Control. Society of Petroleum Engineers.

Palmer, I., Vaziri, H., Willson, S., Moschovidis, Z., Cameron, J., & Ispas, I. (2003, January). Predicting and managing sand production: A new strategy. In SPE Annual Technical Conference and Exhibition. Society of Petroleum Engineers.

Papamichos, E. (2006). Sand production: Physical and experimental evidence. Special issue of Revue européenne de génie civil, 10(6-7), 803-816.

Papamichos, E., & Furui, K. (2013, January). Sand production initiation criteria and their validation. In 47th US rock mechanics/geomechanics symposium. American Rock Mechanics Association.

Papamichos, E., & Stavropoulou, M. (1998). An erosion-mechanical model for sand production rate prediction. International Journal of Rock Mechanics and Mining Sciences, 4(35), 531-532.

Papamichos, E., & Vardoulakis, I. (2005). Sand erosion with a porosity diffusion law. Computers and Geotechnics, 32(1), 47-58.

Papamichos, E., Skjærstein, A., & Tronvoll, J. (2000, January). A volumetric sand production experiment. In 4th North American Rock Mechanics Symposium. American Rock Mechanics Association.

Papamichos, E., Tronvoll, J., Skjærstein, A., & Unander, T. E. (2010). Hole stability of Red Wildmoor sandstone under anisotropic stresses and sand production criterion. Journal of Petroleum Science and Engineering, 72(1-2), 78-92.

Papamichos, E., Vardoulakis, I., Tronvoll, J., & Skjaerstein, A. (2001). Volumetric sand production model and experiment. International journal for numerical and analytical methods in geomechanics, 25(8), 789-808.

Papanastasiou, P. C., & Vardoulakis, I. G. (1992). Numerical treatment of progressive localization in relation to borehole stability. International Journal for Numerical and Analytical Methods in Geomechanics, 16(6), 389-424.

Patankar, S. V. (1980). Numerical heat transfer and fluid flow, Hemisphere Publ. Corp., New York, 58.

Penberthy, W. L., & Shaughnessy, C. M. (1992). Sand control. Henry L. Doherty Memorial Fund of AIME, Society of Petroleum Engineers.

Pera, N. C. (2017). A coupled CFD-DEM model for sand production in oil wells (Doctoral dissertation, Universitat Politècnica de Catalunya).

Peskin, C. S. (1973). Flow patterns around heart valves: a digital computer method for solving the equations of motion. IEEE Transactions on Biomedical Engineering, (4), 316-317.

Potyondy, D. O., & Cundall, P. A. (2004). A bonded-particle model for rock. International journal of rock mechanics and mining sciences, 41(8), 1329-1364.

Price-Smith, C., Parlar, M., Bennett, C., Gilchrist, J. M., Pitoni, E., Burton, R. C., ... & Dickerson, R. (2003). Design methodology for selection of horizontal openhole sand-control completions supported by field case histories. SPE drilling & completion, 18(03), 235-255.

Rahman, Z., Toll, D. G., Gallipoli, D., & Taha, M. R. (2010). Micro-structure and engineering behaviour of weakly bonded soil. Sains Malaysiana, 39(6), 989-997.

Rahmati, H., Jafarpour, M., Azadbakht, S., Nouri, A., Vaziri, H., Chan, D., & Xiao, Y. (2013). Review of sand production prediction models. Journal of Petroleum Engineering, 2013.

Rahmati, H., Nouri, A., Vaziri, H., & Chan, D. (2012). Validation of predicted cumulative sand and sand rate against physical-model test. Journal of Canadian Petroleum Technology, 51(05), 403-410.

Rawlins, C. H. (2013, April). Sand management methodologies for sustained facilities operations. In North Africa Technical Conference and Exhibition. Society of Petroleum Engineers.

Rawlins, C. H., Staten, S. E., & Wang, I. I. (2000, January). Design and installation of a sand separation and handling system for a Gulf of Mexico oil production facility. In SPE Annual Technical Conference and Exhibition. Society of Petroleum Engineers.

Rios, S., Da Fonseca, A. V., & Baudet, B. A. (2014). On the shearing behaviour of an artificially cemented soil. Acta Geotechnica, 9(2), 215-226.

Risnes, R., Bratli, R. K., & Horsrud, P. (1982). Sand stresses around a wellbore. Society of Petroleum Engineers Journal, 22(06), 883-898.

Robertson, P. K. (1990). Soil classification using the cone penetration test. Canadian Geotechnical Journal, 27(1), 151-158.

Robertson, P. K., Campanella, R. G., Gillespie, D., & Greig, J. (1986, June). Use of piezometer cone data. In Use of in situ tests in geotechnical engineering (pp. 1263-1280). ASCE.

Satake, M. (1982). Fabric tensor in granular materials. In: Vermeer, P.A., Luger, H.J. (eds.) Deformation and Failure of Granular Materials, pp. 63–68. Balkema, Rotterdam.

Schnaid, F., Prietto, P. D., & Consoli, N. C. (2001). Characterization of cemented sand in triaxial compression. Journal of geotechnical and geoenvironmental engineering, 127(10), 857-868.

Selfridge, F., Munday, M., Kvernvold, O., & Gordon, B. (2003, January). Safely improving production performance through improved sand management. In SPE Offshore Europe Oil and Gas Exhibition and Conference. Society of Petroleum Engineers.

Shabdirova, A. D., Bissekenova, Z., Minh, N. H., & Kim, J. R. (2016, June). Sample preparation method of clay-rich sandstone analogue of sandstone reservoirs in kazakhstan. In 50th US Rock Mechanics/Geomechanics Symposium. American Rock Mechanics Association.

Shen, Z., & Jiang, M. (2016). DEM simulation of bonded granular material. Part II: extension to grain-coating type methane hydrate bearing sand. Computers and Geotechnics, 75, 225-243.

Shen, Z., Jiang, M., & Thornton, C. (2016). DEM simulation of bonded granular material. Part I: contact model and application to cemented sand. Computers and Geotechnics, 75, 192-209.

Stein, M. H., Colbert, J. R., Asher, G. B., Vaziri, H. H., Chitale, A. A., Gonzalez, F. A., & Sun, Y. (2005, January). Integrated Sand and Erosion Alarming on NaKika, Deepwater Gulf of Mexico. In SPE Annual Technical Conference and Exhibition. Society of Petroleum Engineers.

Tashliyev, M.S., & Tovbina, C.Z. (1992). Paleogeografia zapada Srednei Azii v melovoi period [Paleogeography of west Middle Asia in Creteaceous]. Saint Petersburg: Nedra.

Terzaghi, K. (1936). Stress distribution in dry and in saturated sand above a yielding trapdoor.

Thornton, C. (2000). Numerical simulations of deviatoric shear deformation of granular media. Géotechnique, 50(1), 43-53.

Thornton, C. (2015). Granular dynamics contact mechanics and particle system simulations. A DEM study. Particle Technology Series, 24., Springer.

Tiffin, D. L., Stein, M. H., & Wang, X. (2003, January). Drawdown guidelines for sand control completions. In SPE Annual Technical Conference and Exhibition. Society of Petroleum Engineers.

Tixier, M. P., Loveless, G. W., & Anderson, R. A. (1975). Estimation of formation strength from the mechanical-properties log (incudes associated paper 6400). Journal of Petroleum Technology, 27(03), 283-293.

Tronvoll, J., Fjaer, E., Kessler, N., Santarelli, F. J., & Morita, N. (1993). The effect of anisotropic stress state on the stability of perforation cavities. International Journal of Rock Mechanics and Mining Sciences and Geomechanics Abstracts;(United Kingdom), 30(7).

Tronvoll, J., Skj, A., & Papamichos, E. (1997). Sand production: mechanical failure or hydrodynamic erosion? International Journal of Rock Mechanics and Mining Sciences, 34(3-4), 291-e1.

Tsuji, Y., Kawaguchi, T., & Tanaka, T. (1993). Discrete particle simulation of two-dimensional fluidized bed. Powder technology, 77(1), 79-87.

USGS Open-File Report 2006-1195. (available at https://pubs.usgs.gov/of/2006/1195/htmldocs/imag es/chart.pdf)

Utili, S., & Nova, R. (2008). DEM analysis of bonded granular geomaterials. International Journal for Numerical and Analytical Methods in Geomechanics, 32(17), 1997-2031.

Van den Hoek, P. J., Hertogh, G. M. M., Kooijman, A. P., De Bree, P., Kenter, C. J., & Papamichos, E. (2000). A new concept of sand production prediction: theory and laboratory experiments. SPE Drilling & Completion, 15(04), 261-273.

Van den Hoek, P. J., Kooijman, A. P., De Bree, P., Kenter, C. J., Zheng, Z., & Khodaverdian, M. (2000). Horizontal-wellbore stability and sand production in weakly consolidated sandstones. SPE Drilling & Completion, 15(04), 274-283.

Vardoulakis, I., Stavropoulou, M., & Papanastasiou, P. (1996). Hydro-mechanical aspects of the sand production problem. Transport in Porous Media, 22, 225-244.

Vaziri, H. H., Allam, R. D., Kidd, G. A., Bennett, C. L., Grose, T. D., Robinson, P. A., & Malyn, J. (2006). Sanding: A rigorous examination of the interplay between drawdown, depletion, start-up frequency and water cut. SPE Production & Operations, 21(04), 430-440.

Vaziri, H. H., Nouri, A., Hovem, K. A., & Wang, X. (2007, January). Computation of sand production in water injectors. In European Formation Damage Conference. Society of Petroleum Engineers.

Vaziri, H., Barree, B., Xiao, Y., Palmer, I., & Kutas, M. (2002, September). What is the magic of water in producing sand? In SPE Annual Technical Conference and Exhibition. OnePetro.

Veeken, C. A. M., Davies, D. R., Kenter, C. J., & Kooijman, A. P. (1991, January). Sand production prediction review: developing an integrated approach. In SPE annual technical conference and exhibition. Society of Petroleum Engineers.

Walton, K. (1987). The effective elastic moduli of a random packing of spheres. Journal of the Mechanics and Physics of Solids, 35(2), 213-226.

Wang, J., Yale, D. P., & Dasari, G. R. (2011, January). Numerical modeling of massive sand production. In SPE Annual Technical Conference and Exhibition. Society of Petroleum Engineers.

Wang, Y. H., & Leung, S. C. (2008). A particulate-scale investigation of cemented sand behavior. Canadian Geotechnical Journal, 45(1), 29-44.

Wang, Y. H., & Leung, S. C. (2008). Characterization of cemented sand by experimental and numerical investigations. Journal of geotechnical and geoenvironmental engineering, 134(7), 992-1004.

Wang, Y., & Wu, B. (2001, January). Borehole collapse and sand production evaluation: Experimental testing, analytical solutions and field implications. In DC Rocks 2001, The 38th US Symposium on Rock Mechanics (USRMS). American Rock Mechanics Association.

Weingarten, J. S., & Perkins, T. K. (1995). Prediction of sand production in gas wells: methods and Gulf of Mexico case studies. Journal of Petroleum Technology, 47(07), 596-600.

Williams, C. F., Richard, B. M., & Horner, D. (2006, January). A new sizing criterion for conformable and nonconformable sand screens based on uniform pore structures. In SPE International Symposium and Exhibition on Formation Damage Control. Society of Petroleum Engineers. Pages?

Wong, G. K., Fair, P. S., Bland, K. F., & Sherwood, R. S. (2003, January). Balancing act: Gulf of Mexico sand control completions, peak rate versus risk of sand control failure. In SPE Annual Technical Conference and Exhibition. Society of Petroleum Engineers. Pages?

Wu, B., & Tan, C. P. (2002, January). Sand production prediction of gas field-methodology and field application. In SPE/ISRM Rock Mechanics Conference. Society of Petroleum Engineers. Pages?

Wu, B., Choi, S. K., Denke, R., Barton, T., Viswanathan, C., Lim, S., ... & Madon, B. B. (2016, March). A New and Practical Model for Amount and Rate of Sand Production Estimation. In Offshore Technology Conference Asia. Offshore Technology Conference. Pages?

Yi, X., Valko, P. P., & Russell, J. E. (2004, January). Predicting critical drawdown for the onset of sand production. In SPE international symposium and exhibition on formation damage control. Society of Petroleum Engineers. Pages?

Yi, X., Valkó, P. P., & Russell, J. E. (2005). Effect of rock strength criterion on the predicted onset of sand production. International Journal of Geomechanics, 5(1), 66-73.

Yuki, Y., Takeuchi, S., & Kajishima, T. (2007). Efficient immersed boundary method for strong interaction problem of arbitrary shape object with the self-induced flow. Journal of Fluid Science and Technology, 2(1), 1-11.

Zervos, A., Papanastasiou, P., & Vardoulakis, I. (2001). Modelling of localisation and scale effect in thick-walled cylinders with gradient elastoplasticity. International Journal of Solids and Structures, 38(30-31), 5081-5095.

Zhou, Z. Y., Yu, A. B., & Choi, S. K. (2011). Numerical simulation of the liquid-induced erosion in a weakly bonded sand assembly. Powder technology, 211(2-3), 237-249.

Zivar, D., Shad, S., Foroozesh, J., Salmanpour, S. (2019). Experimental study of sand production and permeability enhancement of unconsolidated rocks under different stress conditions. Journal of Petroleum Science and Engineering, 181, 106238.

Zoback, M. D. (2007). Reservoir geomechanics: Earth stress and rock mechanics applied to exploration. Production and Wellbore Stability, 449.